Fermilab Library
0 1160 0035228 0

NASH

Inelastic and Elastic Photoproduction of J/ψ (3097)

by

Bruce Hayes Denby

July 1983

High Energy Physics
University of California, Santa Barbara

FERMI
THESIS
LIBOFFCE

UNIVERSITY OF CALIFORNIA
Santa Barbara

Inelastic and Elastic Photoproduction of $J/\psi(3097)$

A Dissertation submitted in partial satisfaction
of the requirements for the degree of

Doctor of Philosophy

in

Physics

by

Bruce Hayes Denby

Committee in charge:

Professor Rollin J. Morrison, Chairman

Professor Steven J. Yellin

Professor John L. Cardy

July 1983

AAC8055

The thesis of Bruce Hayes Denby
is approved:

John L. Cordy

Hans G. Gelin

Robert J. Niemi

Committee Chairman

July 1983

ACKNOWLEDGEMENTS

I am extremely grateful to all members of the collaboration for the many hours they have spent over the past six or seven years building, debugging, running, and analyzing results from the Fermilab Tagged Photon Spectrometer Facility. I list them here:

R. Morrison, M. Witherell, D. Summers, S. Yellin, V. Bharadwaj, B. Denby, D. Caldwell, A. Lu, A. Eisner, R. Kennett, U. Joshi

(University of California, Santa Barbara)

P. Estabrooks, J. Pinfold

(Carleton University, Ottowa, Canada)

S. Bhadra, A. Duncan, D. Bartlett, U. Nauenberg, J. Elliott

(University of Colorado, Boulder)

J. Appel, J. Biel, T. Nash, D. Bintinger, B. Schmidke, L. Chen, C. Daum, M. Sokoloff, K. Stanfield, K. Sliwa, M. Streetman, J. Bronstein, P. Mantsch, S. Willis

(Fermi National Accelerator Laboratory)

M. Losty

(National Research Council of Canada)

G. Kalbfleisch, M. Robertson

(University of Oklahoma, Norman)

J. Martin, G. Luste, G. Hartner, D. Gingrich, C. Zorn, J. Spalding, K. Shahbazian, J. Stacey, D. Blodgett, B. Sheperd, S. Bracker, R. Kumar

(University of Toronto, Toronto, Canada)

Of particular mention are the superhuman efforts put forth by Tom Nash, John Martin, Steve Bracker, and many others, during the early stages of getting E516 off the ground.

I give special thanks to my advisor, Prof. Rollin Morrison, for his persistent efforts in offering guidance, (which I appreciated more than I always outwardly showed), and also for continuing to support this research when it was unpopular with others.

Prof. Mike Witherell has been particularly helpful with the data analysis, and has been a pleasure to work with.

I have profitted a great deal from numerous conversations with Dr.'s Jeff Spalding, Jim Elliott, Gerd Hartner, and Kris Sliwa, concerning physics and data analysis.

I thank Dr.'s David Bintinger and Penny Estabrooks for their friendship and guidance while at Fermilab.

I thank Dr. Alan Duncan for allowing me to use figures from his thesis, many of which are reproduced here (41).

I appreciate Dr. Ed Berger's taking the time to discuss with me some of the theoretical questions involved in this work.

I thank Dr. Vinod Bharadwaj and my fellow graduate student (soon to be) Dr. Don Summers for their friendship and moral support over the years, as well as for valuable suggestions and advice.

The support from the Fermilab (former) Proton, Physics, and Computing Departments has always been first rate and is greatly appreciated.

My thanks and great respect go to Rudi Stuber, Dave Hale, and all the UCSB shops for their excellent performance during the construction of the SLIC and outriggers.

I give heartfelt thanks to my mother for her love, patience, and financial support during these difficult years. I would like to dedicate this thesis to the memory of my father, Harry H. Denby, who taught me about perserverance.

Most important of all, I thank my wife, Carol, without whose love, and understanding, I could not possibly have succeeded in this endeavor.

VITA

February 28, 1953--Born--Cleveland, Ohio.

1975--B.S., California Institute of Technology.

1975-1977--Research Intern, High Energy Physics, Rutgers University.

1977-1983--Research Assistant, High Energy Physics, University of California, Santa Barbara.

PUBLICATIONS

Equilibrium Charge States of Molecular Fragment Hydrogen,

Bruce Denby and W. Whaling

Bull. Am. Phys. Soc. 20 (1975) 1500

Inclusive Cross Sections and Average Charged Multiplicities in Inclusive K^0_L and Λ Production in π-P Interactions at 147 GeV/c,

with P.E. Stamer et al.,

Bull. Am. Phys. Soc. 22 (1977) 23

An Inexpensive Large Area Shower Detector with High Spatial and Energy Resolution,

with V.K. Bharadwaj et al.,

Nucl. Inst. Meth. 155 (1978) 411

ABSTRACT

Inelastic and Elastic Photoproduction of $J/\psi(3097)$

by

Bruce Hayes Denby

The $J/\psi(3097)$ photoproduction cross section on hydrogen has been measured at a mean photon energy of 103 GeV, using the Fermilab Tagged Photon Spectrometer, Batavia, Illinois. The total cross section, 21.5 ± 2.4 nb (±25% normalization) has been subdivided into 7 categories: 1) all events, 2) forward elastic, 3) forward inelastic, 4) recoil inelastic, 5) totally elastic, 6) inelastic, and 7) inelastic with $z = E_\psi / E_\gamma < .9$, as defined in the text. The forward inelastic cross section observed in this experiment is much smaller than that seen in muoproduction experiments (16,17), but is roughly consistent with second order perturbative QCD predictions (5). The mean p_+ of the forward inelastic events is significantly larger than that of the totally elastic events, in accord with the muoproduction experiments as well as the second order QCD predictions.

TABLE OF CONTENTS

FIGURE CAPTIONS xi

LIST OF TABLES.....xix

I. INTRODUCTION.....1

II. METHOD 9

III. EXPERIMENTAL APPARATUS

A. Photon Beam
1) Introduction 11
2) The Main Ring.....12
3) Electron Beam 12
4) Tagging System.....14

B. Spectrometer
1) Target.....16
2) Drift Chambers.....16
a) Chambers
b) Drift Chamber Calibration.
i) Drift Chamber TDC Gain Measurements
ii) Drift Chamber TDC Offset Measurements
iii) The Drift Chamber Pulser
iv) Generation of Gain and Offset Data
v) Maintenance of Drift Chamber Electronics
vi) Absolute Tϕ Measurements
vii) Drift Chamber Alignment
3) Analyzing Magnets 31
4) Electromagnetic Shower Detectors.....32
a) SLIC
i) Counter
ii) SLIC Construction
iii) SLIC Calibration
b) Outriggers
i) Counter
ii) Outrigger Calibration
5) Recoil Detector 47
a) Recoil Spectrometer
b) Recoil Detector Calibration
6) Hadrometer 52
a) Counter
b) Hadrometer Calibration
7) Cerenkov Counters.....54
a) Counters
b) Cerenkov Calibration

8) Muon Wall 56
a) Muon Counters
b) Muon Wall Calibration
C. Triggers
1) Tag-H 57
2) Recoil Triggers 58
3) Dimuon Trigger 60
D. Data Acquisition System 62

IV. DATA ANALYSIS

A. Producing the ψ Signal 64
B. Definition of Elastic and Inelastic 70
C. Classification of Events 73
1) Forward Classification
2) Recoil Classification
D. Determination of Z 80
E. Uncertainties in Classification 85
1) Uncertainties in Forward Classification
2) Uncertainties in Recoil Classification

V. EFFICIENCY CALCULATIONS

A. Track Reconstruction Efficiency 90
B. Elastic Monte Carlo 92
C. Inelastic Monte Carlo 94

VI. RESULTS 97

VII. DISCUSSION OF RESULTS 105

APPENDIX A: Figures 111

APPENDIX B: Tables 166

LIST OF REFERENCES 173

FIGURE CAPTIONS

1) First order QCD Psi photoproduction diagram: Photon Gluon Fusion.

2) Second order QCD Psi photoproduction diagrams (ref. 3,5).

3) Aerial view of Fermi National Accelerator Laboratory (Fermilab), Batavia, Illinois.

4) Schematic of Fermilab beam lines.

5) Proton Area beamlines.

6) Pre-target beamline components, target box, and electron transport system. Components labelled "BH" or "BV" are horizontal and vertical bending magnets, respectively. "QH" and "QV" components are horizontal and vertical quadrupole (focussing) magnets. "CH" and "CV" components are collimators. Components labelled "SC" are SWICS, which are small wire chambers used for monitoring beam profiles. TEBY is the primary target, and CONVET is the converter.

7) Electron and tagged photon beam components. Components labelled "LT" are lead targets, which

can be placed in the beam in conjunction with the SWICS to make the electron and photon beams more visible. AN440C is the tagging magnet, and ERAD is the radiator.

8) Electron beam focussing components and beam profiles.

9) Electron yield per 400 GeV proton versus electron energy.

10) Schematic layout of tagging system. L1-L13 are the tagging lead-glass blocks. H1-H13 are the hodoscopes. Counters labelled "A" are used in anti-coincidence. D1 and D2 are electron beam dump counters.

11) Typical tagged photon energy spectrum.

12) Layout of the drift chambers showing z coordinates.

13) Drift chamber cell configuration.

14) Drift chamber amplifier discriminator card with LeCroy DC201's, showing loop antenna from drift chamber pulser.

15) Cutaway view of drift chamber inductive pulse splitter. Only 2 of the 36 or 49 outputs are shown.

16) Printed circuit board artwork used in making the inductive pulse splitters.

17) The inductive/capacitive coupler used to feed pulses into the high-voltage planes of the drift chambers for timing offset measurements.

18) Circuit diagram of the drift chamber test pulser, used for measuring gains and offsets of the TDC's.

19) The SLIC electromagnetic shower counter.

20) Illustrating the construction of the SLIC. Shown are the three orientations of the corrugations and their arrangement in the tank.

21) Implementation of the wavebar readout system. The U view, which read out on top of the SLIC, is shown.

22) In a), the intersection of an electron shower with a typical SLIC counter is shown, illustrating the pair calibration technique

described in the text. In b), an actual shower shape curve from the calibration program is shown, with a fitted Gaussian (asterisks).

23) Schematic overview of the Tagged Photon Spectrometer Facility. Counters are described in detail in the text.

24) The Tagged Photon Spectrometer Facility, Fermilab.

25) OUTRIGGER electromagnetic shower counter, showing X and Y readout schemes.

26) Photon's-eye-view of the Recoil Spectrometer.

27) Cutaway view of recoil PWC's.

28) Cross section of a recoil PWC.

29) The Hadrometer.

30) Upstream Cerenkov counter (C1).

31) Downstream Cerenkov counter (C2).

32) Cerenkov counter optics.

33) Cerenkov counter mirror segmentation (both counters have the same segmentation arrangement),

and mirror suspension system.

34) Schematic of the Muon Wall.

35) Logic diagram of the Hadronic trigger (tag-H).

36) Layout of the dimuon trigger counters, showing location of the Pre-C and Caboose counters.

37) Dimuon trigger logic diagram.

38) Data acquisition system.

39) X, Y, and Z position of dimuon vertices for the final data sample. Also shown is the distribution in distance of closest approach. These distributions are quite clean and do not reduce the significance of the signal.

40) Final dimuon mass spectrum showing all events above 1.5 GeV/c^2. There are 147 events in the range $2.8 \leq M(\mu^+\mu^-) < 3.4$ GeV/c^2.

41) The final dielectron mass spectrum. There are 63 events in the range $2.8 \leq M(\mu^+\mu^-) < 3.4$ GeV/c^2.

42) Dimuon events which were classified as forward elastic (defined in text). There are 110 events between 2.8 and 3.4 GeV/c^2.

43) Dimuon events which were classified as forward inelastic (defined in text). There are 37 events between 2.8 and 3.4 GeV/c^2.

44) In a) we plot $z = E_\psi/(E_\psi + E_x(1))$, where $E_x(1)$ is the total energy of all detected non-Psi particles; i.e., assuming that <u>all</u> forward energy is detected. In b) we plot $z = E_\psi/(E_\psi + F*E_x(1))$; i.e., we correct z for the measured mean inelastic energy deficit.

45) We use the means of these distributions to calculate the average fraction of non-Psi forward energy that we detect. In a), $R = E_\psi/E_\gamma$ for elastic forward events, which peaks near 1, as it should. In b), $R = E_\psi/E_\gamma$ for inelastic forward events; this distribution peaks below 1 since the other particles carry some energy. In c), $R = (E_\psi + E_x(1))/E_\gamma$; we add back in the detected inelastic energy. The peak is midway between those of a) and b).

46) Plotted are the numbers of charged tracks, photons, pi-zeroes, hadronic neutrals detected per inelastic forward event. In e) the total number of particles is shown; here, pi-zeroes count as two particles.

47) Total forward mass for those inelastic events with two extra tracks of opposite charge and no extra photons or hadronic neutrals. The Psi four-vector has been constrained so that its square is exactly the Psi mass. There is a peak of 4 events near the Psi-prime mass 3.685.

48) The overall event reconstruction efficiency ε for elastic events as a function of photon energy k.

49) Mean p_+ versus z from the inelastic monte-carlo (histogram). The smooth curve is from the color singlet model of Berger and Jones (ref. 5). Both are evaluated at 100 GeV.

50) Overall inelastic event reconstruction efficiency ε from the inelastic monte-carlo as a function of z, evaluated in two bins of p_+. The photon energy is 95 Gev.

51) Overall inelastic event reconstruction efficiency ε as a function of z, evaluated for two photon energies. All p_+ values are included.

52) Number of events corrected for efficiency plotted versus the corrected z value (defined in text) for that event. The recoil inelastic events, which are defined to be in the highest bin are left off in this plot. Also shown is an estimate of the contribution from ψ' based on the measurement of ref. 15.

53) The same distribution as in figure 52 but the recoil inelastic events are added into the highest bin.

54) a) shows the p_+ distribution for totally elastic (defined in text) events. b) shows the p_+ distribution for forward inelastic (defined in text) events. The inelastics clearly have a flatter p_+ distribution.

LIST OF TABLES

I. Drift Chamber Resoultions and Efficiencies...167

II. Cerenkov Counters 168

III. Cerenkov Cells.....168

IV. Raw and Corrected Events in Each Category....169

V. Fractions in Each Category 170

VI. A. Cross Sections in Each Category 171

B. ψ'-Subtracted Cross Sections in Each Categ ..171

VII. A. Comparison of Elastic Cross Sections 172

B. Comparison of Inelastic Cross Sections.....172

C. Comparison of Inelastic Ratios 172

I. INTRODUCTION

Production of the $J/\psi(3097)$ meson is a particularly attractive vehicle for an experimental study of the strong interaction because the J/ψ has large branching fractions into dimuons and dielectrons (7.4 percent into each), which provide very clean signatures for events containing the J/ψ. Photoproduction is likely to be one of the best methods of producing the J/ψ because: 1) Vector Meson Dominance (1) dictates a sizable coupling of photons to vector mesons, (the J/ψ is a vector meson like the ρ, ω, and ϕ), and 2) There are fewer hadronic background processes in photoproduction.

From a theoretical standpoint, the J/ψ has proved an excellent system in which to study the strong interaction via perturbative Quantum Chromodynamics (QCD). The J/ψ has been successfully interpreted as one of a family of bound states, called charmonia, of a charmed (c) and anticharmed ($\bar{c}$) quark (2). Perturbative QCD should be valid when the running coupling constant $\alpha_S(m^2)$, is small, which in turn requires that the mass scale, m^2, of the process under consideration be large. In the case of the J/ψ, the

large charmed quark mass, $m_c = 1.5$ GeV/$c^2 \cong .5M_\psi$, ensures that α_s will be small (3,4,5). It is usually taken to have a value of 0.2 to 0.4 (4,5). Photoproduction of the J/ψ should perhaps be simpler to calculate than hadroproduction since: 1) The photon has a direct, pointlike coupling to the $c\bar{c}$ system, and 2) There are no competing Drell-Yan (quark-antiquark annihilation) diagrams to lowest order in α_s (7).

The simplest QCD diagram that can be drawn for J/ψ photoproduction, shown in figure 1, involves the photon's materialization into a $c\bar{c}$ pair, with one of the quarks then interacting with a gluon from the target nucleon. This has come to be referred to as Photon Gluon Fusion, or simply γGF. Qualitatively, this diagram is expected to describe the elastic part of the J/ψ photoproduction cross section (4,9,10). In the framework of the parton model, gluons are taken to be on-shell (8,10,11). Thus for a one-gluon exchange, $-t \equiv Q^2 \cong 0$, indicating forward, diffractive scattering where the J/ψ has very low p_+. Thus far, the first-order γGF diagram describes all $c\bar{c}$ production, both bound and unbound. It has become common to assume, on the basis of semi-local duality arguments, that the kinematics of the real final state

particles are essentially given by those of the c quarks (12, 13).

A calculation of open charm (i.e., unbound $c\bar{c}$ pairs) production gives good agreement with the observed energy dependence and normalization of the data (14). In order to calculate the bound charm cross sections, further assumptions are necessary. First, duality arguments are invoked as before, but with the added assumption that (3, 9, 10, 12, 13)

$$\sigma(\text{bound } c\bar{c}) = \int_{2m_c}^{2m_D} \frac{d\sigma(m)}{dm} \, dm$$

where m_c is the charmed quark mass, m_D is the charmed D meson mass, and $d\sigma(m)/dm$ is the cross section calculated for figure 1. Thus bound $c\bar{c}$ production is taken to be the sum of all $c\bar{c}$ production from $c\bar{c}$ threshhold to open charm threshhold. It now remains to determine what fraction of this is actually J/ψ production. The standard prescription, put forth by Fritzsch (12) is that

$$\sigma_{\psi} = F \cdot \sigma(\text{bound } c\bar{c})$$

where F is the reciprocal of the number of charmonium states, usually taken to be in the neighborhood of 8. This prescription is somewhat arbitrary, and probably wrong, since it predicts equal contributions from all charmonia; recent photoproduction data (15) have shown that the ψ' cross section is only about 20% of the J/ψ cross section. Nevertheless, F must have some value less than one, and using this method, it is possible to reproduce the energy dependence of existing elastic J/ψ photoproduction data rather well (see, e.g. ref. 9).

The use of fig. 1 has a number of fundamental shortcomings: 1) Since only one gluon interacts with the $c\bar{c}$ system, color cannot be conserved, and furthermore, the $c\bar{c}$ system cannot be in a $J^{PC} = 1^{--}$ state. Additional soft gluon(s) must be emitted in a way which is not specified by the theory, and which is assumed not to affect the kinematics of the charmed quarks (12). 2) It is necessary to invoke duality arguments to calculate cross sections. 3) The F factor makes the normalization uncertain. 4) It

probably describes only the elastic cross section.

The lowest order color-conserving diagrams are shown in figure 2 (3,5). These two-gluon diagrams are of order α_s^2 and can qualitatively be thought of as describing inelastic J/ψ photoproduction, since the J/ψ now carries only a fraction $z = E_\psi / E_\gamma$ of the energy of the photon, the rest being carried by a gluon. Also, sizeable p_+ can now be transmitted to the J/ψ (10,14). In calculating with these diagrams, one can again invoke duality and an F factor (3) to get cross sections. The inelastic cross sections are thus expected to be of order α_s times the elastic cross sections (4,6,9), i.e., about 30 percent of the elastic cross sections.

An alternative approach has been adopted by E. Berger and D. Jones (5). Here an explicitly normalized (i.e., parameter free) cross section is calculated by representing the $c\bar{c}$ pair as a normalized $J^P = 1^-$ J/ψ wavefunction. The coupling strength of the J/ψ to $c\bar{c}$ is specified by the electronic width of the J/ψ, $\Gamma_{ee} = 4.8$ keV. Berger and Jones stress that the use of the parton model is justified only in certain kinematic regions, in particular,

1. $m_X \gtrsim 2$ GeV/c² where m_X is the mass of X in $\gamma p \to J/\psi X$. This excludes elastic production, $\gamma p \to J/\psi p$, and quasi-elastic production $\gamma p \to J/\psi N^*$.

2. $|t| = |(p_\psi - p_\gamma)^2| > 1$ GeV²

They show that these conditions will be satisfied only when

$$z = \frac{E_\psi}{E_\gamma} \lesssim .9$$

In our analysis, we shall often make use of this cut, both to allow comparison with theoretical predictions, and to allow our data to be compared to other data, which are often cut in this way.

The main features of inelastic J/ψ photoproduction in the Berger and Jones model are: 1) A z distribution peaked at high z, falling off rapidly at low z. 2) High p_+. The predicted mean p_+ at E_γ = 100 GeV is about 1 GeV. 3) A relatively low cross section. At 105 Gev, the predicted inelastic cross section for $z < .9$ is 2.9 nanobarns. The measured elastic cross section at this energy is roughly 12 to

20 nanobarns (16,17,18). This prediction is in keeping with the qualitative notion that the inelastic cross section should be of order α_s times the elastic.

Since the Berger-Jones model predicts a normalized cross section, it can be compared with data. Inelastic J/ψ data exists from two muoproduction experiments, the Berkeley-Fermilab-Princeton group (BFP, 17,19,21), and the European Muon Collaboration (EMC, 16,20,29). The data from these two experiments, which both used spacelike virtual photons on iron targets, have been corrected for nuclear effects, and extrapolated to $Q^2 = 0$ to yield numbers for photoproduction on single nucleons. While both experiments report z distributions in rough agreement with Berger and Jones, the experimental inelastic cross sections are roughly a factor of 5 larger than the predictions (5,16,17,20,21,29). As the only adjustable parameter in the Berger-Jones model is the value of α_s, which probably cannot vary by more than about 50 %, there is little chance of reconciling this theory with this data (43).

The inelastic data thus seem to be at serious

odds to the theoretical predictions of second order perturbative QCD. In what follows, we will show that a very different result is obtained when the J/ψ is photoproduced on hydrogen with real ($Q^2 = 0$) photons.

II. METHOD

Requisite to the photoproduction of ψ on hydrogen, and the subsequent analysis of events are:

1. A high energy photon beam with sufficient luminosity to produce a statistically strong sample of ψ events in a reasonble length of time.

2. A hydrogen target.

3. A multiparticle spectrometer with the capability to detect and measure four-vectors of all charged and neutral particles produced in the hadronic interaction of the photon with the proton in the target.

4. An experimental trigger with the ablility to select the desired events out of a huge background of electromagnetic processes, as well as reject other, less interesting hadronic processes.

5. A data acquisition system which has the ability to record data from over a thousand different channels on each event, at a rate of about 100 events per second.

6. Offline reconstruction software, and computing power, which can reduce millions of raw triggers down to a manageable set of reconstructed data summary tapes on a reasonable time scale.

In the following section, each of these components, as implemented in Fermilab experiment E516, is discussed in detail.

III. EXPERIMENTAL APPARATUS

A. THE PHOTON BEAM

1. INTRODUCTION

To photoproduce a ψ meson on hydrogen, a photon energy of about 8 GeV or more is necessary, however, earlier experiments (22-25,18) have shown that the cross section for $\gamma p \rightarrow \psi p$ at photon energies near 100 GeV is roughly 50 times larger than at 11 GeV, and thus, it is advantageous to make use of photons of the highest available energies in order to ensure a high production rate. It is also important that the photon beam be free of hadronic contamination since hadroproduction cross sections are typically two orders of magnitude larger than the total photoproduction cross section. Finally, it is useful to know the energy of each photon in the beam with good precision so that energy balance constraints can be imposed, and as will be seen for this experiment, for use in triggering.

The tagged photon beamline of the Tagged Photon Specrometer at Fermi National Accelerator Laboratory, Batavia, Illinois, provides a very clean beam of high energy photons of known energy. The photons are

produced in a multi-step process which is outlined below.

2. THE MAIN RING

All the particle beams for high energy physics research at Fermilab have as their source the large main ring, a proton synchrotron. Protons from a hydrogen ion source are accelerated to 750 keV in the Cockcroft-Walton, to 200 MeV in the LINAC, and to 8 GeV in the booster ring before entering the 4 mile circumference of the main ring where they are accelerated to 400 GeV. (The peak energy is currently being upgraded to 1000 GeV.)

The protons are resonance extracted from the main ring and directed onto the septum. This is a set of wire planes at high positive electrostatic potential set parallel to the beam direction. The protons are repelled from the wire planes as they pass them and the beam is thereby split into three beams, which enter the swithchyard where they are focussed and bent magnetically toward the three main experimental areas, Meson, Neutrino, and Proton. See figures 3, 4, 5 for a layout of the main ring and experimental areas.

3. ELECTRON BEAM

The proton area beam is split in enclosure H by another septum into three beams which go to the PWest, PCenter, and PEast areas. In enclosure E1 in the PEast beamline the protons can be directed either onto the Wide-Band or Tagged Photon primary targets. Protons hitting the 30 cm. long beryllium target (TEBY) of the Tagged Photon beamline produce charged and neutral secondaries. The charged secondaries are swept magnetically into a beam dump, while the neutrals, consisting of neutrons, K^0_L, and photons (from π^0) pass forward to a .32 cm thick (.5 radiation length) lead converter located 12 meters downstream. Roughly 40% of the photons form e^+e^- pairs in the radiator, while less than 2% of the hadronic neutrals interact to form more secondaries. The converter is followed by an electron beam transport system consisting of two stages, each with bending and focussing magnets and collimators. The undeflected neutrals pass into the neutral dump, as do any positively charged secondaries. By adjusting the magnet currents, the beamline can be tuned to transport a beam of 10 to 300 GeV/c. The momentum resolution of the beam is about ± 2.5%. The momentum selection reduces the already small hadronic

contamination of the electron beam to a negligeable level. The beamline components are shown in figures 6, 7, and 8. The electron beam intensity per incident 400 GeV proton is shown in figure 9 as a function of electron beam energy.

4. TAGGING SYSTEM

The tuned electron beam now enters the tagging system. Electrons pass through a copper radiator, and in so doing create bremsstrahlung photons with an energy spectrum given by the thin radiator approximation (34):

$$N(k)dkdx = \frac{dk}{k}\left(\frac{4}{3} - \frac{4}{3}\left(\frac{k}{E_o}\right) + \left(\frac{k}{E_o}\right)^2\right)dx$$

where N(k) is the number of photons near energy k, dx is the thickness in radiation lengths, and E_0 is the electron beam energy. A simple dk/k spectrum is often used in rough calculations. The photon angles are dominated by the multiple scattering angle of the electron in the radiator, which for all practical purposes is $\theta = 0$. While the photons pass straight forward into the experimental hall, the electrons are

bent by the tagging magnets toward the tagging blocks. This is a set of 13 lead glass or lead-lucite blocks instrumented with phototubes and used as shower counters to measure the energy of the electron after radiating, E'. The energy of the tagged photon is then simply

$$E_\gamma = E_o - E'$$

A set of hodoscopes, H1-H13, in front of the lead glass counters gives an independent measurement of the position of the electron. The tagging system is pictured in figure 10.

To enhance the photon flux, one wants the radiator as thick as possible, but as the radiator thickness increases, the probability that the radiated photon will pair produce in the radiator also increases, as does the probability of multiple bremsstrahlung. The thickness .2 radiation lengths was chosen to give as high a rate as possible while keeping the pair production and multiple bremsstrahlung at an acceptable level.

Additional bremsstrahlung photons from a single

electron pass into the C-counter, a total absorption shower counter located downstream. The tagging energy in this case is corrected by

$$E_\gamma = E_o - E' - E_C$$

where E_C is the energy of the additional photon(s) in the C-counter. The fact that the radiator is no longer thin causes the spectrum to deviate somewhat from the thin radiator approximation given above. In particular the high energy end of the spectrum does not scale linearly with radiator thickness. The resulting tagged photon energy spectrum for this experiment is shown in figure 11.

B. SPECTROMETER (42)

1. TARGET

The target consists of a 1.5 meter long, 1 inch radius flask of .005 inch mylar, filled with liquid hydrogen. This was surrounded by a 2.5 inch radius, .5 inch thick foam vacuum jacket covered with another layer of mylar.

2. DRIFT CHAMBERS

a. CHAMBERS

Four chambers, herein referred to as D1, D2, D3, and D4, were used to determine trajectories and momenta of charged particles in the forward spectrometer. The overall layout of the chambers is shown in figure 12. Space points are derived from the coordinates of tracks in wire planes of three orientations, namely U and V planes, at ± 20.5 degrees to vertical, and X planes, which are vertical. The presence of three views allows most ambiguities in track positions to be resolved.

D1, the small chamber located inside M1, consists of two assemblies, each containing U, V, X, and X′ planes. The X′ plane is simply another partial X plane, offset slightly from the X plane, for added redundancy near the beam where rates are highest. D2 and D3 each have three UXV assemblies, and D4 has a single UXV assembly. Thus the trajectory of a particle traversing all four chambers will have a total of 9 measurement points on it: 2 in D1, 3 each in D2 and D3, and one in D4.

In D1-D3, sense wires are at ground, and high voltage wires are at negative potential. In D4, sense

wires are at positive high voltage, the field wires are at ground, and the field wires in the sense plane can be set at a small positive or negative voltage. The drift cell configuration of the chambers is shown in figure 13.

All chambers were mounted on rails so that they could be removed for maintenance or to access another detector.

The chambers were filled with a mixture of 50% argon, 50% ethane, at .1 inches of water, and a small amount of ethanol vapor (D1 and D2 only) to enhance quenching at high rates.

Signal wires were ganged in groups of 16 into card edge connectors on the chambers into which the LeCroy DC201 amplifier-discriminator cards were plugged. Twisted pair cables from each card carried the logic signals to the LeCroy 2770 TDC's, which were read by the online program on each event and written to tape. The stop signal for the TDC's was provided by the low level logic.

b. DRIFT CHAMBER CALIBRATION

i. DRIFT CHAMBER TDC GAIN MEASUREMENTS

To determine the gains of the individual TDC's it

is necessary to be able to artificially supply them with start and stop pulses separated by predetermined delay times. On a small prototype chamber it was found possible to measure both gain and offset by injecting a pulse into the H.V. plane supply line. The pulse travelled down the wires of the H.V. plane and induced pulses on the sense wires which in turn fired the amplifier-discriminators. For the actual chambers used in this experiment, however, this method proved unfeasible for determining gains since single pulses injected into the high voltage plane, presumably due to the size and geometry of the chambers, induced high frequency bursts of pulses at the sense wires which caused the discriminators to multiple pulse. Each subsequent pulse would restart the TDC clock, rendering gain measurements impossible. (Offset measurements were still possible, as we shall discuss later.) A great many different pulsing schemes involving inducement of pulses by the H.V. plane were tried with no success.

On the other hand, it proved relatively easy to produce single output pulses from the discriminators by inducing an input pulse on the wires where they plug into the amplifier cards. The most effective

technique found was to lay a small 50 ohm terminated loop antenna over the solder pads for the 16 wires on each card, as illustrated in figure 14 (30). A 2.5 to 3.0 volt pulse with a risetime of 10 to 20 nanoseconds was found to give single ouput pulses from all 16 channels on a card, with very little crosstalk into neighboring cards. A wide variety of antenna designs were tested to try to increase the number of wires that could be pulsed at one time, since roughly 5000 wires had to be calibrated. None of these proved successful. Thus, although a reliable method of pulsing 16 wires now existed, it seemed as though some 300 separate pulsers would have to be built and maintained.

This problem was elegantly solved by the use of inductive pulse splitters. Resistive splitters are inappropriate since the voltage at each splitter output is 1/N times the input voltage. To put 3 volts into each of, say 25 antenna cards, an initial pulse of 75 volts would be necessary. With an impedance-matched inductive splitter, the output voltage is $1/\sqrt{N}$ of the input, so an initial pulse of 15 volts is adequate. The turns ratio is PRI:SEC = $\sqrt{N}:1$ where N is the number of outputs. To ensure an

integral turns ratio (for ease in winding the coils) the number of outputs should be a perfect square.

On D1, two 49-way splitters were used, one on the East side and one on the West. On D2, one 49-way splitter served each of the three assemblies (UXV triplets), while D3 had 36-way splitters on each assembly. D4, with only three planes, used a single 36-way splitter. All unused outputs were terminated in 50 ohms.

The design of the splitters themselves presented several challenges. Although the use of 2 or 3 way inductive splitters is common, it was not known if a 49-way splitter could be made to work. A fast, low loss core material is necessary. Coil winding must be done carefully to prevent stray capacitance. The primary must be spread uniformly over the core to fully utilize its volume. The core must be kept as small as possible to preserve the integrity of the pulse shape. Careful attention must be paid in winding so that all secondaries have the same polarity (31).

After a number of tests with 16 and 25-way prototypes, the following design was arrived at. A 7/8 inch diameter ferrite core of material 3E2A was

chosen as the core (32). (A 49-way splitter will be used to illustrate the technique used; the 36-way splitters are constructed in exactly the same way.) The turns ratio used was 14:2. The 49 secondaries each consisted of 2 turns of fine magnet wire and were secured by simply twisting the ends together. One end had been flagged before winding to establish polarity. The primary consisted of three 14 turn coils of insulated hookup wire connected in parallel, with the turns uniformly spread around the toroid. The wound toroids were then mounted to specially prepared printed circuit boards as shown in figure 15. The artwork used to prepare the P.C. boards is shown in figure 16. The back of the boards was solid ground plane. The core was held in place by the pigtails on the secondaries, which were soldered to the pads and ground plane. Each secondary had its own 50 ohm LEMO cable which was fed through a 3-hole strain relief system and soldered to the pads, and each of these cables had a connector at the far end for plugging into the antenna card. The board was then enclosed in an aluminum box which provided electrical shielding as well as a framework to which the LEMO connector for primary input was affixed. The shielding was

completed by a conical brass dish soldered to the ground plane. This complete shielding arrangement was found essential to prevent ringing on the outputs which would cause the discriminators to multiple pulse. Construction of the splitters was done in an assembly line operation manned by 4 technicians and took about 3 weeks.

Performance of the completed splitters was very good. Each output was tested individually for pulse height, pulse shape, and timing. Pulse heights and shapes were quite uniform for most of the outputs; a few varied on the order of 5% in pulse height or exhibited slight variations in pulse shape. The pulse heights were quite accurately given by $1/\sqrt{N}$ times input pulse height, indicating low loss. No timing variations were detected. The use of inductive splitters thus reduced the number of pulsers needed from about 300 to only 9. The pulse generators and time delay scheme for gain measurement are outlined in following sections.

ii. <u>DRIFT CHAMBER TDC OFFSET MEASUREMENTS</u>

Although the inductive splitter/antenna card pulsing method outlined above should in principle be

adequate for offset calibration as well as gain calibration, in practice it has one drawback which makes H.V. plane pulsing more attractive. The risetime of the pulses out of the pulse generator is a function of pulse height. At 5 volts, the risetime is about 8 nanoseconds, but at the 20 volt setting needed for a 49-way splitter, the risetime is 15 nanoseconds. Since discriminators on the sense wires do not in general have equal threshholds, a long pulse risetime could introduce variations of a nanosecond or two in the response times. This is not important for gain measurements since only time differences are used, but for offsets one wants to know the time responses of the wires relative to each other and thus the shortest risetime possible is desireable.

A 5 volt pulse of 8 nanosecond risetime injected into the high voltage plane was found adequate for determining offsets. Although the discriminators multiple pulsed, by applying the stop pulse before the arrival of the first reflection, a reliable response, near the high end of the TDC (about 220 counts) was possible.

The signal was coupled into the high voltage cable by means of a capacitive/inductive coupler (35),

illustrated in figure 17.

The risetime problem is really the only drawback in the splitter scheme since the toroids introduce no time jitter, the outputs are uniform in size, and all cable lengths were kept the same. Thus, if a means of achieving a 20 volt, 8 nanosecond pulse becomes available, the splitter method could be used for offsets as well as gains.

iii. THE DRIFT CHAMBER PULSER

The drift chamber pulser is an addressable, remotely triggerable array of up to 64 individual pulse generators. In practice 20 of these were used in this experiment:

1. outputs 1-8 for 20 volt splitters on D1, D2, D3

2. output 9 for 30 volt splitter for D4

3. outputs 10-13 for 5 volt H.V. pulsing for D1

4. outputs 14-20 for 5 volt H.V. pulsing for D2, D3, D4

The number of splitter outputs was dictated by the number of assemblies, as discussed earlier. The H.V. outputs were set up so that there was one for each H.V. cable feeding the drift chambers.

The pulser to fire was selected by the online program by writing an address to a CAMAC output register. The levels at the output of this device were decoded by the D.C. pulser with conventional logic chips to select the appropriate pulser line. Each individual pulser consists of both halves of a Texas Instruments SN75454 dual peripheral NOR driver connected in parallel, which when enabled, allowed a 680 pf capacitor to discharge, producing the output pulse. The enable signal was also supplied by the online program by means of a CAMAC TTL pulse generator. The circuit schematic of the D.C. pulser is shown in figure 18.

The splitter pulsing method did not work on D1 because on D1, the sense wire signals came out of the chamber on short RG174 jumper cables before going into the cards, and the pulser signals reflected off the chamber ends of these jumpers causing double-pulsing. It was found possible to use H.V. pulsing at two closely spaced times to determine gains. This was

adequate since D1's drift time is only 50 ns and small variations in wire gain will not introduce significant time jitter.

D4 did not respond well to the splitter pulsing with a 20 volt signal into its splitter. This was found to be because the pulse height seen by the discriminator is proportional to the value of the input resistor, which was 100 ohms for D4, but 300 ohms for D1, D2, and D3. For this reason, a special D4 output was constructed on the pulser board. Four SN75454 chips were ganged in parallel to distribute the current load, and the output of these was put through an 8 turn auto-transformer to boost the signal. With this scheme, and by raising the bias voltage to 30 volts, D4 response was quite good.

iv. GENERATION OF GAIN AND OFFSET DATA

The drift chamber system was controlled by the online data monitoring program. Just before each beam spill, the monitor program sent a trigger pulse to the pulser system, which in turn sent a pulse to the assembly that had been selected by the output register for the current set of events. The returned "synch out" pulse, appropriately delayed through the FAD box,

(a software controlled CAMAC analog delay module), was fanned out as stop pulses for the 2770's, and also entered the test trigger fan-in, generating an event interrupt.

Ten events were taken at each time delay setting for each drift chamber assembly. The 2770 TDC's have a full scale of 256 counts. Delay times were chosen to give readouts of 60, 120, 180, and 240 counts. (For high voltage pulsing, the readout was typically 220 counts.) Cycling through the delay times and assemblies in this way, a complete set of calibration data was accumulated in about 2 hours.

The data thus accumulated on tape during running was later read by the offline monitor program which corrected bad or missing data, and made fits to the gains and offsets (also called relative T_0's). These numbers were then stored in run-number indexed calibration disk files for subsequent use by the track reconstruction program.

In addition to being written on tape, the responses of the TDC's were compared online to benchmark values stored on disk on the online computer. Channels out of specification were flagged as bad in a monitor report which was spooled to the

lineprinter to alert the person on shift of the problem.

v. MAINTENANCE OF DRIFT CHAMBER ELECTRONICS

The drift chamber system consists of some 5000 individual channels, each with its own DC201, its own twisted pair cable, and its own TDC. In order to keep run-time conditions as trouble free as possible, the entire drift chamber electronics system was checked out once weekly during the scheduled down day.

This checkout was accomplished with a comprehensive set of maintenance programs, written in the FORTH computer language, which used graphics displays and the pulser system to check the mean and sigma of the time responses of each channel. Routines to check gains and T_0's were also run. These FORTH routines turned the staggering complexity of the drift chamber system into a fairly manageable system.

vi. ABSOLUTE T_0 MEASUREMENTS

The TDC offsets for a wire plane measured with the pulser system, when subtracted from the times measured in real data events ensure that the resulting times are measured with respect to a common base value

for the wires in that plane. (Actually, pulsing is done by assembly, but T_0's are established on a plane by plane basis to be on the safe side.) The offsets of the planes with respect to one another remains to be determined. This is best done using raw times for real data events. For perfect resolution one expects a time distribution that is uniformly populated from T_0 to T_0 + total drift time, but in practice the leading and trailing edges have a slope and are somewhat rounded off. The absolute T_0 is taken as the point where the time distribution just begins to turn on. This value was found to be more stable than other possible choices. These absolute T_0's, as in the case of relative T_0's were detemined in an initial monitor pass run on each raw data tape, and were stored in run-number indexed calibration files for subsequent use by the track reconstruction program. Additional work was done on these files, using reconstructed events, to correct for variations in drift velocity, non-linearities in drift velocity, and to find hitherto undetected errors.

vii. DRIFT CHAMBER ALIGNMENT

The drift chamber wires were laid using a special

video-aided technique which allowed alignment to within .001 inch. Standard optical survey techniques were used to measure the physical position of the fiducial marks on the chamber bodies. The location of TPL was such that a substantial flux of muons from the primary target constantly passed through the apparatus. Although this was an unwanted background during normal running, the muons provided an excellent source of straight-through (with magnets off) tracks for chamber alignment. A special muon trigger was set up and muon runs were taken periodically to supply a set of alignment constants for the reconstruction program.

In practice, the final T_0 and alignment constants were correlated and were arrived at through an iterative process. It is also possible to measure resolution and efficiency of the drift chamber planes using the muon run data. These are tabulated in table I.

3. ANALYZING MAGNETS

The spectrometer utilizes two analyzing magnets called M1 and M2. D1, M1 and D2 comprise the "low momentum" arm of the spectrometer, while "high"

momentum tracks are measured with both magnets and all four chambers. This 2 component spectrometer system is discussed more fully in the section on the outriggers. The two magnets are identical in construction, although M1 has one coil and M2 has two. Pole pieces are one meter in length. During data taking M1 was run at 1800 amps giving a total integrated field of 5 kgm, and M2 was run at 900 amps, also giving 5 kgm.

A field map was generated using the Fermilab "Zip-Track", a computer aided magnet mapping machine which recorded the three components of the field at a grid-work of points throughout the volume of the magnet as well as several feet out into the fringe fields. The field map data was analyzed offline and parametrized for use by the track reconstruction program in computing momenta. The absolute calibration of the magnets was accomplished by means of an NMR probe.

4. ELECTROMAGNETIC SHOWER DETECTORS

Electrons, photons, and by their photon decay products, neutral pions are detected by the electromagnetic showers they produce in the SLIC or

outriggers. The majority of such particles hit the SLIC, while those produced at wider angles hit the outriggers. The geometry of these detectors is such that particles which would just miss the top or bottom of the SLIC will be intercepted in the outriggers.

a. SLIC

i. COUNTER

The SLIC (the name is an acronym for Scintillator Lead Interleaved Counter) is a very large area (12 square meters) electromagnetic shower counter consisting of 60 layers of lead interspersed with layers of liquid scintillator. Each lead-scintillator layer makes up 1/3 of a radiation length, for a total of 20 radiation lengths, so that even the highest energy showers will be almost totally contained. Each scintillator layer is divided into 1.25 inch wide strip hodoscopes by means of square wave shaped aluminum corrugations. These hodoscope layers have three possible orientations, U and V, at ± 20.5 degrees to the vertical, and Y, which is horizontal. Three views are used to help in resolving ambiguities in complicated events. There are 20 layers of each type, and they are interleaved in the order U, V, Y.

The lead sheets are laminated between two sheets of aluminum by means of adhesive sheets. The edges are sealed with epoxy so that the lead, a known scintillator poison, never comes in contact with the liquid scintillator.

The surfaces of the laminates and corrugations are all covered with aluminized teflon film which was applied in strips with a tape-laying machine. Thus each hodoscope strip is lined with teflon. Since liquid scintillator has a higher index of refraction than teflon, the scintillator light produced in showers propagates the length of the strip by total internal reflection.

The layers and scintillator are contained within a unique tank, which is structurally rigid (sustaining high hydrostatic pressure), yet transparent on 4 of its sides. The front and back faces are "wirecomb" panels (36). The top, bottom, and sides consist of rectangular lucite windows, with O-ring edge seals, held in place by window grates made of 2 X 1/4 inch steel bars laid on edge. The ends of the hodoscope strips fall in the spaces between the bars.

On the outside of the windows, lucite waveshifter bars, called here wavebars, are placed between the

window bars. Light emerging from the ends of the hodoscopes passes through the windows and into the wavebars, where light of a shifted wavelength is generated. This light then travels down the wavebar to the photomultiplier glued to its end. The wavebars thus integrate the light from all sixty layers.

In the U and V views, each of the 38 central counters feeds into its own wavebar, while the other 71 are ganged two to a wavebar. In the Y view, the inner 40 channels on each side are single and the outer 36 are double. The single wavebars are optically coupled to 2 inch RCA 4900 PMT's and the double wavebars have 3 inch RCA 4902 PMT's.

The construction details outlined thus far can be more readily understood by examining figures 19, 20, 21.

The PMT anode signals are digitized by LeCroy 2285 ADC's and are read out on each event by the data acquisition system. The dynodes of the Y counters (excluding the pair plane) were summed and became a part of the HADRON sum for the tag-H trigger.

ii. <u>SLIC CONSTRUCTION</u>

The construction of the SLIC presented a number

of challenges since a shower detector of this type had never been built before.

Before construction, extensive testing took place to determine what materials might degrade the scintillator, and to ensure that a good attenuation length could be obtained. Aluminum, stainless steel, teflon, lucite were used exclusively in the construction, with the exception of the O-rings, which were of Viton.

All the corrugations started as flat aluminum sheets, to which adhesive-backed teflon tape was applied with a tape-laying machine. This device removed the mylar release layer from the tape and replaced it back on top of the teflon surface while pressing the adhesive layer to the aluminum. The release layer remained in place until the final assembly and did much to preserve the delicate finish of the teflon. After application of the teflon, the corrugations were made on a pneumatic brake with a specially prepared aluminum die. The corrugations for each U, V, and Y layer were cut to size with a high-speed table saw and set aside as a package until needed. The U and V channels each had a mirror at the end opposite the wavebar to increase light output.

These were made by means of a special punch press which cut a flap of the corrugation material and bent it down into the channel at a 90 degree angle to the channel. After corrugations were cut to size, they went to the mirror punch where this operation was done. The Y layers are divided in half vertically by strip mirrors, and have wavebars on both sides of the SLIC. More details on the design and construction of the SLIC and of a prototype can be found in references (37,38).

The Pb-Al laminates were made by first laying out the bottom aluminum layer on a suction table, applying a layer of adhesive, rolling out the lead layer on top of this, followed by another adhesive layer, and finally the top aluminum layer. The lead sheets were cut 1" undersize so that a 1" aluminum strip could be inserted around the edges. Epoxy was also applied here, to ensure no delamination, and to prevent scintillator from contacting the lead. The laminates were then routed to exact size using an 8 by 16 foot routing template.

Once completed, the laminates were transported to the taping table using an array of suction cups lifted by a fork-lift. On this table the teflon tape was

applied using another tape-laying machine. To tape the back of the sheet, the table would be tipped vertically, then a lifting bar affixed to the top, and the sheet picked up with a crane, flipped over, and put down on the table again.

When the taping was complete, the laminate was picked up by crane and carried to another tilting table where the corrugations were attached. Pre-cut pieces were arranged on the table, which had alignment marks around its periphery for positioning them properly. One by one, the corrugations were clamped down in place by non-marring clamps, rivet holes drilled with a high-speed aircraft drill (with a vacuum cleaner to suck away the chips), and the corrugations riveted down using a standard pneumatic rivet squeezer. When all the corrugations were riveted down, the table was again tipped vertically, and the laminate lifted by crane and placed into the tank.

Using shifts of 5 to 7 student workers 24 hours a day, construction took several months.

iii. SLIC CALIBRATION

For good reconstruction efficiency and mass

resolution of final states, it is important to have good energy resolution in the electromagnetic calorimeters. The layer thickness, type of scintillator, and light collection scheme of the SLIC were all chosen to give good intrinsic resolution, but good total resolution over the face of the SLIC requires accurate calibration of the individual counters. Calibration of the SLIC took place in several steps, using a variety of schemes.

First the gains of the counters were crudely matched by adjusting high-voltages and looking at light pulser signals. It was assumed, on the basis of experience from earlier experiments, that in most cases a counter, once calibrated, would maintain its calibration roughly, but drift slightly over time. To correct for these (hopefully small) short term fluctuations, light puler events were used. Each wavebar/PMT assembly was fitted with an optical fiber which carried light pulses from the light pulser system. The online monitoring program sent pulses to the SLIC counters at a designated point in every monitor cycle (i.e., about every 2 hours). If any counters deviated too far from the benchmark values, an online error report was issued. Also, these data

were written to tape, and were subsequently analyzed by the offline monitor and written out in run-number indexed calibration files for use by the calorimeter reconstruction program.

The pedestals were handled in a totally analagous way, except here, instead of a light pulse, the monitor program simply issued a false gate to the ADC's between spills. These quantities too, were monitored online and also made into offline calibration files.

The initial GeV/count calibration constants for the SLIC were obtained in a special 5 GeV electron run taken very early in the running period. In this process, the electron beam was tuned to 5 GeV and a special gymballed steering magnet was installed in place of the target. With this magnet it was possible to steer the 5 GeV beam over almost the entire face of the SLIC, and thereby generate calibration data for each counter at several positions along its length. Because of difficulties in tuning the beam to 5 GeV, because the SLIC PMT's and ADC's were not well debugged before this run, and because the light pulser system was not completely understood at the time of the run, this data ultimately only gave a starting

point for the calibration. (This data was also used to confirm the attenuation lengths measured in the muon calibration, discussed below.)

Most of the U and V counters were calibrated by using tracked e^+e^- pairs produced by non-hadronically interacting photons in the target. These pairs are produced with essentially no p_+ and are simply bent by the magnets and lie in a horizontal plane through the middle of the spectrometer. The corner U and V strips, as well as all but 2 of the Y counters do not cross the pair plane and cannot be calibrated in this way. Since the intensity of pairs is tremendously higher near the beam axis than near the edges, it was necessary to install a special trigger requiring at least one electron track within 2 feet of the edge of the SLIC. This was done by placing 2 foot paddle counters on either side of the SLIC, in coincidence with the normal pair trigger, which used a fan-in of the central 3 SLIC Y counters on either side. Most of the events coming in on this trigger actually turned out to be 2 pairs from multiple bremsstrahlung with a high energy pair creating the pair-plane part of the trigger, and a lower energy track hitting the paddle counter.

A unique, non-iterative method was devised for generating the calibration constants of these U and V counters. Suppose an electron hits the SLIC at horizontal position x (measured in counter widths), and that the energy in it's shower in a small region dx' located at x', is given by E(x'-x)dx'. Clearly,

$$\int_{\infty}^{-\infty} E(x'-x)\, dx' = E$$

with E the energy of the electron. The amount of energy E_I (x) measured by SLIC counter I, centered at x", (see figure 22a), will be given by

$$E_I(x) = \int_{x''-.5}^{x''+.5} A_I E(x'-x)\, dx'$$

where A_I is the calibration constant of this counter, to be determined. Suppose we now form the quantity C_I by integrating E_I (x)/E over all possible positions of the electron:

$$C_I = \int_{\infty}^{-\infty} dx \frac{E_I(x)}{E}$$

$$= \int_{\infty}^{-\infty} dx \int_{x''-.5}^{x''+.5} dx'\, A_I \frac{E(x'-x)}{E}$$

$$C_I = \int_{x''-.5}^{x''+.5} dx' \int_{\infty}^{-\infty} dx\, A_I \frac{E(x'-x)}{E}$$

$$= \int_{x''-.5}^{x''+.5} dx\, A_I$$

$$C_I = A_I$$

Thus, the integral we have formed is exactly the calibration constant we want. The function $E_I(x)/E$ is simply obtained by calculating the average pulse height divided by track energy for several bins in distance from the center of the counter. The calibration constant is then just the integral of this function. The shape of this function for a typical counter is shown in figure 22b.

This method has several attractive features. First, it is "diagonal", i.e., the calibration of one counter does not depend on those of its neighbors. For this reason, it is not necessary to solve for the constants with an iterative approach. Second, it does not depend on an explicit knowledge of shower shapes and how they change with track angle. The integral of such a shape is always just equal to the energy.

Third, it allows all the data to be used. Tracks which do not actually hit a particular counter can still be used to calibrate it.

Special pair runs were taken at intervals of about a month. Analysis of the first 7 such runs showed that the calibration constants did not change with time in the vast majority of counters, within errors of the pair calibration method (about 2%). This indicated that not only was the pair calibration method working, but also that the light pulser system was correctly tracking the gains of the phototubes, since the pairs provided and abolute baseline to check against. With the light pulser corrections left off, it was found that the calibration constants were not very much different, indicating that the drifts were small.

The Y counters, and those U and V counters which do not cross the pair plane, were calibrated with background muons. These are minimum ionising and deposit typically .5 GeV in a SLIC counter. Special muon calibration runs were taken from time to time throughout the run for this purpose (and also to calibrate the hadrometer). The constants for these counters were adjusted so that all minimum ionising

peaks fell at the same value. These data were also used to find the attenuation constants of the SLIC counters.

Further calibration was possible using tracked isolated electron showers in the SLIC. The track momentum calibrates the energy scale, and one further requires that U, V, and Y views give the same energy.

Finally the mass of the pi-zero from reconstructed can be used to set an overall energy scale for the entire detector.

The energy and position resolutions of the SLIC for isolated electromagnetic showers are $12\%/\sqrt{E}$ and 3 millimeters, respectively. For typical reconstructed events, the energy resolution was about $15\%/\sqrt{E}$.

b. OUTRIGGERS

i. COUNTERS

The outriggers, so named because two long counters straddle the beamline, measure the positions and energies of photons and electrons at large angles to the beam, which are outside the vertical acceptance of the SLIC. They can also provide an energy deposit value for other incident particles if necessary. The location of these counters is shown in figures 23 and

24.

The outriggers do not reduce the acceptance of M2 to charged tracks substantially. Rather, their location is a consequence of the fact that the spectrometer is divided, roughly, into a "high" momentum part and a "low" momentum part. Low momentum particles typically emerge from the targer at larger angles, and those with $\theta_y \geq 40$ mr will hit the outriggers. It would have been unfeasible to make magnet apertures and detector sizes large enough to handle the highest and lowest momentum particles simultaneously.

The construction of the outriggers is shown in figure 25. They consist of two identical modules, one above the beam and one below, each of which has 16 layers of 1/4 inch lead interleaved with 16 layers of plastic scintillators for a total of 18 radiation lengths. Eight of the layers, called X layers are divided into 23 vertical optically isolated strips, which feed into wavebars and PMT's just as on the SLIC. The 8 Y layers are comprised of 15 horizontal 1.25 inch strips. The protruding ends of the 8 scintillator strips of the successive Y layers were formed into light guides which are coupled to PMT's.

All PMT's are 2 inch RCA 4900's, and had 14 mil conetic magnetic shields, followed by iron jackets, to protect them from the fringe fields of M2. The anode signals are read out with LeCroy 2280 ADC's by the data acquisition system, and the dynode signals are summed and added into the HADRON sum in the low level trigger logic.

ii. OUTRIGGER CALIBRATION

Most of the outrigger calibration was done using the background muon flux, in special muon runs. This data was analyzed offline to establish gains and attenuation constants for the counters. There were also a few electron runs in which the outriggers were lowered into the electron beam of known energy. The outriggers were also monitored online by the light pulser system.

5. RECOIL DETECTOR

a. RECOIL SPECTROMETER

The recoil detector, a set of PWC's and scintillator layers of cylindrical geometry surrounding the hydrogen target, was used to determine four-vectors of tracks emerging at large angles from

the hadronic vertex, as well as to provide signals to the trigger processor for generating recoil triggers.

A particle emerging from the target will first pass through 3 cylindrical PWC's, each with longitudinal anode wires for determining azimuthal angle, and circumferential cathode wires, which measure polar angle. The particle then enters the scintillators, called the A, B, C, and D layers, which are divided into 15 compartments, called sectors, in azimuth, each of which subtends 22.1 degrees. The A and B layers are of plastic scintillator, while C and D are actually comprised of compartments filled with liquid scintillator. A sixteenth sector is uninstrumented and houses support members for the PWC's and scintillator tank, as well as PWC readout cables. This sector introduces a dead region of 24.5 degrees, so that the acceptance in ϕ is about 93%. The lengths of the layers is about 2.5 meters, making the typical minimum θ of recoil tracks about 25 degrees. A schematic of recoil counter construction is shown in figure 26.

The recoil detector was designed primarily to identify single protons from so-called diffractive production of forward states in the $c\bar{c}$ mass range,

i.e. about 2-11 GeV/c^2, although it is also useful for providing information on events with multiple recoil tracks, i.e. for non-diffractive events. Monte-carlo studies of the four-vectors of such recoil protons were done to determine the thicknesses of scintillator layers, which were chosen to allow π-p discrimination by comparing the relative energy deposits in the layers to those expected from Bethe-Bloch dE/dX predictions. This information is also used to deduce the kinetic energy of the proton. Most protons are expected to range out in the scintillator.

The four scintillators have PMT's optically coupled to their downstream ends. The A layer has 3 tubes, B has four, C has two, and the D layer, three. Anode signals are carried to the LeCroy 2280 ADC's for data logging, while the dynode signals go into special fast ADC's for input to the trigger processor. The A layer also has one tube at the upstream end. Timing signals from the upstream and downstream tubes on this layer are used to determine an end-to-end (EET) timing measurement of the z position of the particle passing through it. This value can be used to resolve ambiquities when more than one track is present, and

as a consistency check. The average of the time values from the EET tubes is also used as a time-of-flight (TOF) measurement which can help in determining particle type for particles which stop in the A layer.

The PWC's have a three layer construction as shown in figures 27 and 28. The inner cathode is aluminized mylar and is held at ground. The anode wires on all chambers have a 4 millimeter spacing and are stretched on a frame having two end rings with three equally spaced support rings between them. The inner chamber has 268 anode wires, ganged in twos, the middle has 536, ganged in fours, and the outer has 804, ganged in sixes. Thus the granularity of the anode wires in θ is the same for all three chambers. Anode signals are processed on anode boards, sixteen to a board. Each in-time hit wire sets a bit in a shift register, which is read via CAMAC by the data acquisition system. Anode wires are at nominally 2500 volts. The cathode wires are flattened copper and are glued with 1.5 millimeter spacing to a mylar cylinder. Each chamber has 1312 cathode wires, which are ganged in twos into the preamplifier-discriminators. Typically a cluster of about 6 wire pairs will fire

when a track passes through the chambers. The readout scheme calculates a centroid and width for each such cluster and quickly (150 ns/cluster) sends these values to the trigger processor for use in creating a trigger.

The PWC's are filled with a gas mixture of 82.5% argon, 15% isobutane, and 2.5% methylal.

b. RECOIL DETECTOR CALIBRATION

The recoil detector was calibrated with single clean recoil protons from data events. For such events, there are no ambiguities, and the z position measured by the cathode is used to calibrate EET. The kinetic energy measurements are calibrated by comparing the observed pulse heights to Bethe-Bloch predictions for different mass and kinetic energy hypotheses in an iterative process which ultimately produces a set of 12 calibration constants for each of the 15 sectors. There are three constants per layer, which are basically an overall additive constant, an overall multiplicative constant, and an attenuation length. The recoil trajectory and results of energy reconstruction are used to predict the time-of-flight value, which is used to calibrate the measured TOF values.

To minimize complexity in the trigger processor calculations, all sectors have a single set of calibration constants in the trigger processor load. For this reason, gain matching was carried out every few weeks to reproduce as nearly as possible the calibrations expected by the trigger processor. This was done using the light pulser system. The gains of the PMT's were also monitored online by the light pulser system. The recoil detector is discussed more fully in reference (33).

6. HADROMETER

a. COUNTER

The hadrometer is a hadron calorimeter consisting of 36 3/8 inch thick scintillator layers interleaved with 36 1 inch thick iron plates, for a total of 6 interaction lengths. The scintillator layers are segmented with a 5.7 inch width and are oriented either vertically (X view) or horizontally (Y view). The calorimeter is segmented longitudinally into a front module and a back module, and within each module, 9 successive layers of scintillator in a given view feed via lucite light pipes into a single 5 inch EMI 9791KB PMT. There are 33 X counters and 38 Y

counters (19 each side) in each module. The location of the hadrometer in the spectrometer is shown in figure 24, and its construction in figure 29.

In construction of the hadrometer, first the steel plates were welded in place, and then the completed 9-layer scintillators were inserted as units.

The phototube anode signals are read out by LeCroy 2280 ADC's, while the dynodes are summed and become part of the HADRON fan-in for the tag-H trigger.

In the data analysis, the hadrometer provides a measurement of the energy and position of hadronic showers. Because of the intrinsically poor energy resolution of hadron calorimeters, (in this case, $75\%/\sqrt{E}$), the energy information is useful only when a crude number is adequate, e.g., for the hadronic trigger, or to differentiate hadrons from muons, which are minimum ionising and deposit about 2 GeV. Also, the hadrometer positions can be matched with charged tracks, and the hadrometer is the only source of energy and position information for neutral hadrons.

b. <u>HADROMETER CALIBRATION</u>

The online program generated light pulser events to monitor the PMT gains and pedestal events to monitor pedestal shifts. These events were also written on tape and analyzed offline to create calibration files for use by the reconstruction programs.

The absolute gains and attenuation functions of the counters were established by using data from periodic muon runs, and also a few special runs with a tuned pion beam.

7. CERENKOV COUNTERS

a. COUNTERS

Pions, kaons, and protons identification in the forward spectrometer is effected by two threshhold Cerenkov counters, called C1 and C2. The location of the counters are apparent from figure 24, while the counters themselves are detailed in figures 30 and 31. Information on dimensions, mirror sizes, gas mixtures, and particle threshholds is given in tables II and III. For momenta from 5 to 20 GeV/c, pions are distinguishable from kaons and protons. For momenta from 20 to 36 GeV/c, all three types of particles are distinguishable. From 36 to 69 GeV/c, protons are

distinguishable from pions and kaons.

The Cerenkov counter bodies are constructed of 1/4 inch aluminum I beams. The upstream end of C1 extends inside the field region of M1 and is made of fiberglass to prevent damage from eddy currents. The location of C1 necessitates a 2-bounce optics system. The optics for C1 and C2 are illustrated in figure 32. The upstream and downstream ends of both counters are sealed by thin flexible windows of vinyl and aluminum laminate. Both counters were mounted on rails to allow positioning and removal. The Cerenkov mirrors, which were slump-molded from acrylic sheet and aluminized, are suspended by dacron filaments. In C2, a 3 centimeter gap is left between the upper and lower halves of the mirror plane to avoid collecting light from the pair plane. The mirror segmentation and suspension systems are shown in figure 33.

The winston cones for light collection are made of epoxy. These are mounted on 5 inch RCA 8854 PMT's whos anode signals are digitized by LeCroy 2249 ADC's and subsequently logged onto tape. Also, the dynode signals are used in the dimuon trigger and in other special test triggers.

b. <u>CERENKOV CALIBRATION</u>

The index of refraction of C1 was monitored using a gas chromatograph. In C2 the pion threshhold, determined using reconstructed tracks, was used to determine the refractive index.

Mirrors were surveyed in initially, and their positions verified during the 5 GeV electron run. Subsequently, the mirror positions were monitored using reconstructed tracks. The winston cones were aligned using light beams before the counters were sealed up. The PMT's and ADC's were monitored online with the light-pulser system. The pulser events were also written on tape and used to create calibration files for the reconstruction programs.

8. MUON WALL

a. MUON COUNTERS

Directly behind the hadrometer is a four foot thick wall of steel which, together with the steel in the hadrometer itself, is sufficient to range out all but a small fraction of muons produced in hadronic showers. Thus the only particles exiting the steel wall are muons from the event vertex (or perhaps background muons) above some minimum cutoff momentum (about 5 GeV/c). The muon wall is simply an array of

18 and 24 inch wide scintillator strips with lucite light pipes and 5 inch EMI 9791KB PMT's. The layout of the wall is shown in figure 34, and is discussed again in the section on the dimuon trigger.

The signals from each PMT feed into discriminators, the outputs of which are used to set a latch bit, to start a TDC, and as an input to the dimuon trigger. The TDC value is used offline to measure the Y position of the muon hit in the counter.

b. MUON WALL CALIBRATION

The counter efficiencies were measured with a paddle counter telescope (triggered by background muons) at the near end and far end of each counter. All counters were essentially 100% efficient near the PMT, and typically about 98% efficient 7 feet from the PMT. The TDC T_0's and gains were measured offline with reconstructed tracks.

C. TRIGGERS

1. TAG-H

This trigger is the core of all the experimental triggers, with the notable exception of the dimuon trigger discussed below. It is a coincidence between

tag, which is supplied by the tagging system and simply indicates the presence of a tagged photon, and H, which indicates the presence of energy in the calorimeters that is consistent with a hadronic interaction. To form H, the dynode signals from the hadrometer and SLIC (Y view only, excluding pair plane) are summed, in the linear combination $E_H = E_{SLIC} + 1.25 * E_{HAD}$. The tag-H trigger required that $E_H > .3 * E_\gamma$. This is equivalent to requiring that $E_H > .3*(E_e - ETOT)$, where ETOT is the total energy in the tagging system, which is in turn equivalent to $E_H + .3*ETOT > .3*E_e$, where $.3*E_e$ will simply become the equivalent discriminator setting for tag-H. The outrigger dynode sum was discriminated and or-ed in with HADRON. The logic diagram of tag-H is shown in figure 35. The electromagnetic background, which is 200 times larger than the hadronic interaction rate, was reduced to a level about equal to the hadronic rate by use of the tag-H trigger. The efficiency of the tag-H trigger was measured to be 97 ± 2 percent.

2. RECOIL TRIGGERS

Recoil triggers are generated by the trigger processor. This is a unique trigger processing system

which uses high-speed ECL circuitry and memory-look-up (MLU) units to make complicated triggering decisions, involving track finding and particle identification, in a few microseconds. This system is discussed in detail in references (26,27,28). Basically, the trigger processor uses information supplied to it by the recoil spectrometer to decide if a hadronic event (tag-H is a prerequisite to recoil triggers) possesses a single well identified recoil proton emerging from the must upstream hadronic vertex. To make this decsion, the processor actually reconstructs tracks in the recoil PWC's, matches these with EET information in the recoil calorimeter, and attempts to identify the recoil particle as a pion or proton from its energy deposits. When a clean proton is identified, a missing forward mass is calculated from the four-vectors of the incident photon and the recoil proton. The recoil triggers are defined by:

1. Recoil 1: $0.0 < M_X < 2.0$ GeV/c^2

2. Recoil 2: $2.0 < M_X < 5.5$ GeV/c^2

3. Recoil 3: $5.5 < M_X < 11.$ GeV/c^2

The recoil 1 trigger was heavily prescaled to allow only small number of low mass events to be recorded for calibration purposes. The ρ events, for instance, were useful as a check of the track reconstruction program.

The process $\psi \to e^+e^-$ is expected to come in under the recoil 2 trigger since the ψ has a mass of 3.1 GeV/c^2. The tag-H is provided by the high energy electrons hitting the SLIC. Since this trigger is biased heavily toward elastic production, the dielectron mode will be used only as a crude check of the elastic cross section. We shall return to this point later.

3. DIMUON TRIGGER

The efficiency of the recoil trigger for ψ is rather low, due in large part to fact that many of the protons have low $-t$ and do not escape the target. Also, the recoil trigger is biased toward elastic production. The dimuon trigger was implemented to allow detection of ψ at a higher rate and to provide an unbiased ψ sample.

This trigger utilized dynode signals from the muon wall counters to identify candidate dimuon

events. It consists of two parts, here called MEW (Mu East-West) and MUTS (MUon TeleScope). MEW is designed to pick up the more symmetric decays in which one expects (for the elastic case) to find the muons in an East-West or Up-Down configuration. MUTS is designed to pick up many of the asymmetric decays where one muon is very fast and travels down the center of the spectrometer into MU16, and the other is slower and hits some other muon counter. Thus, MEW is a coincidence between the East and West sides of the muon wall (or between MU14 and MU18, directly below and above the central counter), and MUTS is a coincidence between the central MU16 counter and the outer muon counters. To reduce the number of accidental triggers, a coincidence with C2 was required for MEW, while the Pre-C and Caboose counters served the same purpse for MUTS. The Pre-C and Caboose counters are simply scintillator paddle counters; their locations are shown in figure 36. The dimuon trigger logic is:

$$\text{DIMUON} = \text{MEW} + \text{MUTS}$$

$$MEW = [(\mu_6+\mu_8+\mu_{10}+\mu_{12})\cdot C_E]\cdot[(\mu_{20}+\mu_{22}+\mu_{24}+\mu_{26})\cdot C_W]$$
$$+ (\mu_{14}\cdot C_{DN})\cdot(\mu_{18}\cdot C_{UP})$$

$$MUTS = (Pre\text{-}C\cdot Caboose\cdot\mu_{16})\cdot(\mu_8+\mu_{10}+\mu_{12}+\mu_{18}+\mu_{20}+\mu_{22}+\mu_{24}+\mu_{26})$$

C_E, C_W, C_{UP}, and C_{DN} are fan-ins of the east, west, top, and bottom counters of C2. The logic diagram for the dimuon trigger is shown in figure 37.

D. DATA ACQUISITION SYSTEM

The data acquisition system is outlined schematically in figure 38. The Fermilab standard RSX-MULTI online system provided a user-oriented environment on the PDP11/55 in which data taking runs could be initiated and ended, and through which a variety of user-defined quantities could be monitored, with graphics displays and MULTI commands.

MULTI also interacted with a stand-alone data acquisition system which when prompted by an event interrupt from a high-level trigger, read the data from the detectors out of all the CAMAC modules via 3 Jorway model 411 CAMAC branch drivers. The data was initially stored in a fast bank-switchable bulk memory

system; during the interspill period the data was transferred to one of Tagged Photon Lab's two 6250 BPI magnetic drives. Typically, about 50 events of all types were recorded per beam spill.

MULTI also controlled the data monitoring program. This program had the following functions:

1. Generate calibration events such as pedestals, light pulser events, and drift chamber pulser events.

2. Compare data from these events with benchmark values stored on disk.

3. Monitor high-voltages, low-voltages, magnet currents, mean chamber multiplicities, data integrity for the recoil system, tagging system calibration, scalers, etc.

4. Generate warning messages when any quantity was outside of acceptable limits.

IV. DATA ANALYSIS

A. PRODUCING THE ψ SIGNAL

During a 3 month data taking run in Spring of 1981, at an electron beam energy of 170 GeV, 7592374 triggers of all types were written onto 255 6250 BPI tapes. This data set represents .994E11 live-time-corrected tagged photons on target. All tapes were run through two sequential analysis passes on the Fermilab CYBER 175's. In Pass-1, the drift chamber charged track reconstruction, recoil counter analysis, part of the Cerenkov reconstruction, and part of the tagging analysis were carried out. Each raw data tape created three partially full Pass-1 output tapes to allow room for additional Pass-2 information. In the second pass, the electromagnetic and hadronic calorimetry analysis were carried out, as well as the remainder of the Cerenkov and tagging analysis. Particle identification, using the Cerenkov for π/K/p, and the calorimeters and muon wall for μ and e, was also done. The electron and muon identification programs are discussed more fully later. Each Pass-1 segment (1/3 of a raw tape) was used to create one Pass-2 output segment (which still

retained the raw data). At this stage the main-line data reduction was complete and the tapes could be stripped to look for specific physics signals.

A stripping program was written to select both dimuon and dielectron candidates from the Pass-2 ouptut tapes and write them onto special condensed files. The stripping selected roughly 120 dimuon candidates and 150 dielectron candidates, out of a total of some 30000 beam events, from each complete three-segment Pass-2 output tape. Cuts were left rather loose on this initial stripping pass. They are outlined below.

For dimuon candidates, at least one pair of tracks had to exist which satisfied the following cuts:

1. Opposite charge

2. Distance of closest approach of the two tracks less than 2 inches.

3. Position of closest approach within beam spot.

4. Invariant mass greater than .5 GeV/c^2 (to reduce the number of low mass background events written out)

5. Total momentum of two tracks at least 30% of tagged photon energy.

6. At least one of the tracks flagged as a muon in Pass-2.

7. The other track, if not so flagged, must have an energy deposit in the hadron calorimeter which is consistent with minimum ionising.

Cut 5 could introduce a bias in the z distribution, but, as we shall see, the efficiency for $z \lesssim .4$ is essentially zero anyway.

A track was identified as a muon in Pass-2 if

1. A muon counter gives x (from counter position) and y (from TDC) consistent with track position at muon wall.

2. Hadrometer energy deposit is consistent with

minimum ionising in magnitude, width, and front-to-back ratio.

In the final analysis, only 4% of dimuon tracks had not been flagged as muons in Pass-2, indicating that inefficiencies in the muon identification technique were small.

For dielectron events, the cuts used were:

1. At least two tracks are consistent with being electrons based on the ratio of SLIC energy to drift chamber momentum, and, for tracks below 20 GeV, based also upon shower width in the SLIC. Four-vectors of photons consistent with being bremsstrahlung photons radiated by the electrons are added in to the four-vectors of the corresponding electrons.

2. Neither electron consistent with being from a beam pair (i.e., Bethe-Heitler electron-positron pairs from photons that did not interact hadronically in the target).

3. Each track has > 6.0 GeV/c momentum.

4. Total momentum of the two electrons is at least 30% of the tagged photon energy.

5. Invariant mass of electron pair is at least .5 GeV/c^2.

A clear signal was seen in both dimuon and dielectron channels after the initial stripping pass, but backgrounds were still rather large. When the stripping pass was complete, the stripped events were copied onto summary tapes. Then a ψ analysis program was run on these tapes, which attempted to reduce the background by more cleanly identifying muons and electrons.

The additional new cuts for the dimuons were:

1. Total momentum of two muons less than 220 GeV/c (to get rid of tracks with mis-measured momenta).

2. Distance of closest approach less than .4 inches.

3. Tighter cut on vertex position.

4. SLIC energy less than 2.2 Gev for each track (i.e., consistent with minimum ionising; the minimum ionising peak is at about .5 GeV, with a Landau tail that is significantly populated out to 2 GeV or so.)

5. Each muon has momentum greater than 9 GeV/c.

6. (Calorimeter energy)/(Drift Chamber momentum) is less than .3 for each track (to cut out low energy pions that might be identified as muons)

7. Less than 9 good tracks besides the 2 muons.

8. If more than one pair of tracks pass all cuts, take the highest energy pair.

The final vertex distributions are shown in figure 39. These distributions are quite clean: the widths of the X and Y distributions are comparable to the beam size, and the Z distribution cuts off fairly cleanly at the front and back ends of the target. The sum of all cuts had an estimated efficiency of .93 ± .05,

determined by estimating the number of ψ's above background before and after making the cuts. This is discussed again in the section on efficiencies. The final dimuon mass spectrum is shown in figure 40. There are 147 events in the range $2.8 \leq M(\mu^+\mu^-) < 3.4$ GeV/c^2.

For dielectrons, in the background reduction program, more stringent cuts were made on the ratio of SLIC energy to drift chamber momentum, and the shower widths of all candidates were required to be consistent with being electromagnetic. The overall efficiency of all cuts was estimated to be $.92 \pm .05$. The final dielectron spectrum is shown in figure 41.

For the dimuons, it was found that requiring all events to have the dimuon trigger bit on did not affect any events with dimuon masses above 2.4 GeV/c^2. This cut was then made permanent.

After the background reduction pass, events were written onto small disk files for further analysis.

B. DEFINITION OF ELASTIC AND INELASTIC

After the ψ signal was isolated, programs were run which classified each event as elastic or inelastic. Since the dielectrons must come in on a

recoil trigger, this sample is biased strongly toward diffractive production, and therefore, in the absence of a detailed monte-carlo study of recoil trigger acceptance for non-diffractive events, it is not useful for a comparison of the relative magnitudes of elastic and inelastic cross sections. Rather, the totally elastic dielectron events are used as a crude check of the dimuon cross sections, as will be discussed along with the final results. In what follows, then, we refer only to the dimuon case in discussion of elasticity assignment. (In fact, a totally analogous procedure was followed for the electrons in defining their totally elastic sample.)

For our purposes, only the exclusive process $\gamma p \to \psi p$ is considered to be totally elastic production. Inelastic production, from a physics standpoint encompasses three classes of processes, namely,

1. $\gamma p \to \psi N^*$, the so-called quasi-elastic process,

2. $\gamma p \to \psi^* P$, with $\psi^* \to \psi X$, where charmonia are produced elastically and subsequently decay to ψ, and

3. $\gamma p \rightarrow \psi X$, the truly inelastic, hard scattering process.

From a theoretical standpoint, though, it is desireable to focus on the third process, i.e., truly inelastic production. As we shall see, the first process can be excluded by means of a cut in $z = E_\psi / E_\gamma$, and the second process can be "subtracted out", roughly, in a statistical way, even if it is not possible to completely reconstruct the events in all cases.

Operationally, an event is classified as inelastic if

1. Real forward tracks, photons, or hadronic neutrals are detected accompanying the ψ (forward inelastic),

   <u>or</u>

2. The recoil system data is inconsistent with the single recoil proton calculated from the incident photon and ψ assuming elastic production (recoil inelastic).

The remaining events are called elastic.

C. CLASSIFICATION OF EVENTS

1. FORWARD CLASSIFICATION

The forward inelastic classification was accomplished in a subroutine called CHOOSE. It was necessary to apply cuts to the additional particles detected in order to exclude backgrounds and spurious tracks, which could have forced truly elastic events to be labelled inelastic. The cuts in CHOOSE were:

1. For tracks:

    1. Must be seen in a calorimeter.

    2. Not consistent with being a beam pair.

    3. Must come from near the ψ vertex.

    4. Must be seen in at least D1 and D2.

2. For photons:

1. Energy of at least 3 GeV (to exclude untracked muons).

2. Not in pair plane.

3. Pi-zeroes must have a high probability of being real based on the two-photon mass and the possible presence of other combinations.

4. Hadronic neutrals must have energy above 9 GeV (to exclude untracked muons).

The motivation for these cuts, and their effect on the data are discussed in the section on uncertainties in assignment of events.

In figures 42 and 43 we present separate mass plots for forward elastic and forward inelastic events. The elastic and inelastic plots have 110 and 37 events, respectively, in the mass range $2.8 \leq M(\mu^+\mu^-) < 3.4$ GeV/c^2. The clear peak in the forward inelastic plot is conclusive evidence of inelastic ψ photoproduction.

2. RECOIL CLASSIFICATION

All forward elastic and inelastic events were also assigned as recoil elastic or inelastic by examining the data from the recoil spectrometer. We make the ansatz that the detected ψ was produced elastically. Using the measured four-vector of the ψ, constrained such that $E_\psi^2 = P_\psi^2 + M_\psi^2$, and the approximation $E_\gamma = E_\psi$, which is more accurate than the tagging energy for elastic production, we calculate, by imposing momentum and energy conservation, the polar angle, θ, azimuthal angle ϕ, and kinetic energy T of the recoiling proton. The errors in track momenta and slopes are also used to compute the errors predicted in θ, ϕ, and T.

It should be stressed that in the recoil classification, the four-vector of the recoil proton is calculated using only the ψ; no other forward particles (if present) are included. This method has the advantage that if forward tracks are missed, the event will still be classified as inelastic since the recoil proton will not match up. The disadvantage is that elastic charmonimum production will also be called inelastic since we do not include the extra tracks along with the ψ from the charmonium decay. There is really nothing that can be done about this

situation since it was not possible to totally reconstruct all the events. Thus there is an unknown amount of elastic charmonium production in our inelastic sample. There are, however, two points that mollify this problem: 1) Most of the inelastic forward events can be clearly identified as inelastic in the recoil system (and therefore not from charmonium production) because of the presence of extra tracks in the recoil system. 2) The ψ' cross section is known. ψ' production can be "subtracted out" approximately in a statistical way, as we shall see.

During the data processing, a standard recoil reconstruction package had been run on every event. This provided θ, ϕ, and momentum values, as well as particle identification information for all fully reconstructed charged tracks in the recoil spectrometer. Information on unmatched tracks and neutrals was also provided. This program matched cathode (θ) tracks to anode (ϕ) tracks by attempting to find an end-to-end-timing (EET) value in some sector which agreed with that predicted form the cathode track. The particle's type and momentum were determined from its energy deposit in the scintillator layers. The errors on measured quantities were also

provided. In a large fraction of the events, these θ, ϕ, and T values could be directly compared to those predicted from the ψ. Because of PWC inefficiency and noise, faulty data readout, interactions in the scintillator, confusion from background tracks or real extra tracks, and because the recoil program did not know the ψ vertex position a priori, the information from the recoil reconstruction program was not useful in some cases. For this reason an event display showing raw PWC hits, scintillator energy deposits, EET values, forward vertex position, and the predicted quantities was made for each event, and these were hand-scanned. The kinetic energy reconstruction was run again on each event using the predicted sector of the proton, and this information was also printed out on the event display. Knowledge of the vertex and predicted θ and ϕ allowed 2-hit tracks, which the reconstruction program did not always find, to be picked up.

In comparing the predicted with measured quantities an overall error was calculated as the sum in quadrature of errors on predicted and measured quantities. The size of the errors on predicted quantities depends on the measurement errors of the

forward tracks, however typical values are

1. σ_θ(pred) ~ 30 mr.

2. σ_θ(meas) ~ 20 mr.

3. σ_ϕ(pred) ~ 100-200 mr. (sector=380 mr.)

4. σ_ϕ(meas) ~ 40 mr.

5. σ_T(pred) ~ 25% (T > 40 MeV; worse below)

6. σ_T(meas) ~ 1%

In cases where the standard reconstruction package failed, the error in the measured recoil quantities was assumed to be the average error. Recoil tracks clearly emanating from the forward vertex were compared to the predictions. Events were labelled inelastic if:

1. At least 2 of θ, ϕ, T were off by 2σ or more.

   <u>or</u>

2. At least one of θ, ϕ, T were off by 3σ or more.

   <u>or</u>

3. No recoil proton is seen even though it should not have ranged out in the target. This is rare.

   <u>or</u>

4. A matching track is seen but there is clear evidence of an additional track(s). This is also rare.

The remaining events are called recoil elastic, and consist of two types:

1. A matching recoil track is found.

2. The recoil proton is predicted to range out in the target and none is seen. A kinetic energy of roughly 30 MeV or more is necessary for a proton to just reach the A scintillator layer. For about 36% of the totally elastic events, (elastic in recoil and forward

systems), the recoil proton ranges out before reaching the A layer.

D. DETERMINATION OF Z

After an event was labelled inelastic by CHOOSE, a modified version of CHOOSE, called OMNES, was used to calculate the four-vector of all forward particles excluding the ψ. The energy component of this four-vector can now be used to compute z through

$$z = \frac{E_\psi}{E_\psi + E_x(1)}$$

where $E_x(1)$ is the energy component of the four-vector. The cuts used in OMNES were identical to those in CHOOSE with two exceptions:

1. Tracks are no longer required to be seen in a calorimeter.

2. The photon energy cut was lowered to 2.2 GeV from 3.0 GeV.

It was assumed that, for truly inelastic events,

errors introduced by possibly spurious particles, due to the looser cuts, would be small in most cases in comparison to the total inelastic energy. A photon energy cut of 2.2 GeV will exclude all but a few percent of background muons while now allowing real photons in the range 2.2 to 3.0 GeV to be included in the total inelastic energy. OMNES thus allows the best possible estimate of the detectable forward energy. The "raw" z distribution from OMNES was plotted 1) with cuts as described above, and 2) with cuts identical to those in CHOOSE. The change in the z distribution was actually rather slight. The distribution for 1) is shown in figure 44a.

In principle the tagged photon energy can be used to calculate z by the formula

$$z = \frac{E_\psi}{ETAG}$$

The resolution of ETAG is, however, about 6.8%, which would give a sigma of 6.8 GeV for a 100 GeV ψ. For a z of .9 at 100 GeV, the total inelastic energy is only 10 GeV. Thus, the use of the tagging energy is undesireable at high z since 1) the fractional error

in (1-z) is large and 2) the calculated z may be larger than one, creating an ambiguity with elastic events.

There are also problems with using $E_x(1)$ from OMNES to calculate z. Although the tagging energy is too inaccurate for calculating z at high z, it was possible, by averaging over a number of events, to use it to determine that on average, only about 54% of the total inelastic energy was being detected. This can be seen by comparing figures 45a, 45b, and 45c. In figure 45a, the ratio $A = E_\psi$ /ETAG is histogrammed for elastic forward events. The mean is 1.052 ± .010, in good agreement with the known systematic 5% underestimate of the electron beam energy. In figure 45b, we plot $B = E_\psi$ /ETAG for those inelastic forward events that satisfy $E_x(1) < 2 * .068 *$ ETAG, i.e., we exclude the events with the largest values of $E_x(1)$. This was done to prevent the introduction of uncertainties due to possibly large fluctuations in the detected energy $E_x(1)$. The mean of this plot is .905 ± .022. The inclusion of all inelastic forward events does not significantly change the mean. In figure 45c, $C = (E_\psi + E_x(1))$/ETAG is plotted for the same class of events as in figure 45b. The mean is

.985 ± .019. Again, the mean does not change appreciably if all events are included. The quantitiy

$$Q_{abc} = \frac{C-B}{A-B}$$

is a measure of the mean fraction of the total inelastic energy that is detected. The result is Q_{abc} = .544 ± .151. Taking the inverse of Q_{abc} we see that to calculate z using $E_x(1)$ we should scale it up by a factor F = 1.84 ± .51. The error here is just the error on the mean factor. We expect a considerable spread in this factor on an event by event basis. If we assume that the mean of this spread is about half the correction, we obtain F = 1.84 ± 1.05. Thus we can calculate z by

$$z = \frac{E_\psi}{E_\psi + F \cdot E_x(1)}$$

This method will work best when $E_x(1)$ is small compared to the error in the tagging energy.

In practice, z was calculated using whichever of the two methods had the smaller predicted error. The condition $z \geq 1$ never occurred. The ETAG method was

employed for smaller z values, and the $E_x(1)$ method near z = 1. The resulting "corrected" z distribution is shown in figure 44b.

Information on the energies of recoil particles is not reliably known. We can, however, estimate the effect of these on the z value. (This is necessary only for forward elastic events since the energy missed in the recoil was included in the correction to $E_x(1)$). The mean θ of recoil tracks is something like 40 degrees. With typical p_+ values of 350 MeV/c, this indicates $p_{TOT} \sim 540$ MeV/c for recoil tracks. For two or three such particles, we thus expect 1-2 GeV in the recoil system. Thus, for the ψ energies in this experiment, events which are inelastic in the recoil system only can safely be assigned to the highest z bin, $.95 < z < 1.0$.

Since only about 54% of the inelastic energy is detected, it is important to check that inelastic events are not being called elastic in some instances. The CHOOSE program tabulates the number of tracks, photons, pi-zeroes, and hadronic neutrals which pass the cuts for each event. These quantities are histogrammed in figures 46a, 46b, 46c, and 46d. The total number of extra particles (where pi-zeroes count

as two) is shown in figure 46e. About 70% of the events have 2 or more inelastic components. Of those with only 1, many also had an additional track that did not hit a calorimeter or a photon(s) below 3 GeV. (The elastic events, though, usually showed little evidence for additional energy which failed the CHOOSE cuts.) It is thus unlikely that many inelastic events are classified as elastic. Two events were somewhat marginal, involving only a track of less than 1 GeV or a photon near the the pair plane. This type of event is treated in the following section on uncertainties in classification.

E. UNCERTAINTIES IN CLASSIFICATION

1. UNCERTAINTIES IN FORWARD CLASSIFICATION

The cuts in the CHOOSE subroutine were designed to prevent truly elastic events from being labelled inelastic due to the presence of uncorrelated or spurious tracks or photons. Four techniques were used to check the effect of these cuts on the classification of events.

First, the subroutine was run on elastic monte-carlo data which included background e^+e^- pairs

and background muons. The number of events which were classified as inelastic was negligeably small. Second the photon energy cut was examined. The SLIC cut of 3 GeV and hadrometer cut of 9 GeV ensure that less than 1% of untracked muons will be identified as photons, based on the measured spectra of minimum ionising particles in the SLIC and hadrometer. A plot of photon Y position at the SLIC, outside the pair plane, indicated no contribution from leakage of untracked pairs outside of the pair plane. Thus, the contribution to the inelastic events due to muon and pair background is negligeable.

Third, a z value was calculated, using OMNES, for events which had been labelled elastic by CHOOSE. Of the 110 elastic forward events, 4 had $z \neq 1.0$, with the mean z of these 4 being .98. Thus, $z \sim .98$ can be thought of as the "inelastic threshhold" for this experiment, above which elastic and inelastic cannot be reliably distinguished. In the forward inelastic sample, 2 events had $z \gtrsim .98$, for a total of 6 "marginal" events. The recoil system, however, resolved the ambiguity in 4 of these cases, labelling these events as inelastic, and thus leaving 2 events with potentially incorrect classification. Clearly,

for z $\gtrsim$ .98, in those cases where the deviation from elastic in the recoil system is less than our resolution, we can make no statement about incorrect classification: these events must simply be called elastic. However, we may estimate that for events not too far from inelastic threshhold, the probability of misidentification is about 50%. Thus we might expect that rather than 2, perhaps 4 are potentially misidentified. To reflect this additional uncertainty, the errors on numbers of elastic and inelastic forward events are increased by half this amount, or 2 events. This contribution is much smaller than that of the statistical errors. The numbers of events and their errors are discussed more fully in the final results section.

Finally, the 5 events which were found to be inelastic forward but elastic in the recoil were examined more closely to see if they might possibly be truly elastic. The largest z value of these was .86, indicating that they were truly inelastic

The case of ψ plus neutrals is a difficult one. Because it was necessary to put the photon energy cut at 3.0 GeV, events with multiple soft photons would be classified as elastic. Copious production of such

states, then, would introduce a systematic error in our inelastic and elastic fractions. A known source of such events is the process $\gamma p \rightarrow \psi' p \rightarrow \psi \pi^0 \pi^0 p$. Using the ratio $\sigma(\psi)/\sigma(\psi') = .20 \pm .05$ (15) and the branching fraction for $\psi' \rightarrow \psi \pi^0 \pi^0$ of 17% we predict about 3 events. A monte-carlo calculation gives a mean z of .84 for these events. At a photon energy of 100 GeV, this gives 16 GeV to be shared among 4 photons. Thus it is unlikely that even these events would be classified elastic.

As a rough check of the inelastic reconstruction efficiency, a search for ψ' production was made. Using the previously quoted cross section we predict 7 events in our inelastic sample into $\psi \pi^+ \pi^-$, where we have included the reconstruction efficiency for the ψ but not the additional pions. In figure 47 we present the forward mass spectrum for events with four tracks, total charge zero, and no extra photons or hadronic neutrals, where the muons are required to form a ψ. A peak of 4 events appears at the ψ' mass (3.685 GeV/c^2).

2. UNCERTAINTIES IN RECOIL CLASSIFICATION

In about 15% of the events, it was not possible

to make a clearcut decision on elastic or inelastic in the recoil system. The reasons for this were:

1. Confusion in PWC's due to delta rays or missing or spurious hits.

2. Protons interacting in the scintillator.

3. Errors on predicted quantities too large.

4. Recoil acceptance losses (tracks go into missing sector or out end of counter)

5. Recoil data not present or incorrect.

6. Recoil data self inconsistent.

However, in about 2/3 of these cases, it was possible to pick elastic or inelastic with high probability. In the remaining cases a guess was made based on all information available. An additional systematic error of .5 event was assumed for any event that could not be assigned with certainty to either the elastic or inelastic category.

V. EFFICIENCY CALCULATIONS

A. TRACK RECONSTRUCTION EFFICIENCY

A tracking monte-carlo, which attempted to mimic the true operating environment of the track reconstruction program by including noise hits, cross-talk, and inefficiency, was used to estimate the track reconstruction efficiency. The noise, cross talk, and inefficiency information was obtained from a detailed study of a small number of runs, and may only be valid for runs in that region of the data. The efficiency obtained was .80 ± .02 (statistical) for $\psi \to \mu^+\mu^-$, (i.e., about .90 per track), with an estimated systematic uncertainty of about 16 percent.

To account for possible time dependence of the track reconstruction efficiency, a study was made of ρ photoproduction for the same 170 GeV data sample. A plot was made of the number of events of the form $\gamma p \to \rho p$, $\rho \to \pi^+\pi^-$, per flux bin versus the total accumulated flux. This plot, in an ideal experiment, would be flat, indicating a constant reconstruction efficiency over time. Instead, the plot showed a central dip. The ψ was assumed to exhibit the same behavior, since it, too, is a two prong topology. The

statistics on the ψ sample are low, but there was evidence of a central dip for the ψ too. This dip was also seen in the same location in a plot of number of K^0 per run. On the other hand, the number of π^0 per event, which does not directly involve the track reconstruction, showed no dip. A correction factor equal to the average number of ρ per bin divided by the average of the largest 4 contiguous bins in the vicinity of the Monte-Carlo model run (where the reconstruction efficiency was presumably best) was applied to the track reconstruction efficiency. These factors were .74 ± .07 for MUTS and .60 ± .05 for MEW. These also include the fact that the MEW trigger was not functional for part of the run.

The ρ study was also used to map out the spatial dependence of the track reconstruction efficiency. A central inefficient region, or "hole" caused by the high flux of beam pairs was discovered, and its extent was mapped out by the positions of pion tracks from the ρ. This hole, which was then included in the elastic and inelastic monte-carlo's (discussed below), reduces the ψ signal by about 10%, after other factors are included. The .80 efficiency quoted above does not include the effect of this hole.

To estimate the effect of extra tracks on inefficiency for inelastic events, the tracking monte-carlo was run with a $\psi' \to \psi\pi^+\pi^-$ generator. This should be adequate since, as we saw, very few of the inelastic events have more than two additional tracks. The presence of the extra pions reduced the event reconstruction efficiency by only about 3%. This effect was then included in the inelastic efficiency.

B. ELASTIC MONTE CARLO

A monte-carlo was written with the following attributes:

1. $d\sigma/dt \sim e^{Bt}$ with B=4. Changing B from 2 to 20 did not measurably affect the results.

2. Vertex generated uniform in z within target.

3. ψ decays to 2 muons distributed as $1+\cos^2\theta$, where θ is measured with respect to the lab direction of the ψ as seen in the ψ rest frame. The data is consistent with this, the standard SCHC prescription, but statistics

are too low to rule out other distributions. The results have only about a 5% dependence upon the anglular distribution used.

4. Muons are projected through the spectrometer. All known acceptance losses and analysis cuts are taken into account. If two muons hit muon counters which would cause a dimuon trigger, the event is kept.

5. This monte-carlo did not do tracking. The track reconstruction efficiency was done separately, as discussed in the previous section.

The MEW part of the dimuon trigger contains a Cerenkov coincidence. This appeared to introduce an additional inefficiency in the trigger, as the ratio of MEW to MUTS in the data did not initially match the monte-carlo. By histogramming Cerenkov light for tracks from MEW events and those from MUTS events it was possible to measure this inefficiency, which was included in the monte-carlo. The final elastic reconstruction efficiency as a function of photon

energy is shown in figure 48.

C. INELASTIC MONTE CARLO

The philosophy in the inelastic monte-carlo was not to generate events explicitly according to a particular model, but to generate data-like events in a simple way, determine the efficiency as a function of $k = E_\gamma$ and z, and then demonstrate that the results are insensitive to the method used.

The inelastic monte-carlo diffractively generated forward masses from XMIN = $M_\psi + 2M_\pi$ to XMAX, with a t slope B of 4. Changing B from 2 to 20 did not measurably affect the results. The forward masses were generated from a distribution that fell linearly from XMIN to XMAX. The forward mass then decays to $\psi\pi^+\pi^-$ where the pions decay via two body phase space. Events generated in this way produce ψ with some p_+ and z distributions. By varying XMAX, it is possible to vary the p_+ and z dependence. XMAX was chosen to have the value $0.65X_0$ where X_0 is the maximum kinematically allowed forward mass that can be produced in the reaction $\gamma p \rightarrow M(X_0)p$. Choosing this value yielded a p_+ vs. z distribution which agreed

well with that predicted by Berger and Jones (5) over the range of z values accessible to this experiment, as shown in figure 49. Also, the resulting p_+ distribution had a mean value of .75, which is roughly comparable to the value .96 found for the inelastic data (we shall return to the inelastic p_+ distribution later). In fact the efficiency does not depend strongly on the value of XMAX used. In changing XMAX from $0.5X_0$ to $1.0X_0$, efficiency numbers changed about 20% near z = .4, and very little near z = 1., in spite of the fact that the p_+ distribution extended to unphysically large values for the case of XMAX = $1.0X_0$. Using the cross section predicted by Berger and Jones, which falls rapidly at low z, the total predicted number of inelastic events changed only about 10% when XMAX was changed from $0.5X_0$ to $1.0X_0$. In any case, the efficiency is not strongly dependent upon p_+, as seen in figure 50 where we present the inelastic efficiency for two bins in p_+.

The ψ was assumed to decay isotropically in its center of mass. Berger and Jones predict a nearly uniform distribution for high z and reasonable p_+ values, where most of the data lie. Using $1+\cos^2\theta$ or $\sin^2\theta$ changes the results by only about 5%.

The dimuon trigger and reconstruction "hole" were put in just as for the elastic monte-carlo. The overall inelastic efficiency is illustrated in figure 51 for several values of k. This efficiency, taken as a function of $k*z = E_\psi$, is almost identical to the elastic efficiency. It differs only slightly due to the different angular distribution used, p_+ effects, and the reduced track reconstruction efficiency for multiple tracks. In correcting inelastic events for efficiency, the efficiency was treated as a function of k*z and k, since E_ψ is known more accurately than either k or z, and since, once the E_ψ dependence is factored out, the efficiency now depends only weakly on k.

VI. RESULTS

Each dimuon event has now been categorized as elastic or inelastic in both forward and recoil spectrometers. The events are now broken down into seven categories based upon these classifications:

1. All events.

2. Forward elastic. Any recoil configuration.

3. Forward inelastic. Any recoil configuration.

4. Forward elastic, but recoil inelastic.

5. Forward elastic and recoil elastic, i.e., totally elastic.

6. Any inelastic, i.e., forward inelastic and/or recoil inelastic.

7. Inelastic with $z \leq .9$. This by definition excludes recoil inelastic.

In each category, the sum

$$N_c = \sum_i \frac{1}{\varepsilon_i}$$

is made, where ε_i is the efficiency of the ith event. This is the number of events corrected for efficiency, using the efficiency function(s) appropriate for that category.

The backgrounds under the elastic and inelastic mass plots (figures 42 and 43), along with their errors, are estimated by superimposing smooth background curves on the plots. A study of the recoil inelastic fraction of the forward elastic background was made for events with masses below the ψ in the range 2.0 to 2.6 GeV/c^2. This fraction was similar to that for events in the ψ mass range (i.e., about 30%), and was used to calculate the contributions of the background to events in categories 4, 5, and 6. The number of corrected background events was taken to be the raw number of background events divided by the average efficiency.

The statistical error in N_c is given by

$$\sigma^2_{N_c} = \sum_i \left(\frac{1}{\varepsilon_i}\right)^2$$

To this, the systematic errors, due to background subtraction and uncertainties in forward and recoil classification, are added in quadrature. In the case of inelastic events, there are additional systematic errors due to uncertainties in efficiency that are also added in at this point. These are due to: 1) Uncertainty in ratio of MUTS to MEW due to Cerenkov efficiency. Inelastic events have a higher fraction of MEW events than elastic. This is about a 4% error. 2) Lack of knowledge of the correct p_+ vs z distribution (about 5%). 3) Uncertainty in the effect of confusion in the hadrometer on inelastic events (5%). There are also additional systematic effects for both inelastic and elastic events which effect only the overall normalization. These are discussed below. The systematic errors added in thus far are comparable in size to the statistical errors.

The raw numbers of events, estimated backgrounds, and corrected numbers of events, along with their errors, are given in Table IV. In figure 52 we present the corrected z distribution of the corrected

number of events. This plot contains only inelastic forward events. In figure 53 the same plot is shown with recoil inelastic events added in. Recall that the recoil inelastics are defined to be in the highest bin. Also it should be borne in mind that the errors on z for forward inelastic are often of the order of one bin.

In Table Va we present the ratios of corrected numbers of events in categories 2 through 7 to that for category 1 (all events). These are the fractions of ψ events produced with the attributes of each category. The fractional statistical error on these ratios is assumed to be given by that for the ratios of the raw numbers of events. Systematic errors due to background subtraction, uncertainties in assignment, and uncertainties in efficiency (inelastic only) are added in quadrature. It should be remembered when considering these ratios, as well as the cross sections presented below, that the efficiency for detecting events with $z \lesssim .4$ is essentially zero. Therefore, if the true z distribution of the data were heavily populated at low z, the inelastic numbers presented here would be wrong. However, both the theoretical predictions

(3,5) and the measured z distributions of the EMC (16,20,29) and BFP (17,19,21) groups indicate only a small contribution from $z \lesssim .4$. (The EMC and BFP groups, though, also suffer from low acceptance at low z, although they can go a bit lower than .4)

Finally, the corrected numbers of events are divided by the total luminosity, resulting in the cross section for each category evaluated at the mean (over luminosity) photon energy of 103 GeV, where we have assumed a linear dependence of the cross section over the range of photon energies used. These are presented, with their errors, in table VIa. Note that there is an additional ~25% uncertainty in the overall normalization of the cross sections. The sources of this uncertainty are:

1. Uncertainty in the time dependence of the reconstruction efficiency as determined from the rho study (10%).

2. Uncertainty in the correct "best" value of the track reconstruction efficicency (16%).

3. Uncertainty in the characteristics of the "hole" in the drift chamber reconstruction (3%)

4. Uncertainty in the flux measurement (8%).

5. Uncertainty in the effect of analysis cuts (5%).

6. Uncertainty in the Cerenkov efficiency for the dimuon trigger (10%).

7. Uncertainties in the correct decay angular distribution of the ψ (5%).

In order to get a more accurate representation of <u>direct</u> ψ photoproduction, as opposed to cascade production, it is desireable to subtract out the cross section for charmonium production. The only measured non-ψ charmonium photoproduction cross section is that for the ψ′, which has recently measured (15) to be .20 ± .05 times the ψ cross section. In figure 52 we show the estimated contribution from ψ′ to the corrected numbers of events, based on this cross section. The z

dependence was determined by a monte-carlo study of the process $\gamma p \rightarrow \psi' p$ where $\psi' \rightarrow \psi \pi^+ \pi^-$. In Table Vb we present the fractions of ψ in each category with ψ' subtracted out, and in table VIb, the ψ' subtracted cross sections. Again, there is a ~25% uncertainty in overall normalization of cross sections.

The dielectron events were used as a crude check of the normalization of the cross sections measured with the dimuon events. As mentioned before, these events came in under the recoil-2 trigger, which is totally independent of the dimuon trigger. The dielectron events were assigned as elastic or inelastic in forward and recoil systems exactly as in the case of the dimuons. The result is that 37 ± 7 events were totally elastic. Then, using the dimuon events, we can, by counting the number of totally elastic dimuon ψ with a recoil trigger bit on, calculate the recoil trigger efficiency for elastic ψ production. This was found to be .27 ± .05, which is consistent with the value .24 obtained by folding together the efficiencies of the recoil PWC's, EET matching, kinetic energy reconstruction, t acceptance, etc. Using this efficiency, a dielectron monte-carlo similar to the dimuon monte-carlo, and the elastic ψ

cross section measured with the dimuon events, we expect to observe 34 ± 6 events. This indicates that

$$\frac{\sigma_e}{\sigma_\mu} = \frac{37 \pm 7}{34 \pm 6} = 1.09 \pm .3$$

The error on this ratio is, unfortunately, rather large, due to the low statistics involved, but it does give an indication that there are no serious normalization problems, since the dimuon and dielectron techniques are quite independent.

VII. DISCUSSION OF RESULTS

Let us first examine the data at face value. From Table Vb we see that

1. Only 51 percent of all ψ photoproduction is totally elastic (category 5). The remainder is inelastic.

2. Of the inelastic ψ production, only about 50% (category 7) has $z < .9$, i.e., has substantial energy accompanying the ψ. The z distribution, although not measured with great precision, is clearly peaked at high z (figure 53).

3. Some 73% (category 2) of ψ were accompanied by no additional forward particles. About 30% of these (category 4) are inelastic in the recoil system. This second result is in good agreement with the recoil elastic fraction measured in another photoproduction experiment (18).

Note that none of these numbers will change very much if we use the corresponding numbers before subtraction of the ψ′ (Table Va).

In Table VII a comparison is made of elastic (a) and inelastic (b) ψ photoproduction as measured in this experiment, by the EMC and BFP groups, and by the Fermilab Wide Band photoproduction group. (Fermilab Wide Band data were taken with deuterium and hydrogen targets.) For E516, BFP, and Wide Band, errors due to uncertainty in normalization are presented separately in parentheses. The Wide Band elastic cross section was calculated at 100 GeV using the parametrization of reference (18). In the case of elastic production, as can be seen in the table, there is a spread in the values reported, but the experimental errors are large, and, as shown, the definition of elastic is not exactly the same in all four cases. The term "forward elastic" is an acceptance-dependent quantity. For these reasons, it is probably not unreasonable to conclude that the four experiments are at least crudely in agreement on the elastic cross section.

The inelastic cross section, displayed in Table VIIb, is quite another story. The inelastic ψ muoproduction cross sections on iron, corrected for

nuclear effects and extrapolated to $Q^2 = 0$, are roughly a factor of 3 larger than the inelastic ψ photoproduction cross sections measured in this experiment. We have here limited our comparison to z values of .9 or less (.95 or less for EMC) to exclude most of the high-z peak, where, for all experiments, separation of inelastic from elastic is most difficult. Even with the slightly different definitions of inelastic for these experiments, it is difficult to understand a factor of 3. Using the cross sections from this experiment before ψ' subtraction does not, as shown, appreciably affect this result.

Since different experiments will have different systematics in overall normalization, we also compare, in Table VIIc, the ratio of inelastic to elastic production. Here the muoproduction experiments report inelastic ratios of .81 ± .08 to 2.4 ± .5 while the ratio for this experiment is .36 ± .07 (.46 ± .09 before ψ' subtraction).

The inelastic cross section was not explicitly measured in the Wide Band experiment (except for the recoil inelastic fraction, which as mentioned before, agrees with our measurement), but it was reported (18)

that the forward inelastic events constituted no more than about 8% of the total ψ sample. Although inelastic events will in general have a different efficiency than elastic events, this may be another indication that the inelastic cross section is smaller for photoproduction experiments.

The reasons for the discrepancy between muoproduction on iron and photoproduction on hydrogen are not known. The most obvious potential sources are:

1. The effect that the binding of the nucleons into an iron nucleus has upon inelastic cross sections may not be completely understood. (There is evidence that nucleon structure functions are different for free nucleons and those bound in nuclei (39,40), although this is not as large an effect as is observed here.)

2. It may be that a simple extrapolation to $Q^2 = 0$ is inappropriate.

On the other hand, the photoproduction results are closer to the second order perturbative calculations of Berger and Jones. As noted earlier, the total $z < .9$ inelastic cross section at 105 GeV in the Berger-Jones model is 2.9 nanobarns, which is within experimental error of the 5.1 ± 1.4 (± 1.3 normalization) value measured here. A value of $\alpha_s = 0.4$, as suggested by the four-flavor model (5) gives a predicted value of 5.2 nanobarns (see also ref. 43). Conversely, our experimental value may really be a bit too large due to the possible presence of elastic charmonium production that has not been completely subtracted out. It is also interesting to note that the ratio of inelastic to elastic of .36 is in accord with the qualitative notion that the the inelastic cross section should be of order α_s times the elastic cross section.

Finally, we present in figure 54 the p_+ distribution for totally elastic (categ. 5) and forward inelastic (categ. 3) events. Because of the small numbers of events involved, it is not instructive to subdivide these plots further. It is clear that the p_+ distribution of the inelastic events is flatter, as predicted by second-order perturbative

QCD (5,10,14). The mean p_+ of the forward inelastics is .96 ± .11 GeV/c, and the mean for the totally elastics is .39 ± .03 GeV/c. The forward elastic events (not shown) have a distribution similar to the totally elastic and have a mean p_+ of .50 ± .04. A flatter p_+ distribution for inelastic events is also reported by both the EMC (16) and BFP (17) groups.

APPENDIX A - FIGURES

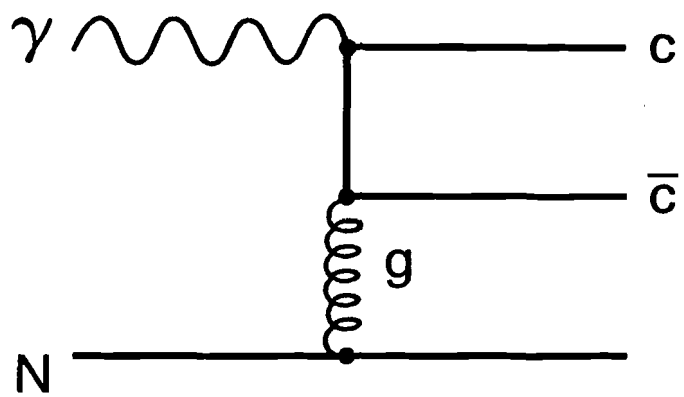

γGF: 1st ORDER QCD

Figure 1

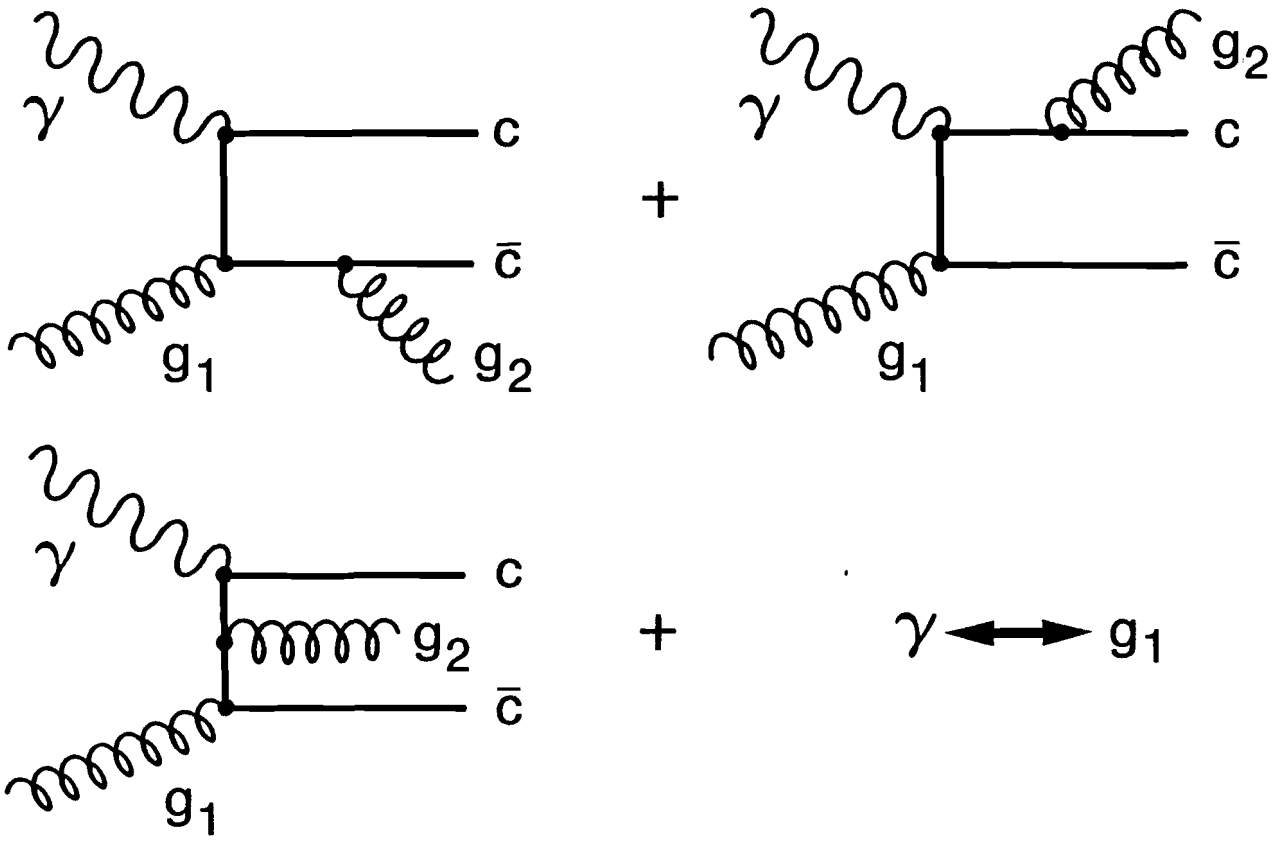

γGF: 2nd ORDER QCD

Figure 2

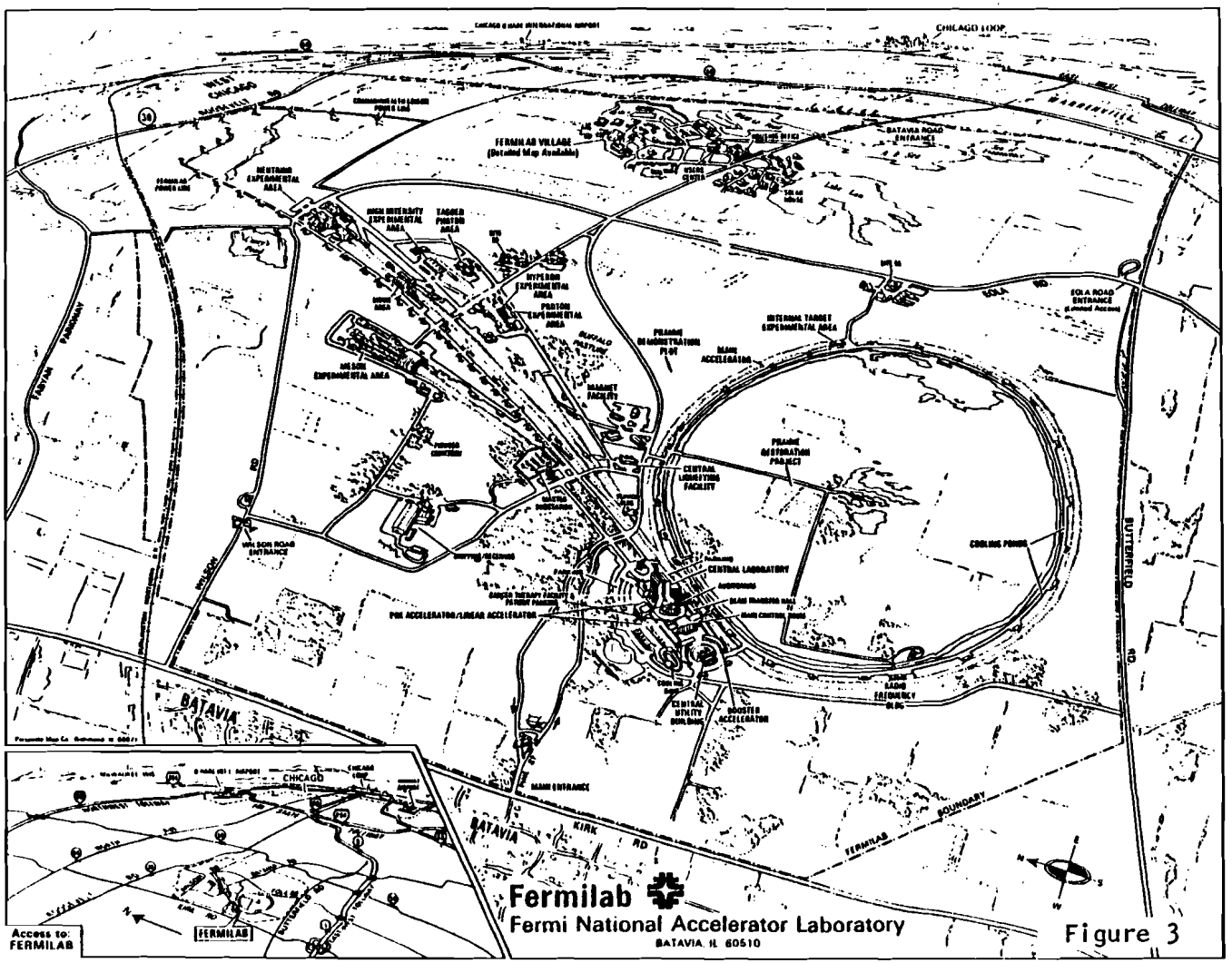
CHICAGO LOOP
FERMILAB VILLAGE
(Detailed Map Available)
BATAVIA ROAD ENTRANCE
NEUTRINO EXPERIMENTAL AREA
HIGH INTENSITY EXPERIMENTAL AREA
TAGGED PHOTON AREA
HYPERON EXPERIMENTAL AREA
PROTON EXPERIMENTAL AREA
MESON EXPERIMENTAL AREA
MAGNET FACILITY
PRAIRIE DEMONSTRATION PLOT
MAIN ACCELERATOR
INTERNAL TARGET EXPERIMENTAL AREA
EOLA ROAD ENTRANCE
PRAIRIE RESTORATION PROJECT
CENTRAL LABORATORY
COOLING POND
WILSON ROAD ENTRANCE
PIN ACCELERATOR/LINEAR ACCELERATOR
BOOSTER ACCELERATOR
MAIN ENTRANCE
BATAVIA
KIRK RD
FERMILAB BOUNDARY
BUTTERFIELD RD
CHICAGO
FERMILAB
Access to: FERMILAB
Fermilab
Fermi National Accelerator Laboratory
BATAVIA, IL 60510

Figure 3

FERMI NATIONAL ACCELERATOR LABORATORY

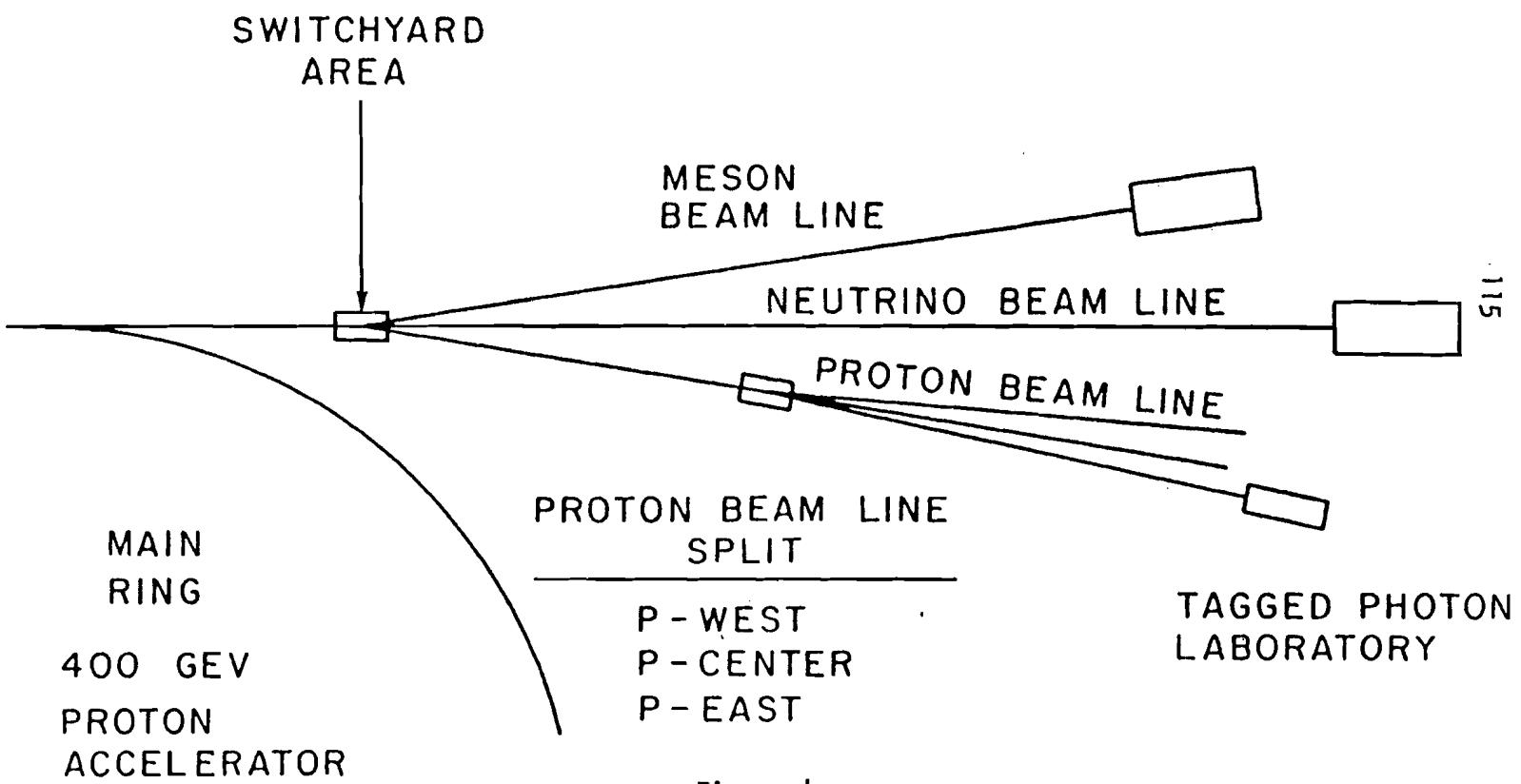

Figure 4

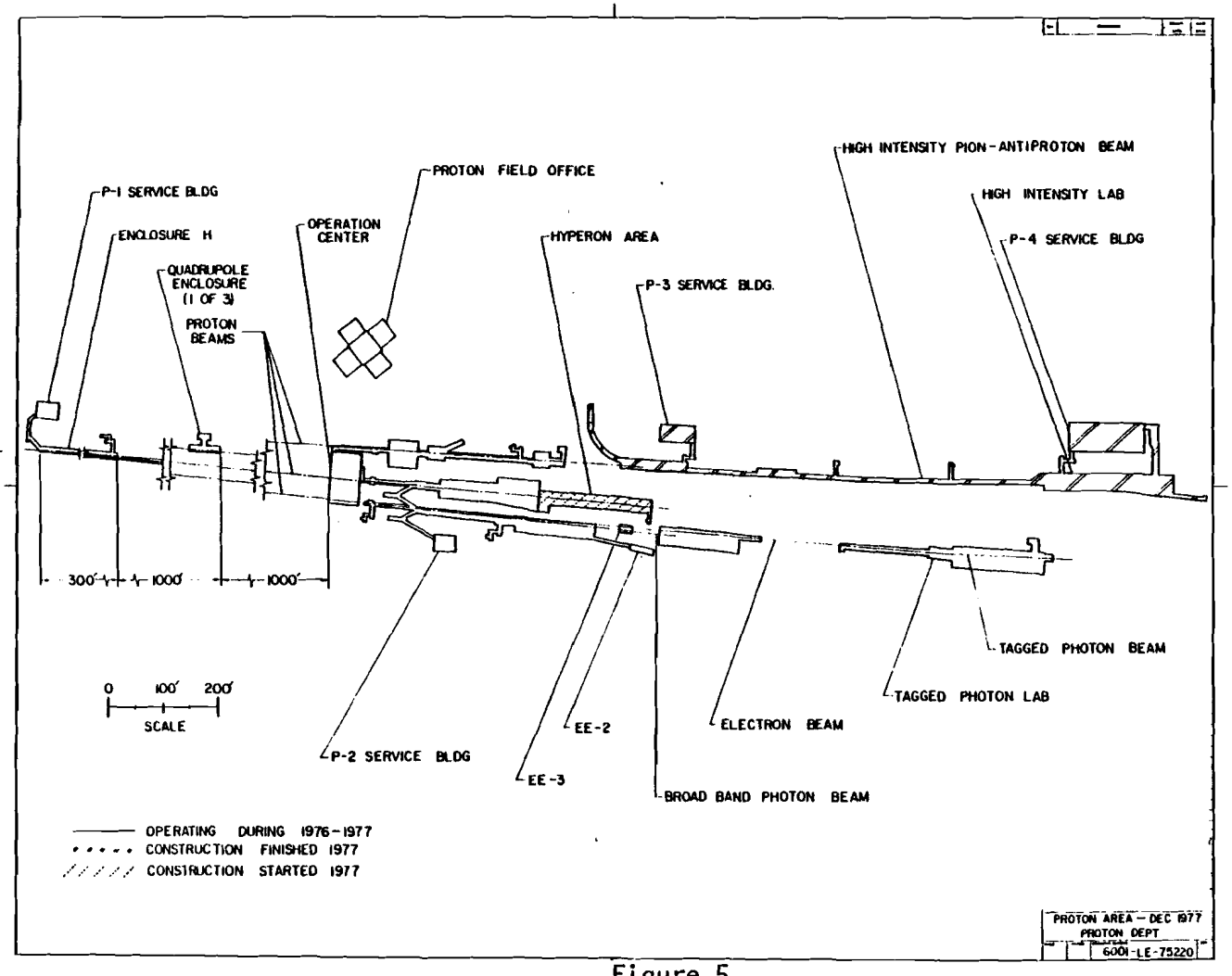
P-1 SERVICE BLDG
ENCLOSURE H
QUADRUPOLE ENCLOSURE (1 OF 3)
PROTON BEAMS
OPERATION CENTER
PROTON FIELD OFFICE
HYPERON AREA
P-3 SERVICE BLDG.
HIGH INTENSITY PION-ANTIPROTON BEAM
HIGH INTENSITY LAB
P-4 SERVICE BLDG
300'
1000'
1000'
0 100' 200'
SCALE
P-2 SERVICE BLDG
EE-3
EE-2
BROAD BAND PHOTON BEAM
ELECTRON BEAM
TAGGED PHOTON LAB
TAGGED PHOTON BEAM
OPERATING DURING 1976-1977
CONSTRUCTION FINISHED 1977
CONSTRUCTION STARTED 1977
PROTON AREA - DEC 1977
PROTON DEPT
6001-LE-75220

Figure 5

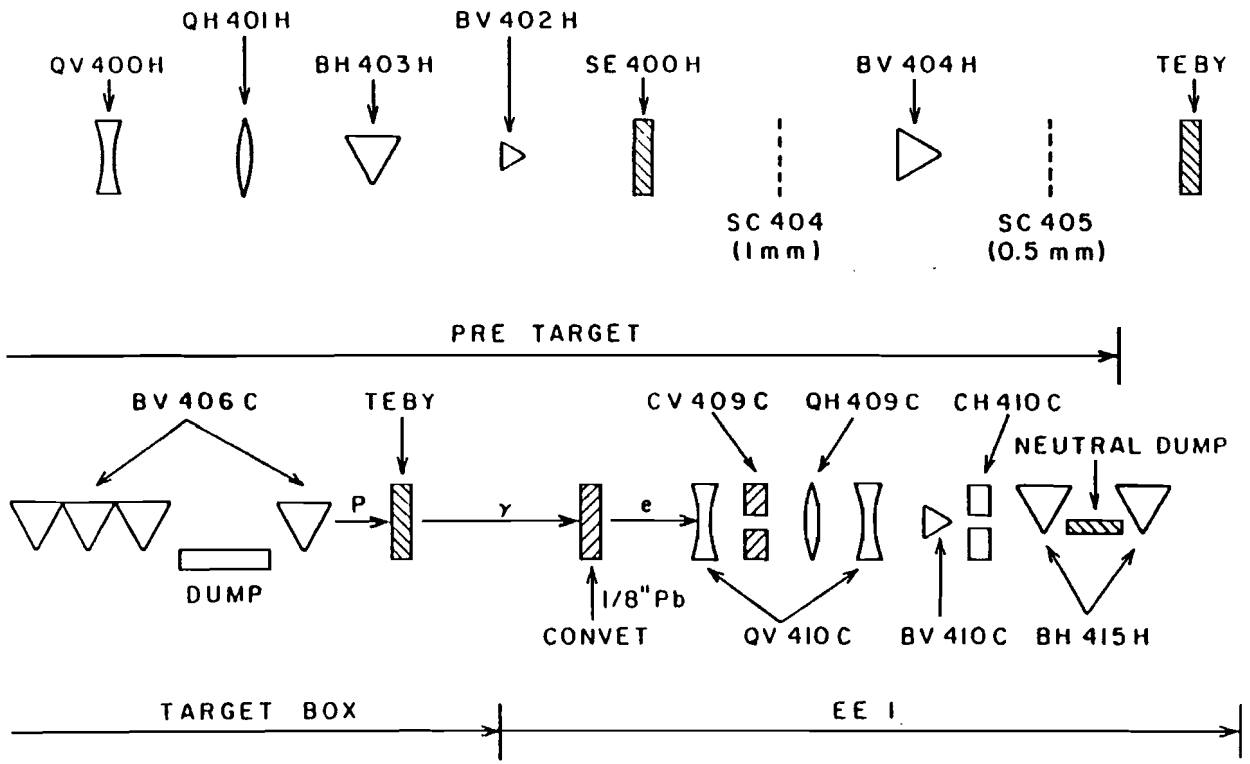
QV 400H
QH 401H
BH 403H
BV 402H
SE 400H
SC 404
(1mm)
BV 404H
SC 405
(0.5 mm)
TEBY
PRE TARGET
BV 406C
DUMP
TEBY
P
γ
e
1/8"Pb
CONVET
CV 409C
QH 409C
QV 410C
CH 410C
BV 410C
NEUTRAL DUMP
BH 415H
TARGET BOX
EE I

Figure 6

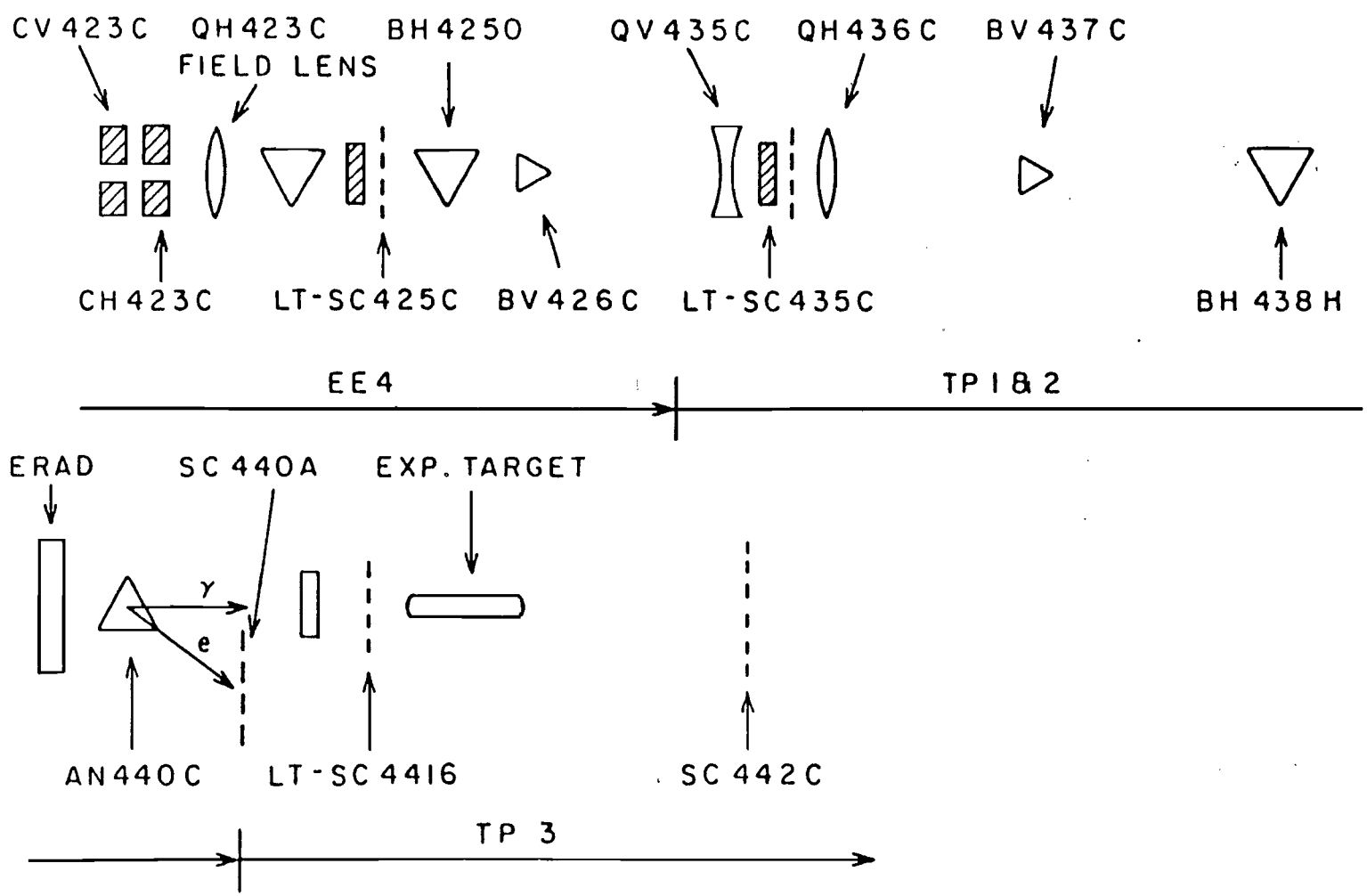
CV423C
QH423C
FIELD LENS
BH425O
QV435C
QH436C
BV437C
CH423C
LT-SC425C
BV426C
LT-SC435C
BH 438H
EE4
TP 1 & 2
ERAD
SC 440A
EXP. TARGET
γ
e
AN440C
LT-SC 441B
SC 442C
TP 3

Figure 7

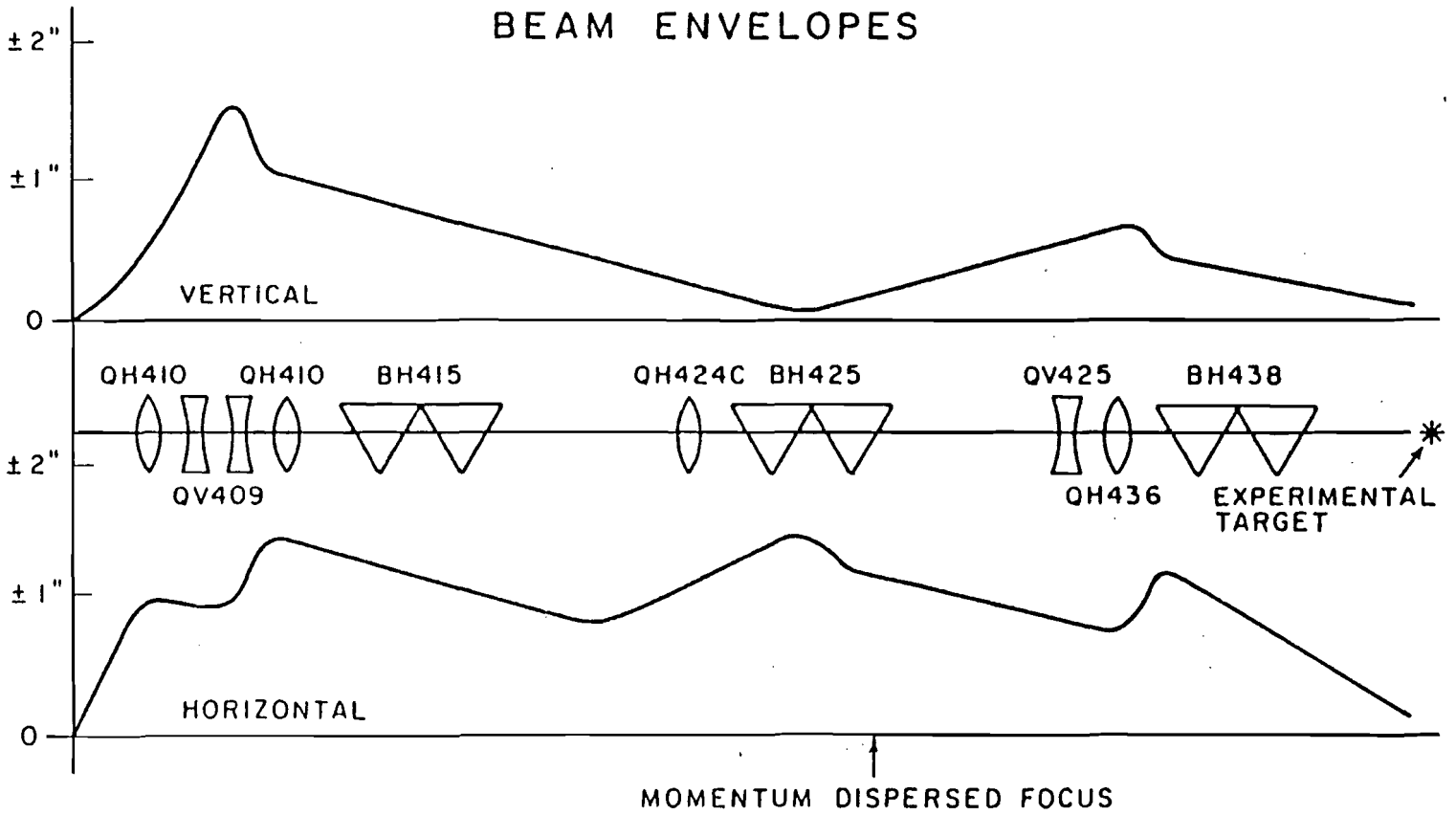
BEAM ENVELOPES
±2"
±1"
0
VERTICAL
QH410
QH410
BH415
QH424C
BH425
QV425
BH438
±2"
QV409
QH436
EXPERIMENTAL TARGET
±1"
HORIZONTAL
0
MOMENTUM DISPERSED FOCUS

Figure 8

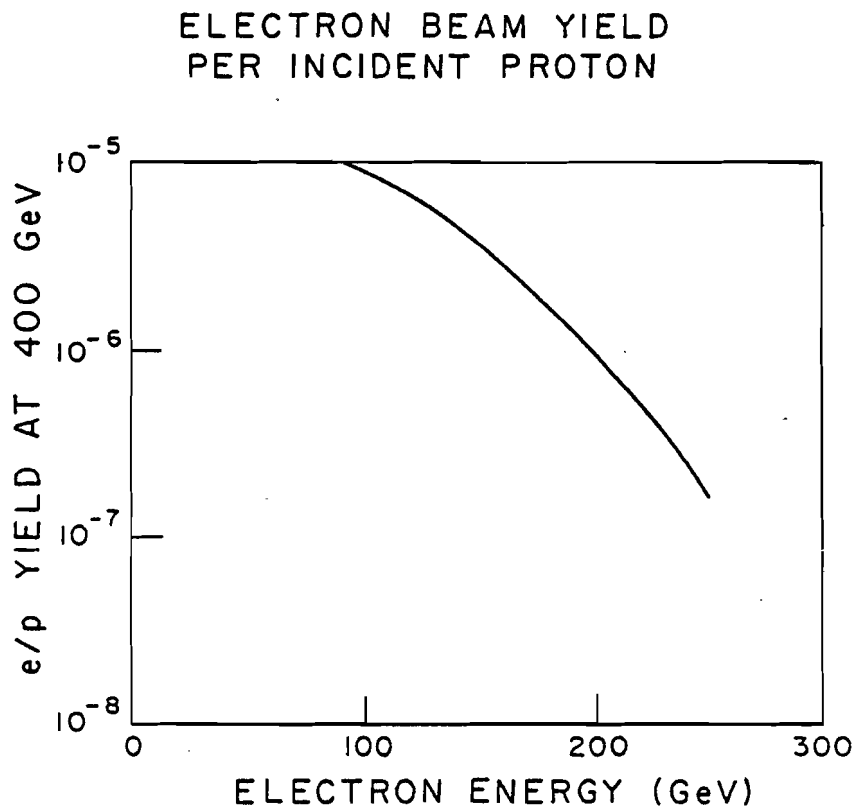
ELECTRON BEAM YIELD
PER INCIDENT PROTON
e/p YIELD AT 400 GeV
10^-5
10^-6
10^-7
10^-8
0
100
200
300
ELECTRON ENERGY (GeV)

Figure 9

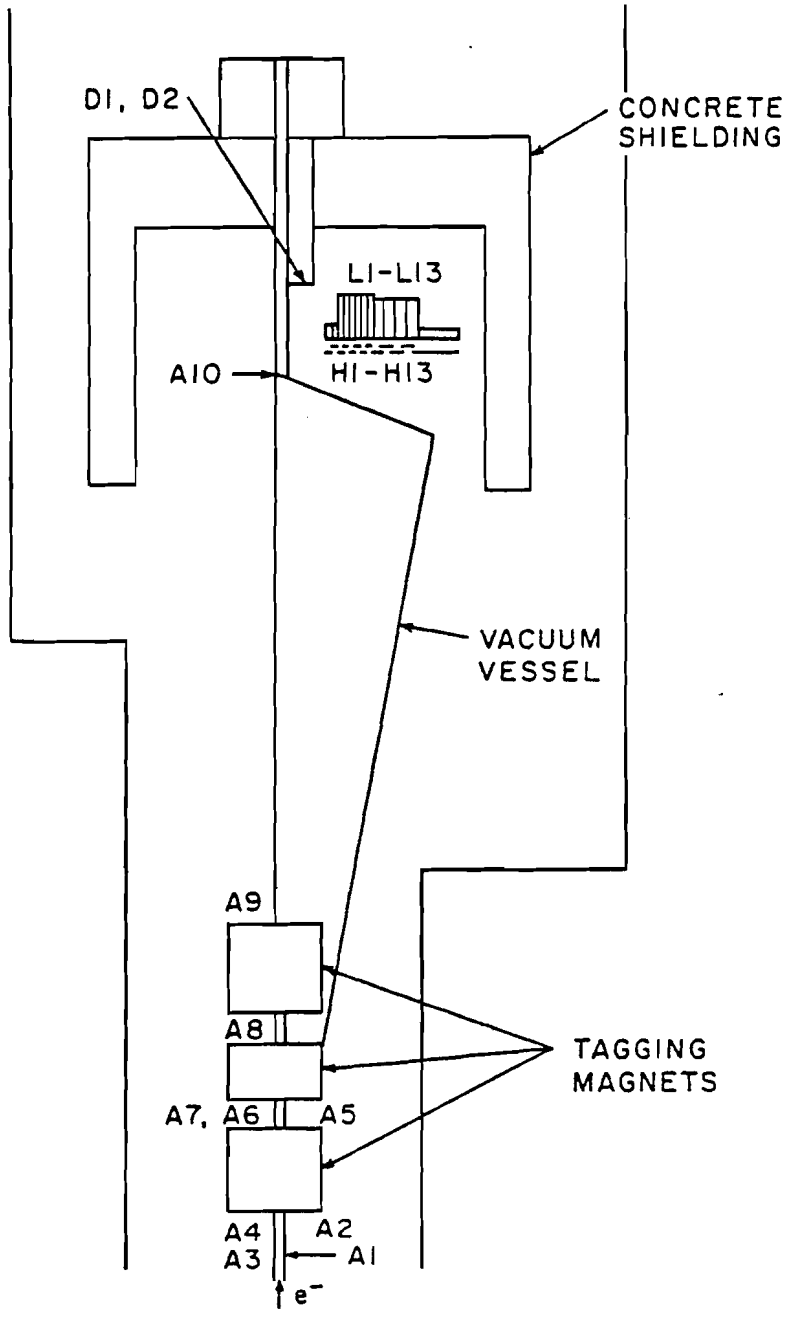
D1, D2
CONCRETE SHIELDING
L1-L13
H1-H13
A10
VACUUM VESSEL
A9
A8
A7, A6
A5
TAGGING MAGNETS
A4
A3
A2
A1
e⁻

Figure 10

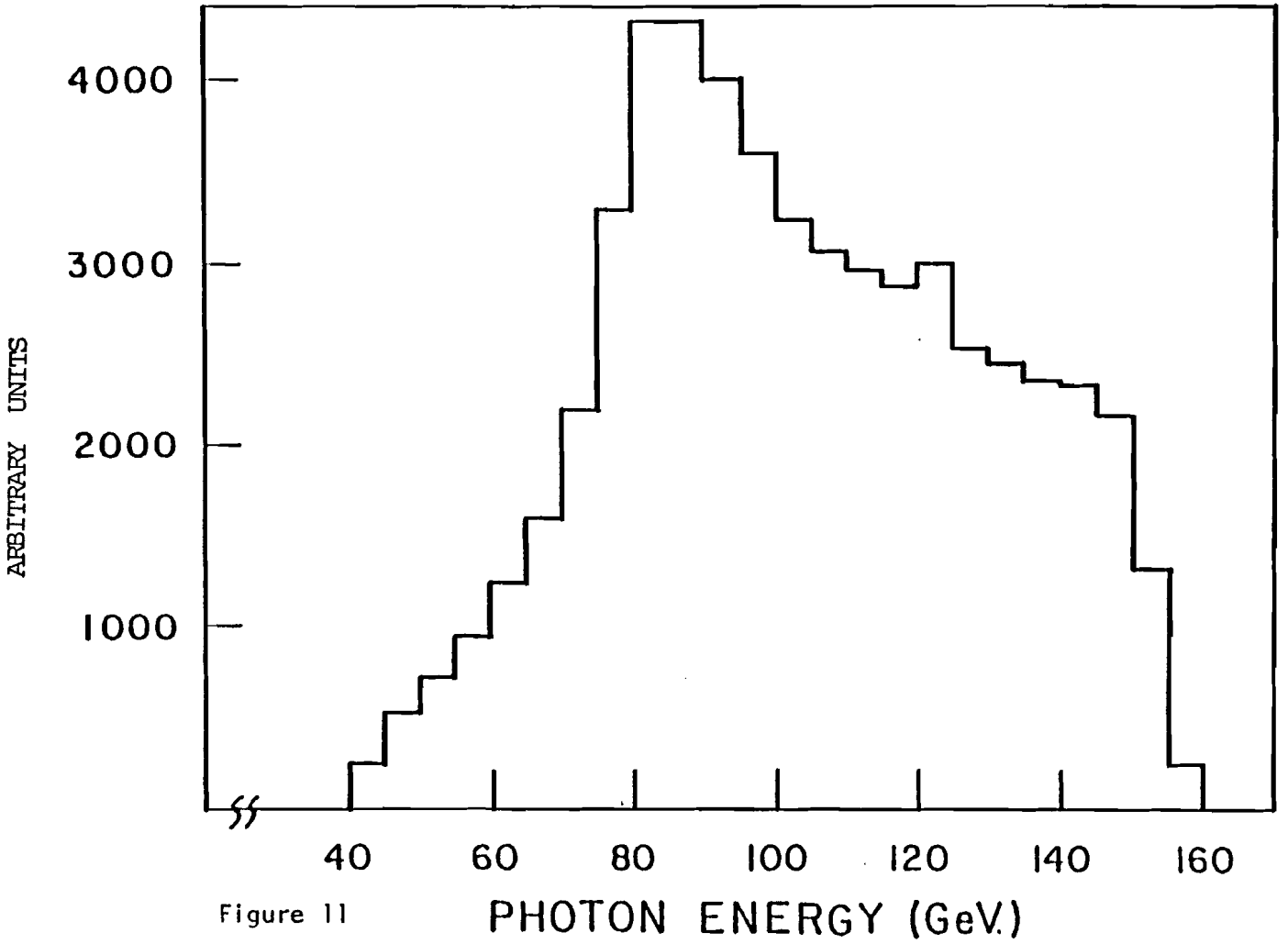
4000
3000
2000
1000
ARBITRARY UNITS
40
60
80
100
120
140
160
PHOTON ENERGY (GeV.)

Figure 11

DRIFT CHAMBER SYSTEM (TOP VIEW)
(TOTAL OF 29 PLANES)

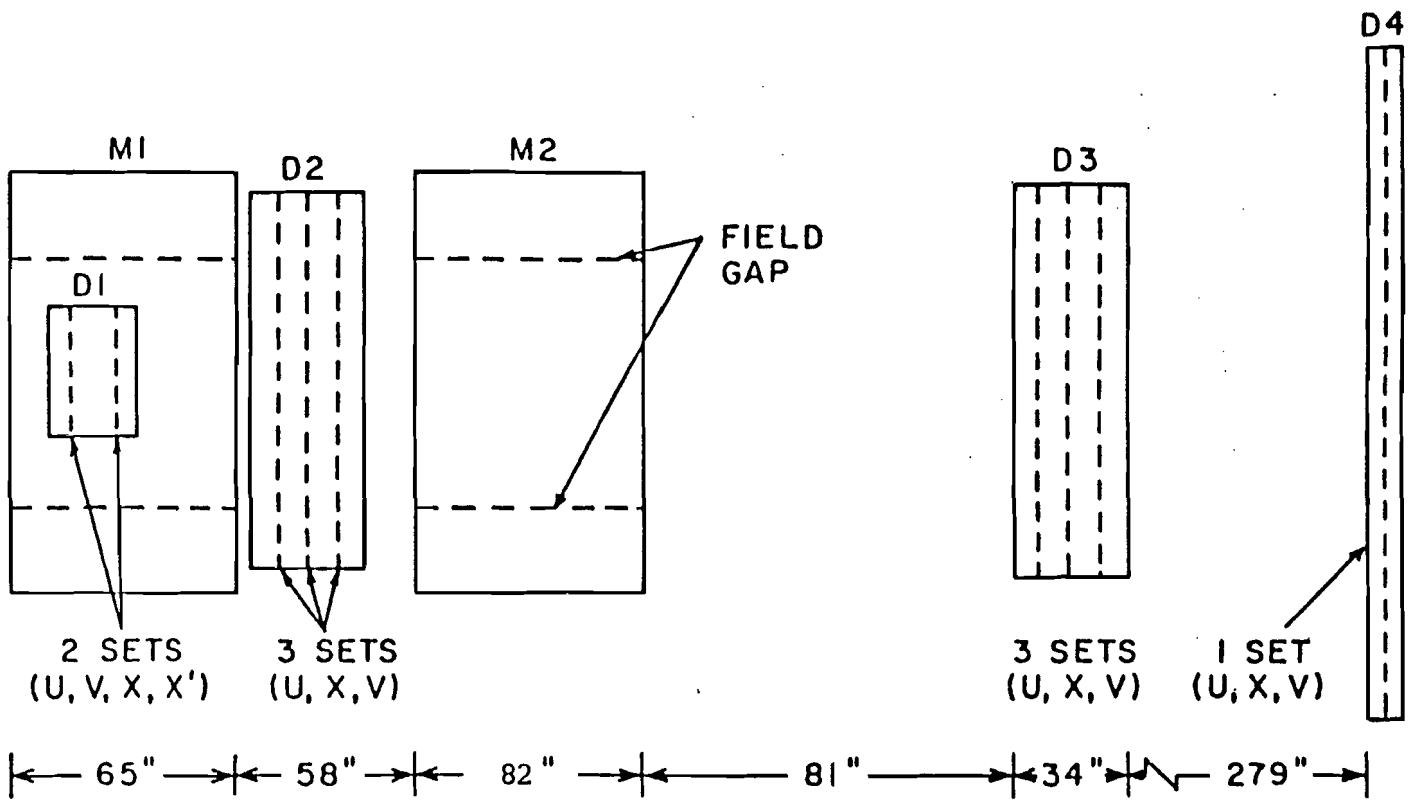

Figure 12

D1 ASSEMBLY

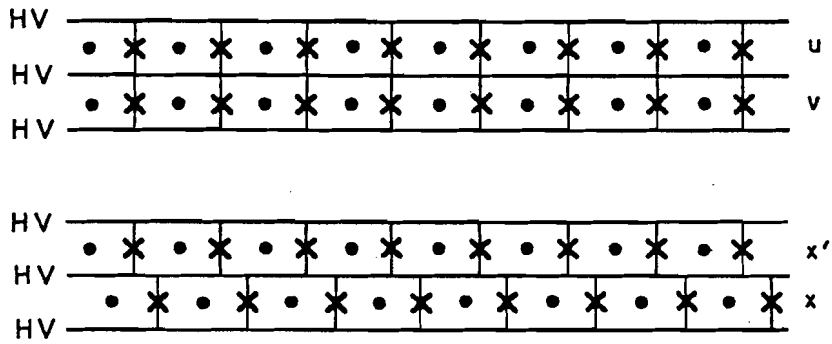

× - FIELD WIRES

• - SENSE WIRES

HV - HIGH VOLTAGE FIELD PLANES

D2-D4 ASSEMBLIES

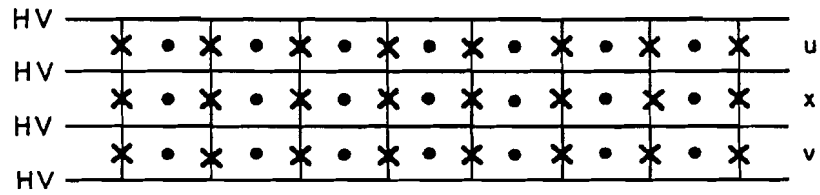

DRIFT CHAMBER CELL STRUCTURE

Figure 13

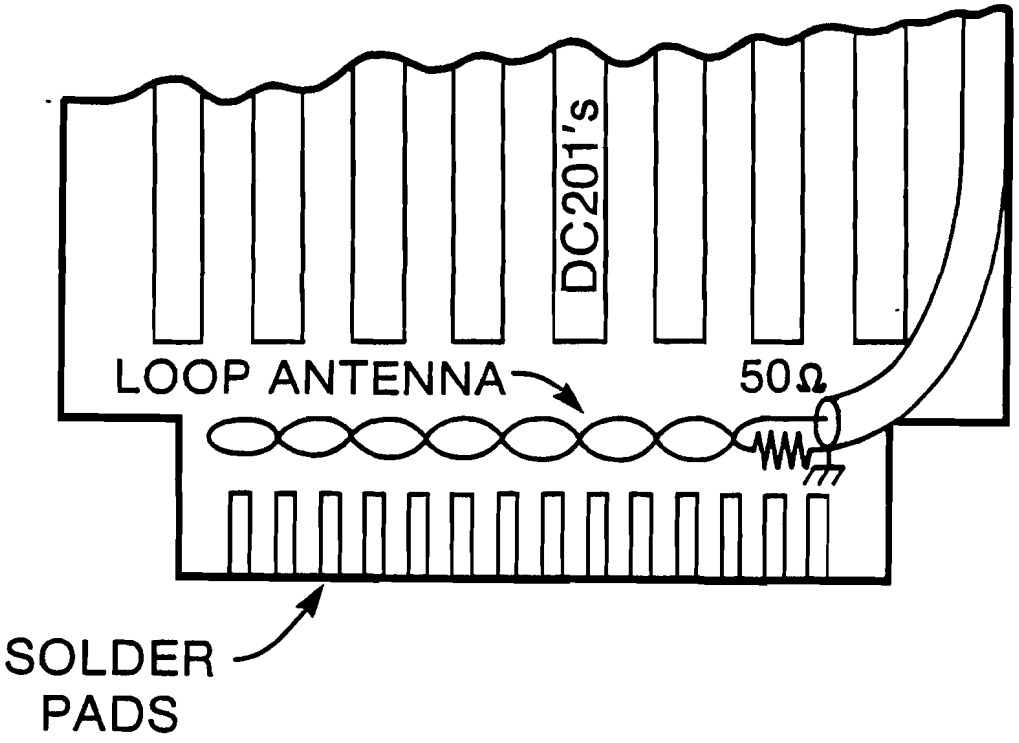

Figure 14

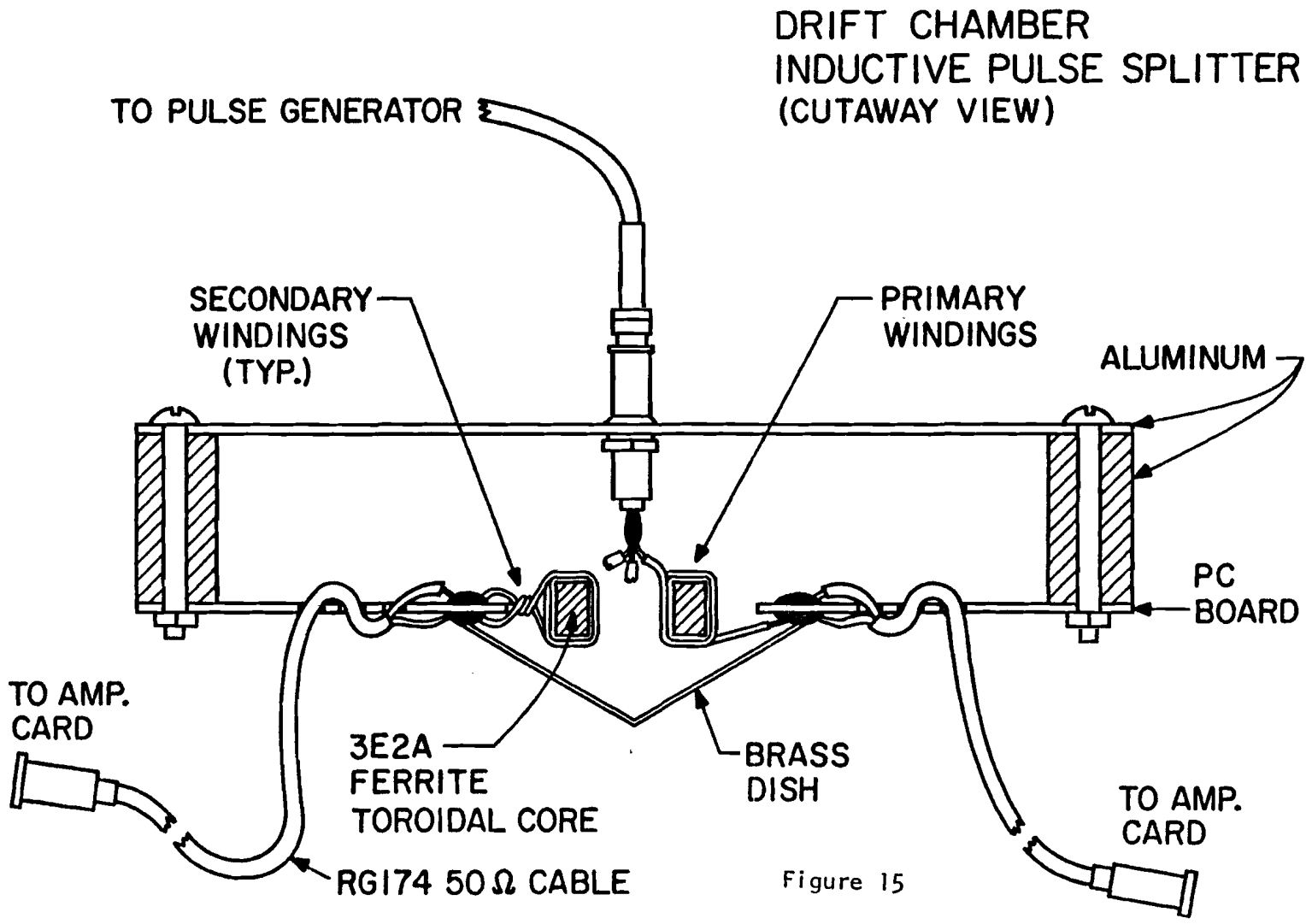
DRIFT CHAMBER
INDUCTIVE PULSE SPLITTER
(CUTAWAY VIEW)
TO PULSE GENERATOR
SECONDARY WINDINGS (TYP.)
PRIMARY WINDINGS
ALUMINUM
PC BOARD
TO AMP. CARD
3E2A FERRITE TOROIDAL CORE
BRASS DISH
TO AMP. CARD
RG174 50Ω CABLE

Figure 15

Figure 16

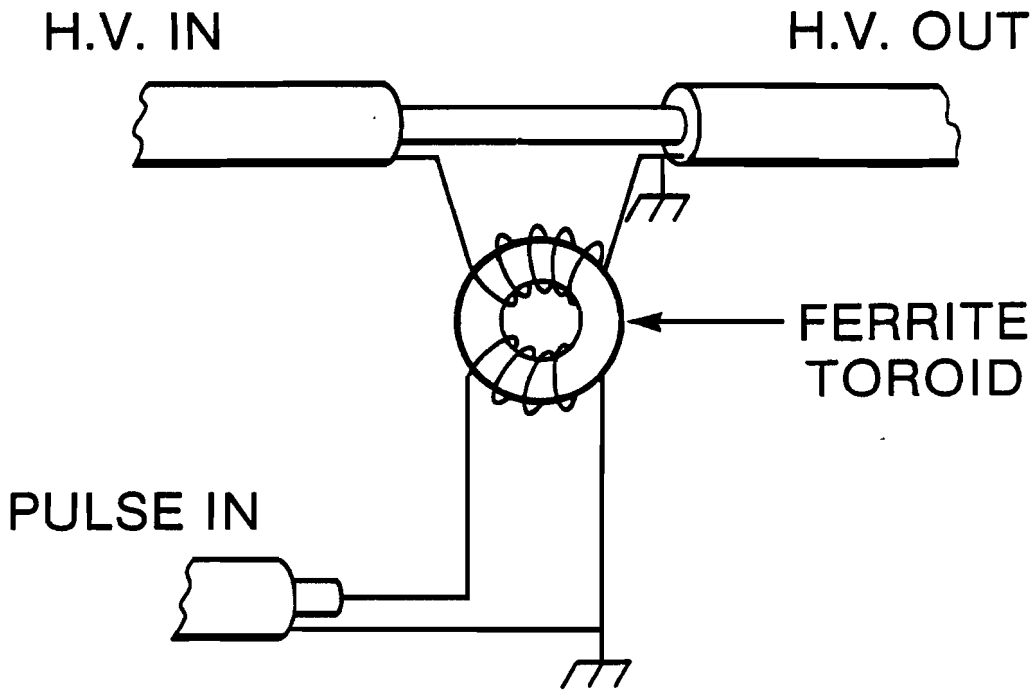

INDUCTIVE/CAPACITIVE COUPLER

Figure 17

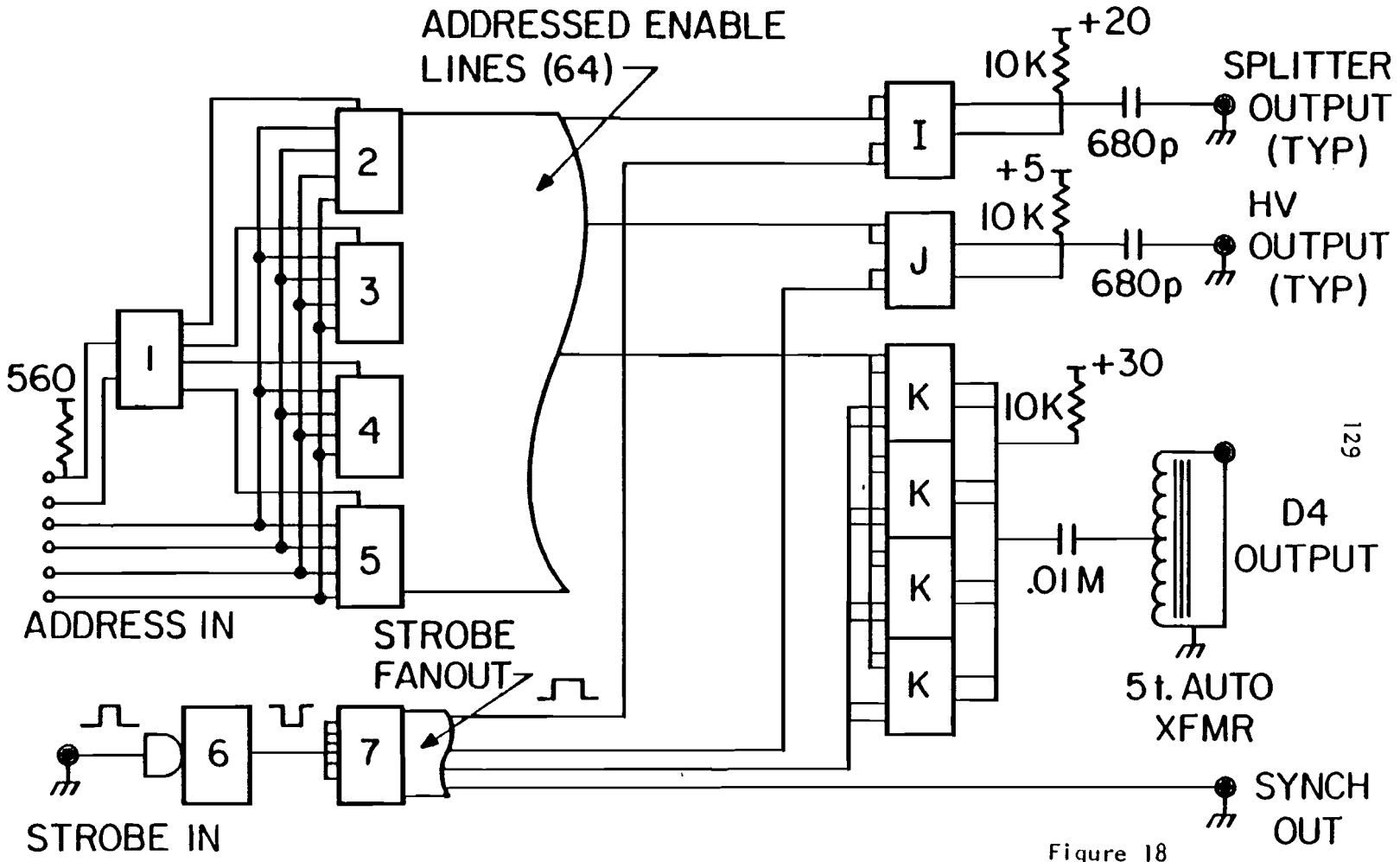

Figure 18

DRIFT CHAMBER TEST PULSER

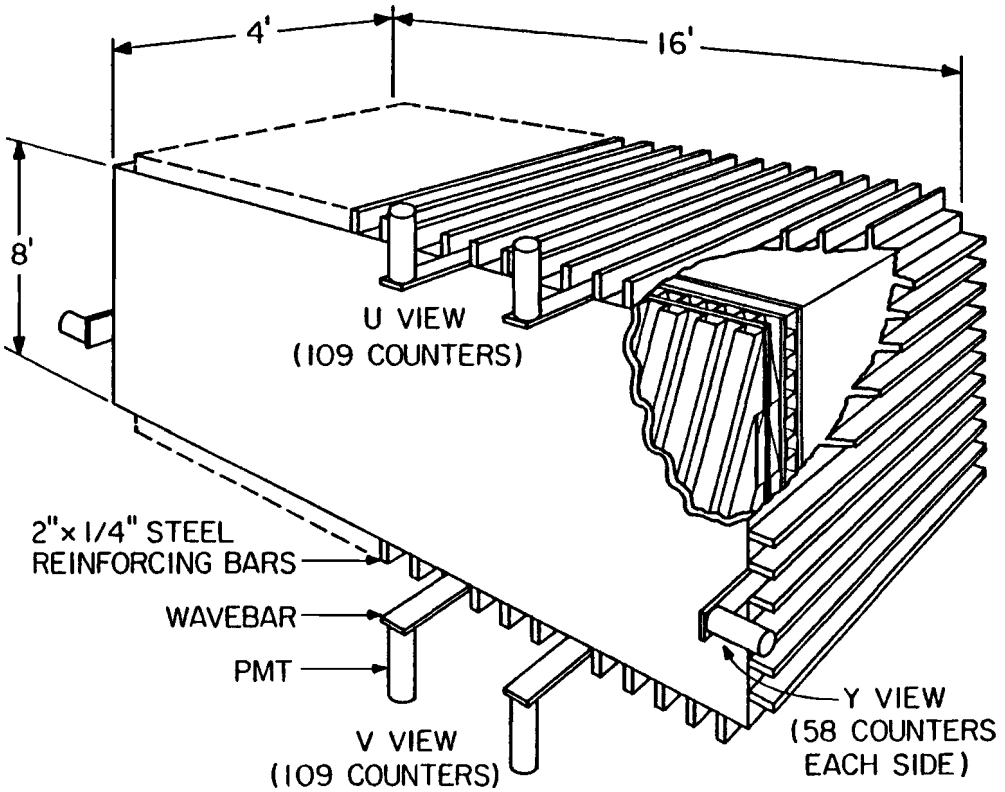

LEAD/LIQUID SCINTILLATOR SHOWER COUNTER (SLIC)
(SCHEMATIC)

Figure 19

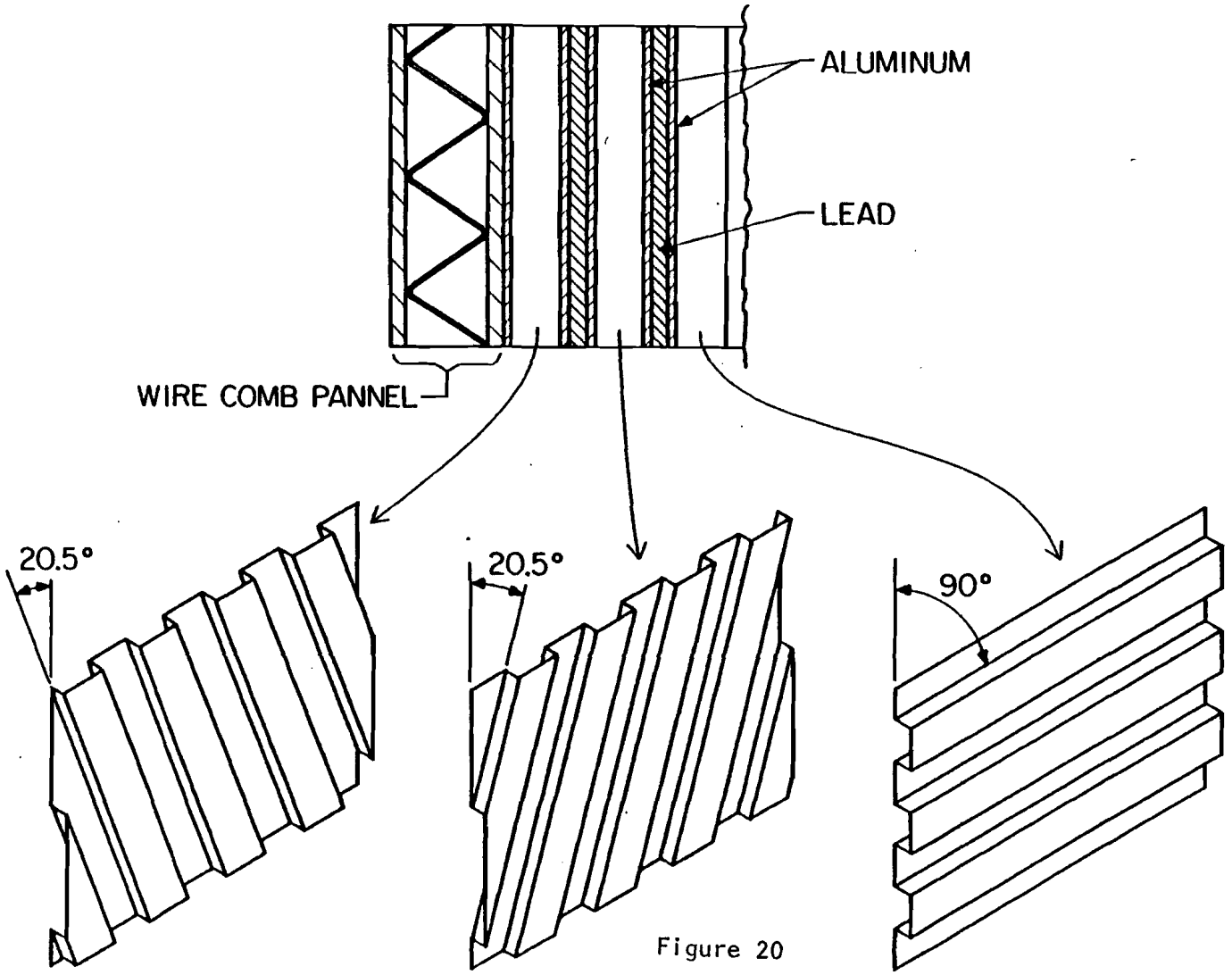

Figure 20

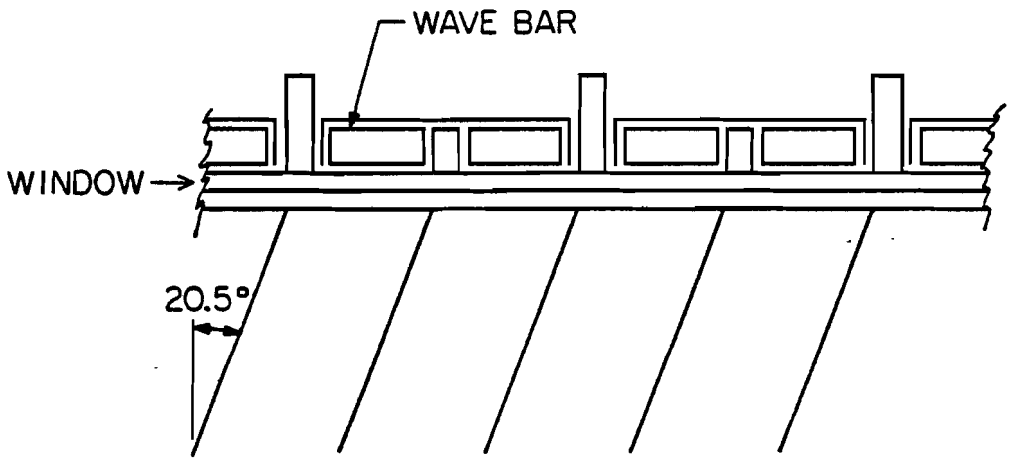

Figure 21

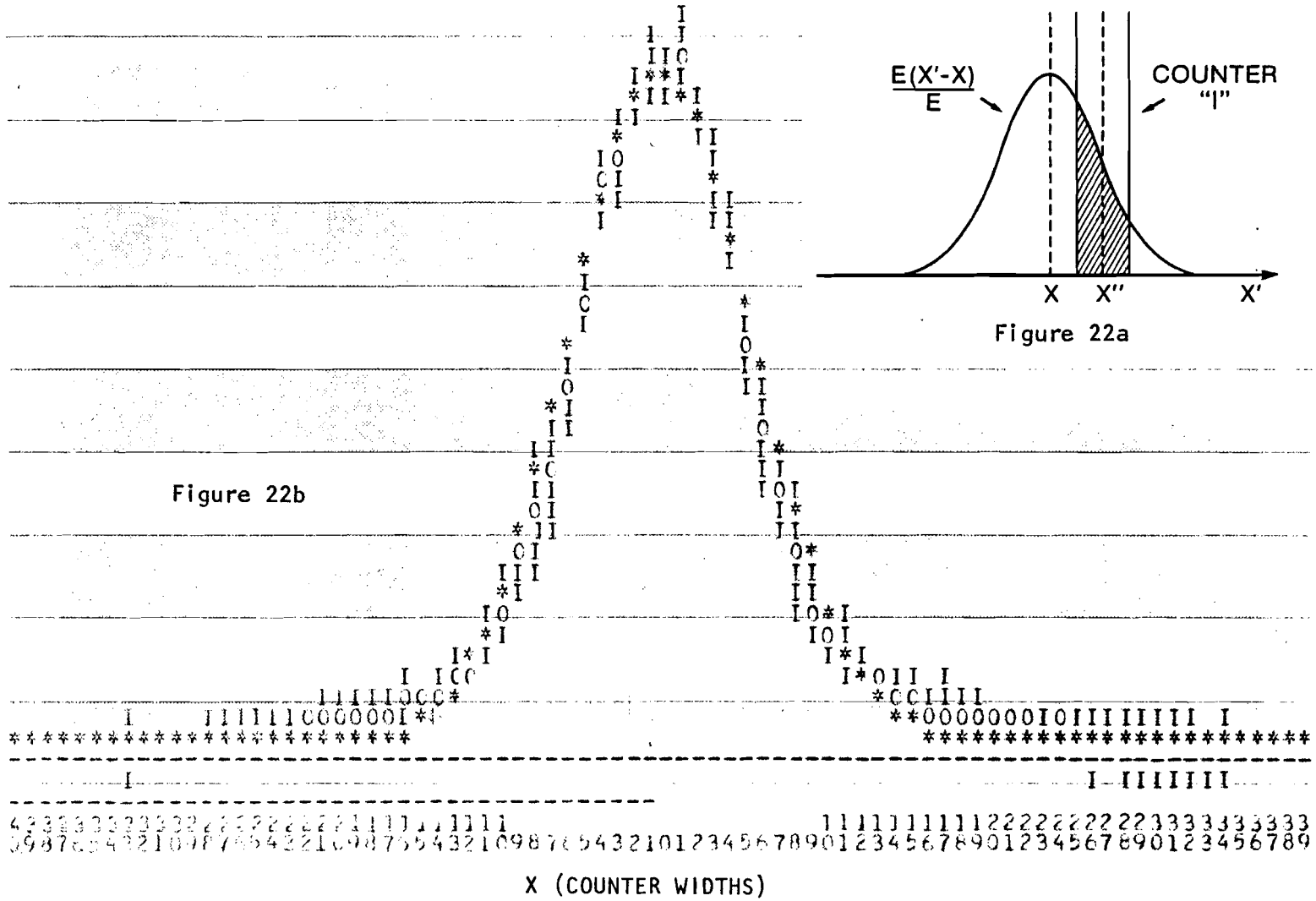

Figure 22b

Figure 22a

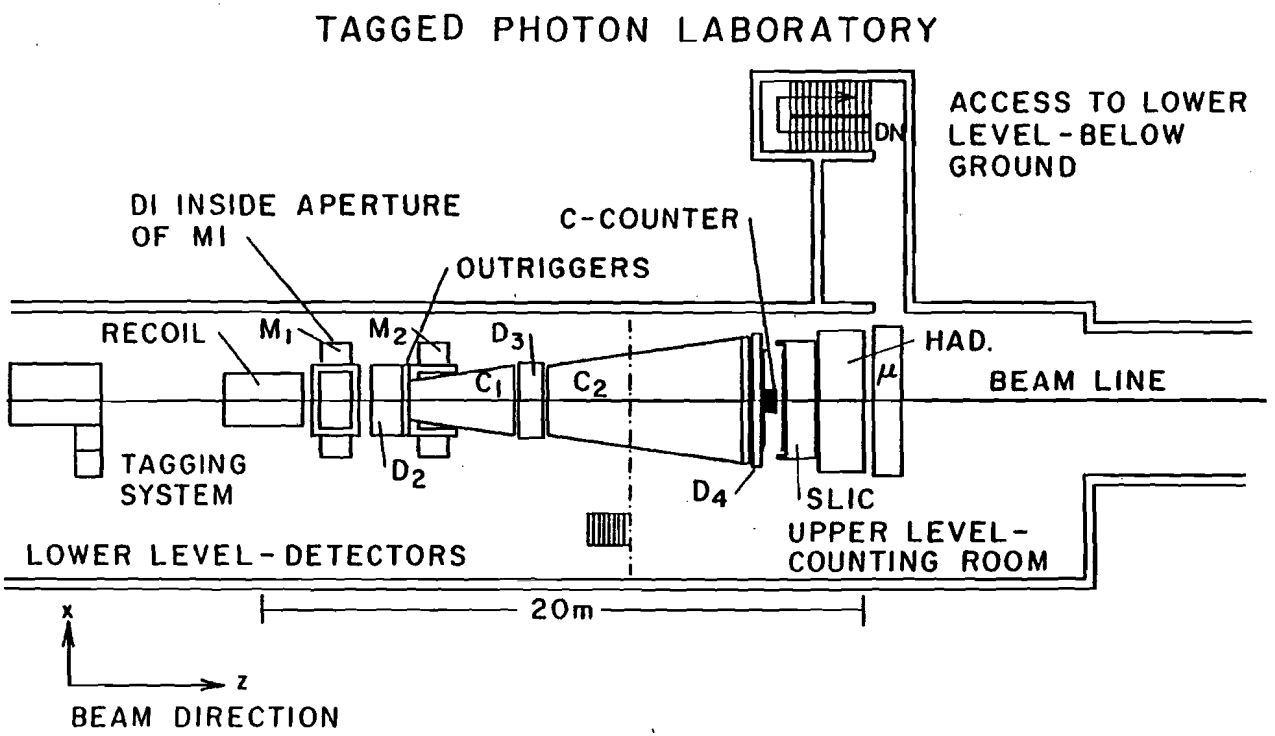
TAGGED PHOTON LABORATORY
ACCESS TO LOWER LEVEL - BELOW GROUND
DN
DI INSIDE APERTURE OF MI
C-COUNTER
OUTRIGGERS
RECOIL
M1
M2
D3
C1
C2
HAD.
μ
BEAM LINE
TAGGING SYSTEM
D2
D4
SLIC
UPPER LEVEL - COUNTING ROOM
LOWER LEVEL - DETECTORS
20m
x
z
BEAM DIRECTION

Figure 23

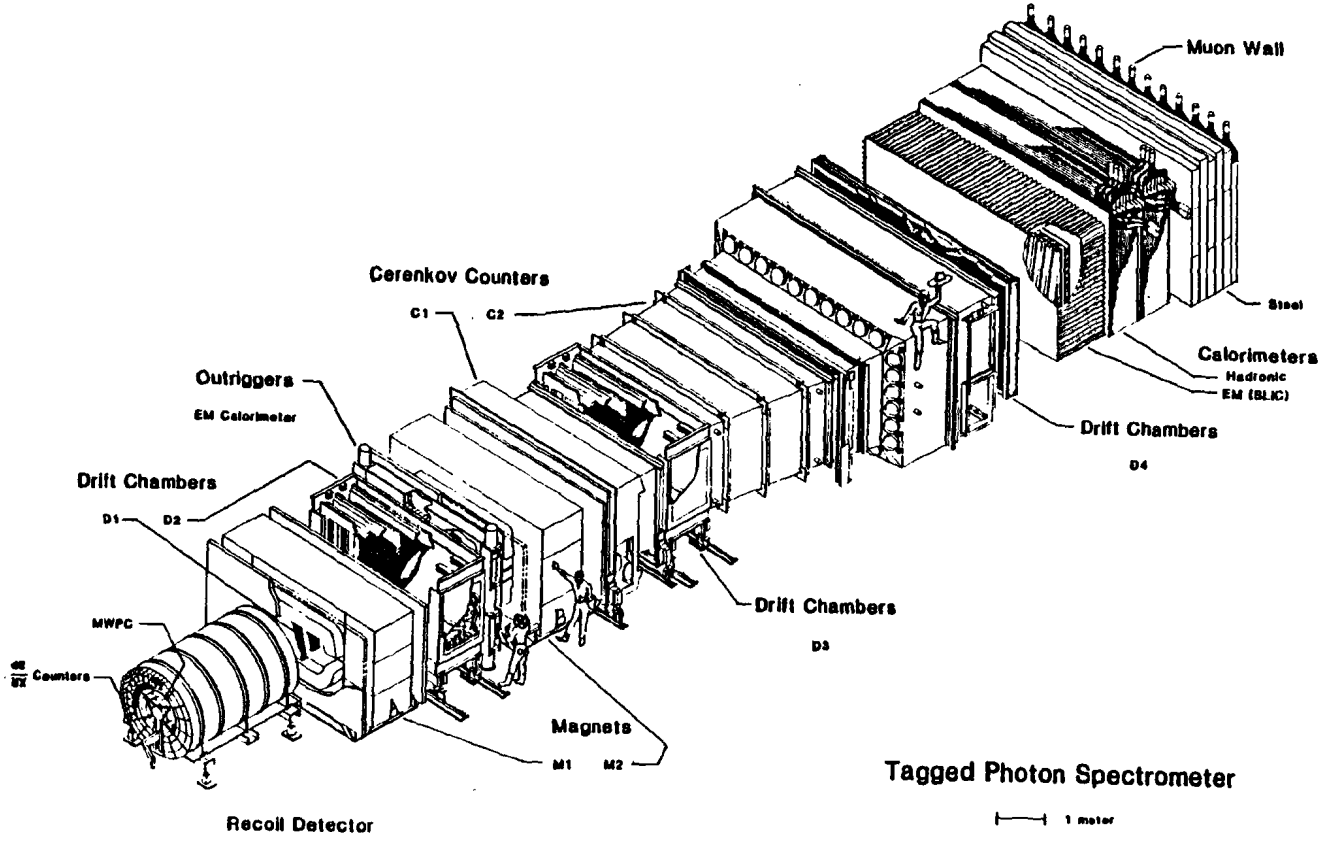
Muon Wall
Steel
Calorimeters
Hadronic
EM (SLIC)
Drift Chambers
D4
Cerenkov Counters
C1
C2
Outriggers
EM Calorimeter
Drift Chambers
D1
D2
MWPC
Counters
Drift Chambers
D3
Magnets
M1
M2
Tagged Photon Spectrometer
1 meter
Recoil Detector

Figure 24

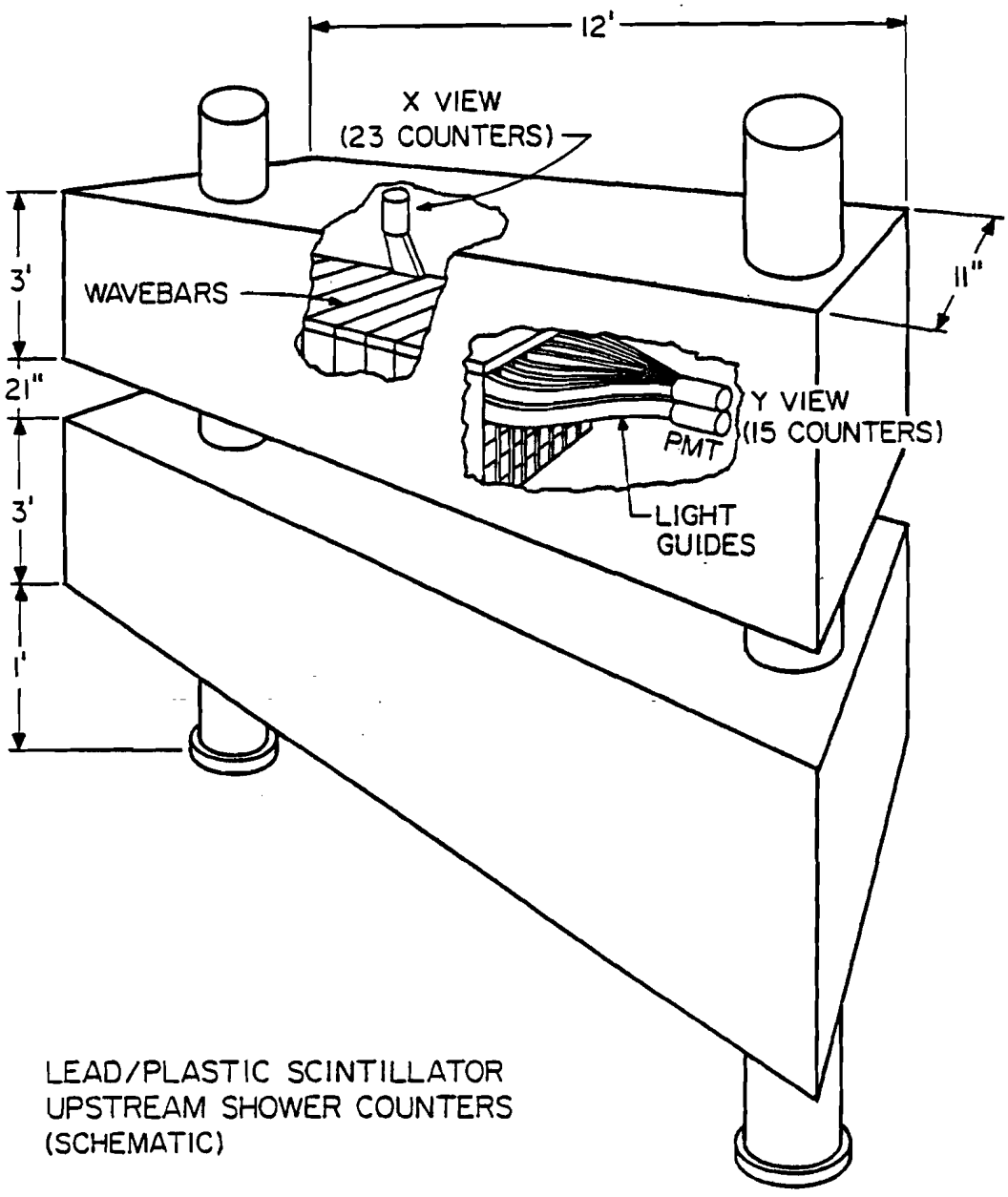

LEAD/PLASTIC SCINTILLATOR
UPSTREAM SHOWER COUNTERS
(SCHEMATIC)

Figure 25

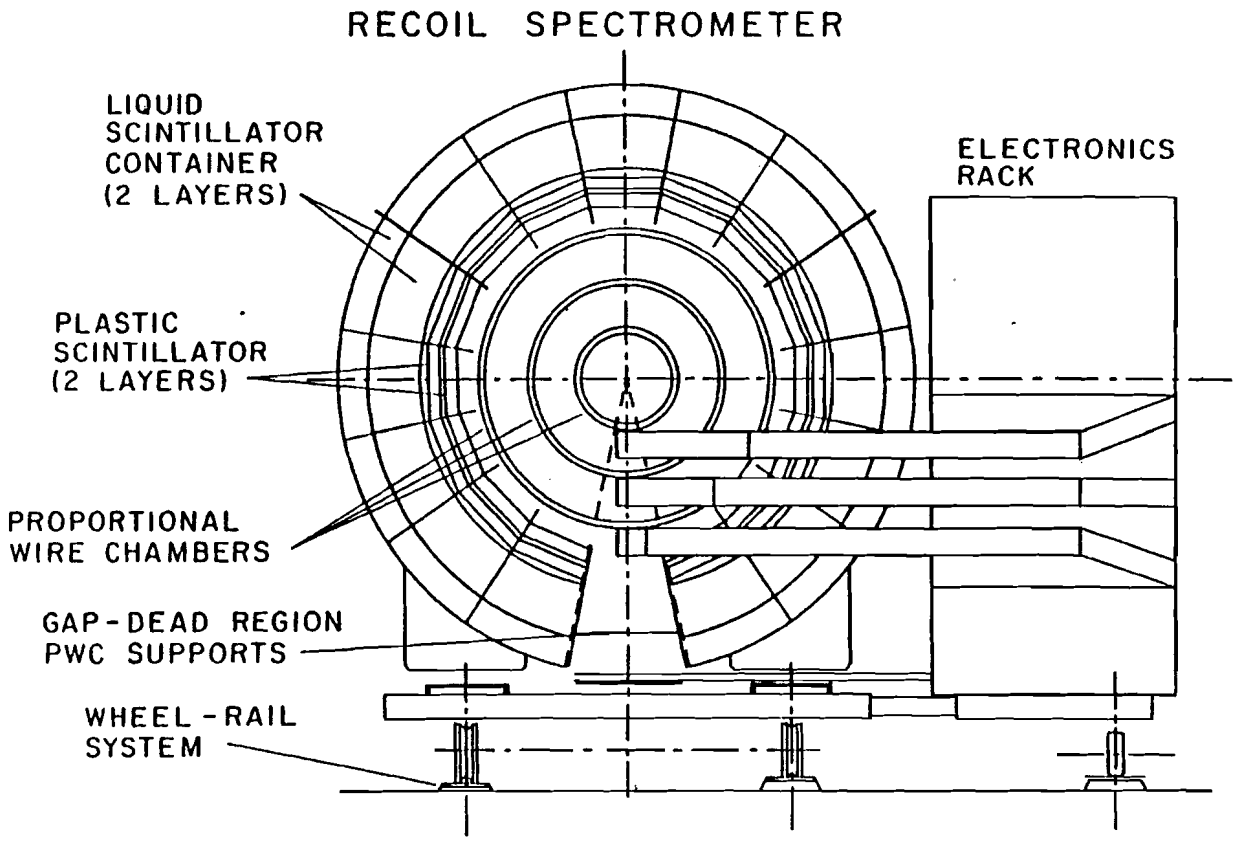
RECOIL SPECTROMETER
LIQUID SCINTILLATOR CONTAINER (2 LAYERS)
PLASTIC SCINTILLATOR (2 LAYERS)
PROPORTIONAL WIRE CHAMBERS
GAP-DEAD REGION PWC SUPPORTS
WHEEL-RAIL SYSTEM
ELECTRONICS RACK

Figure 26

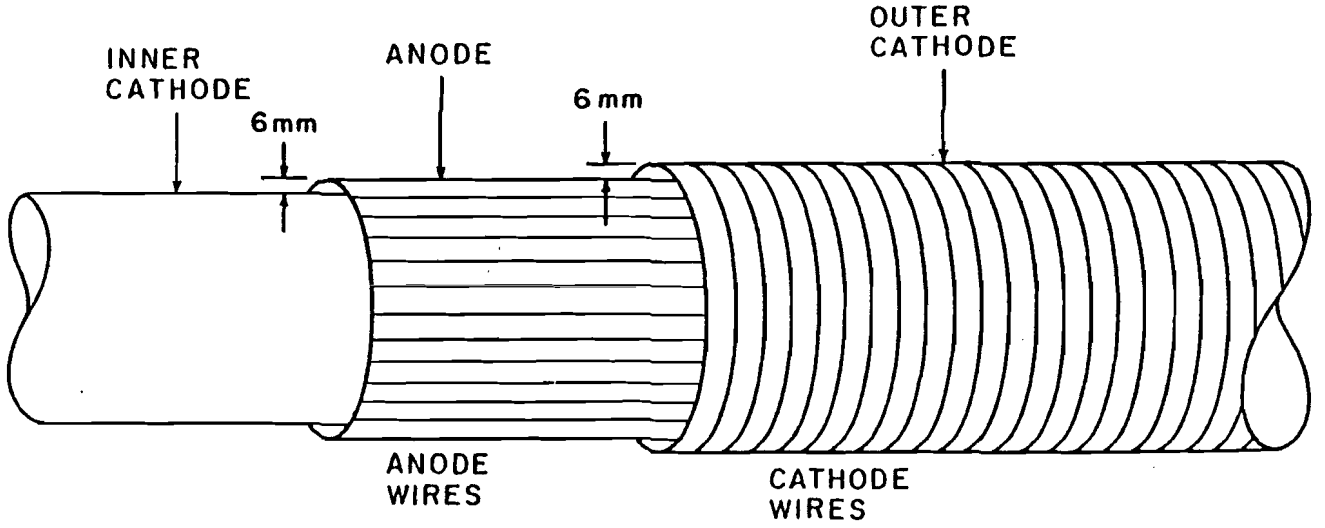

CUTAWAY VIEW OF PWC CHAMBER

Figure 27

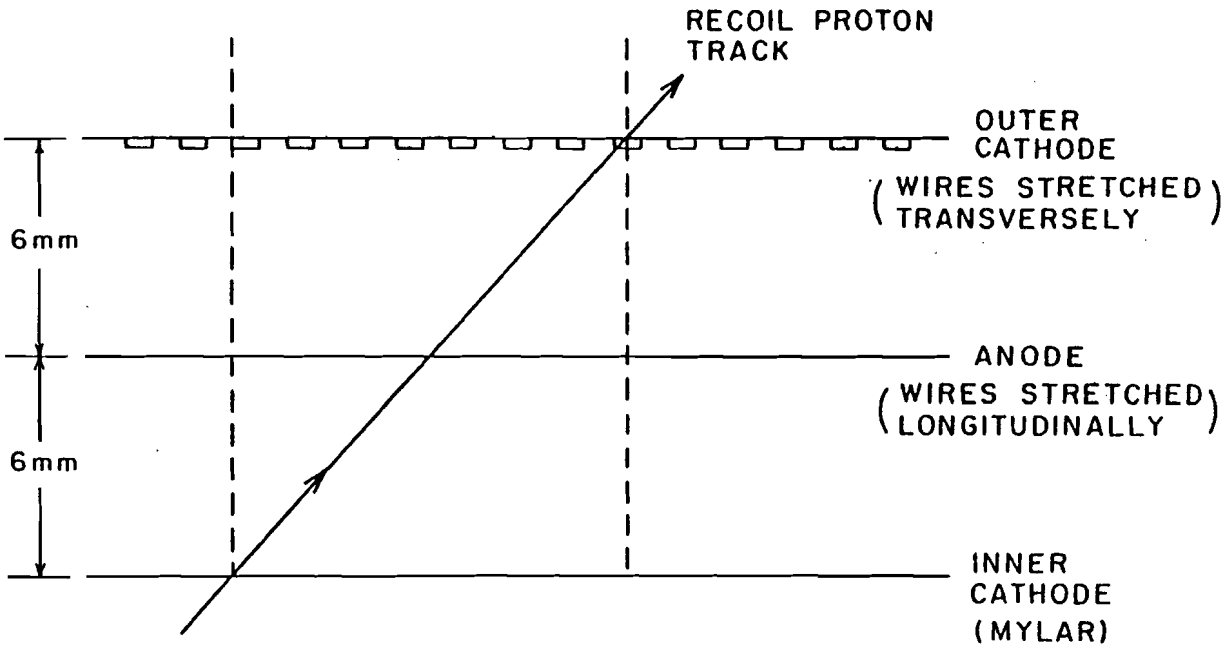

PWC CHAMBER
LONGITUDINAL CROSS SECTION

Figure 28

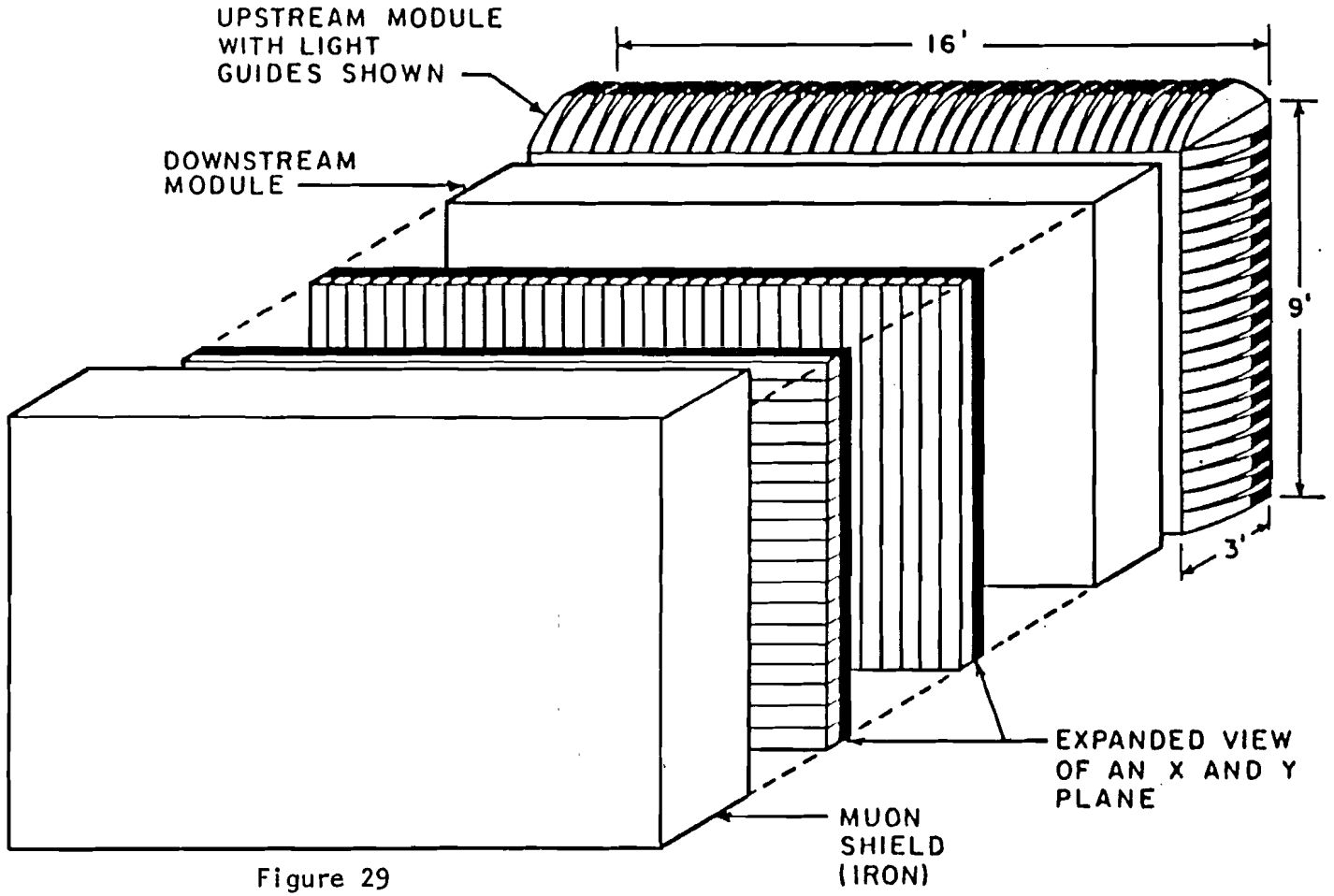
UPSTREAM MODULE
WITH LIGHT
GUIDES SHOWN
DOWNSTREAM
MODULE
16'
9'
3'
EXPANDED VIEW
OF AN X AND Y
PLANE
MUON
SHIELD
(IRON)

Figure 29

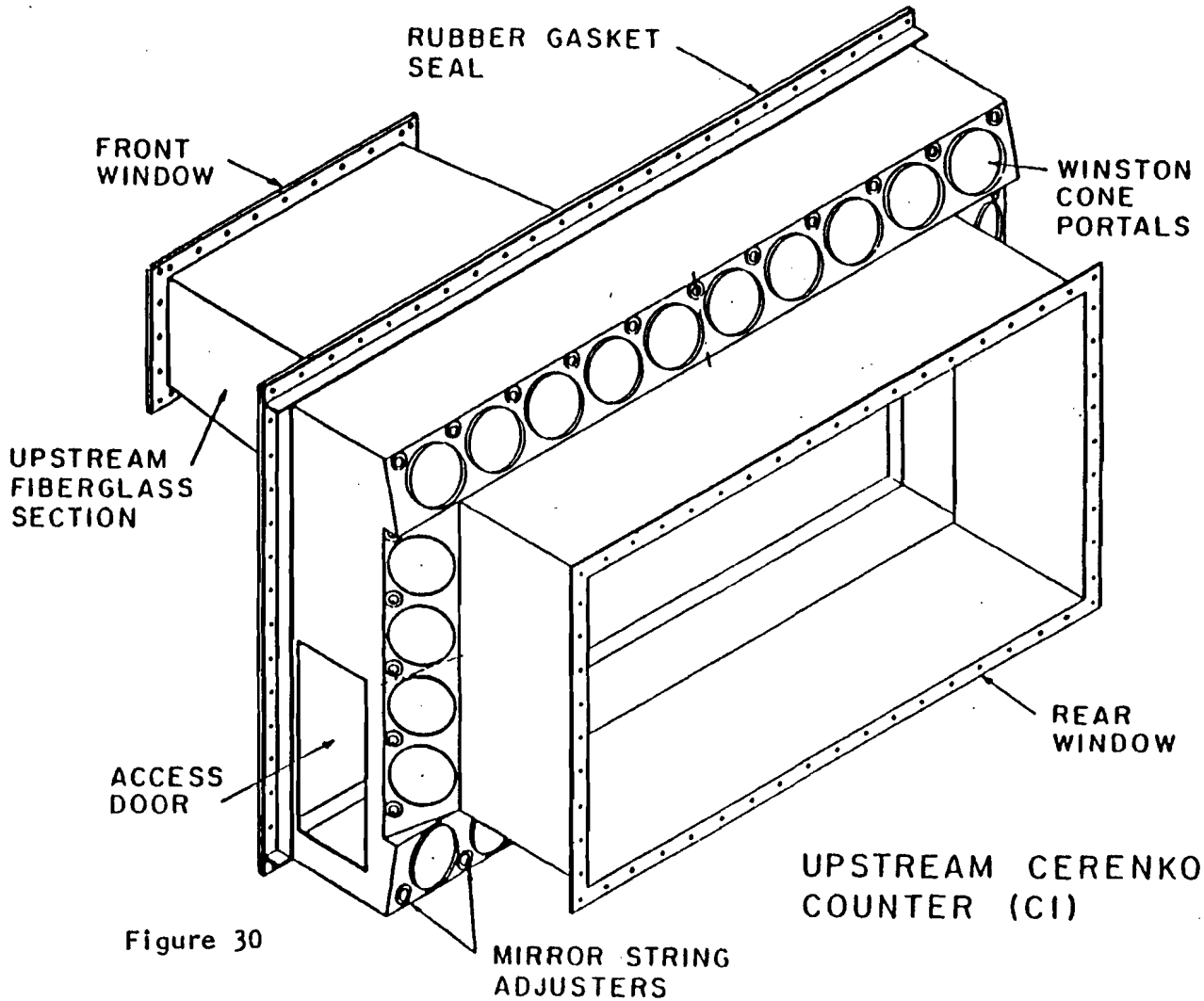

UPSTREAM CERENKOV COUNTER (CI)

Figure 30

DOWNSTREAM CERENKOV COUNTER (C2)

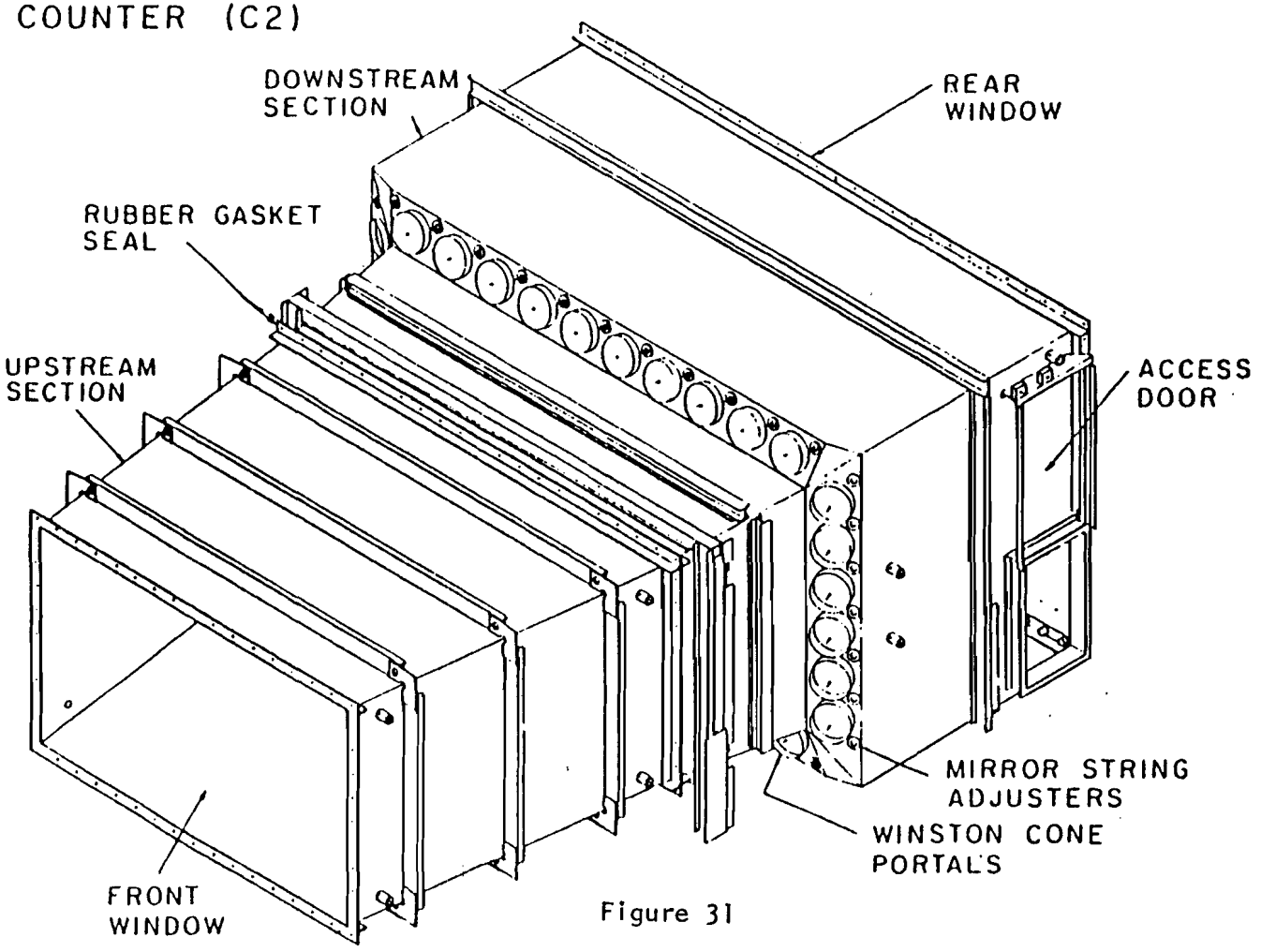

Figure 31

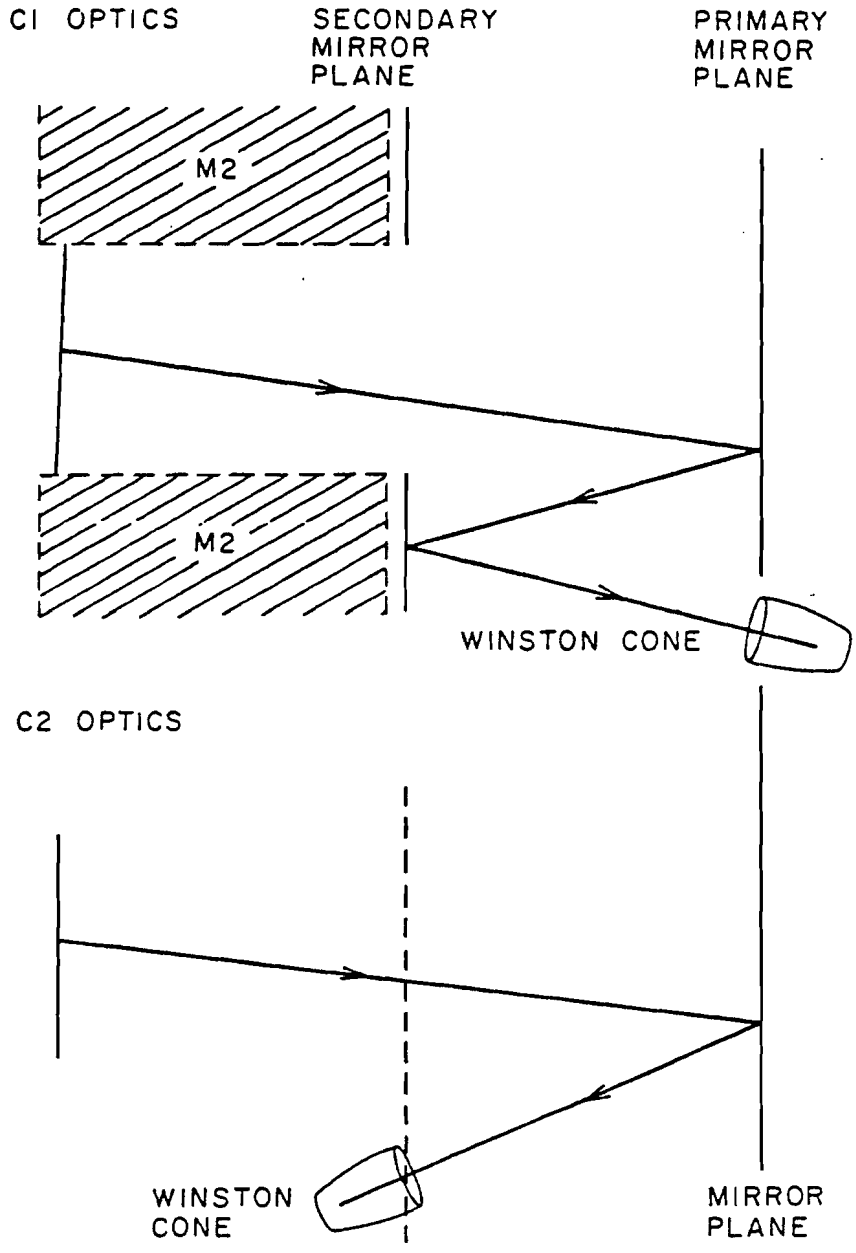
C1 OPTICS
SECONDARY MIRROR PLANE
PRIMARY MIRROR PLANE
M2
M2
WINSTON CONE
C2 OPTICS
WINSTON CONE
MIRROR PLANE

Figure 32

CERENKOV MIRROR SEGMENTATION

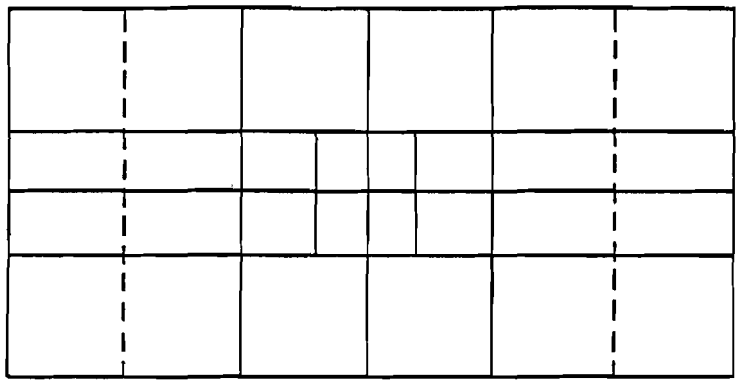

CERENKOV MIRROR SUSPENSION

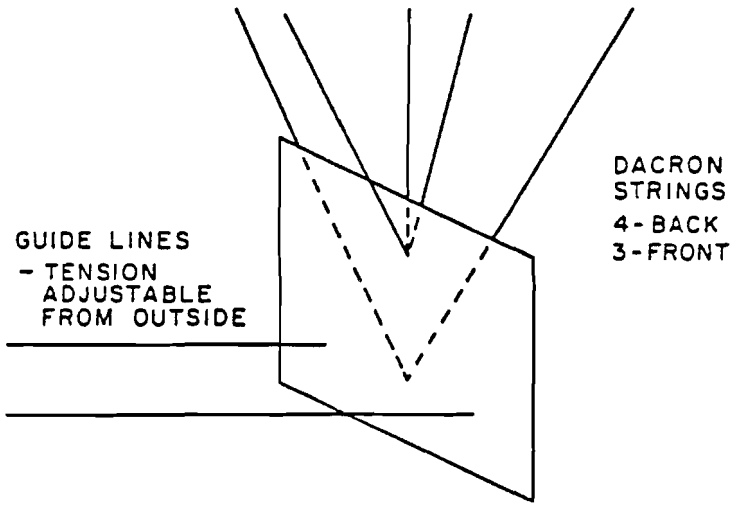

Figure 33

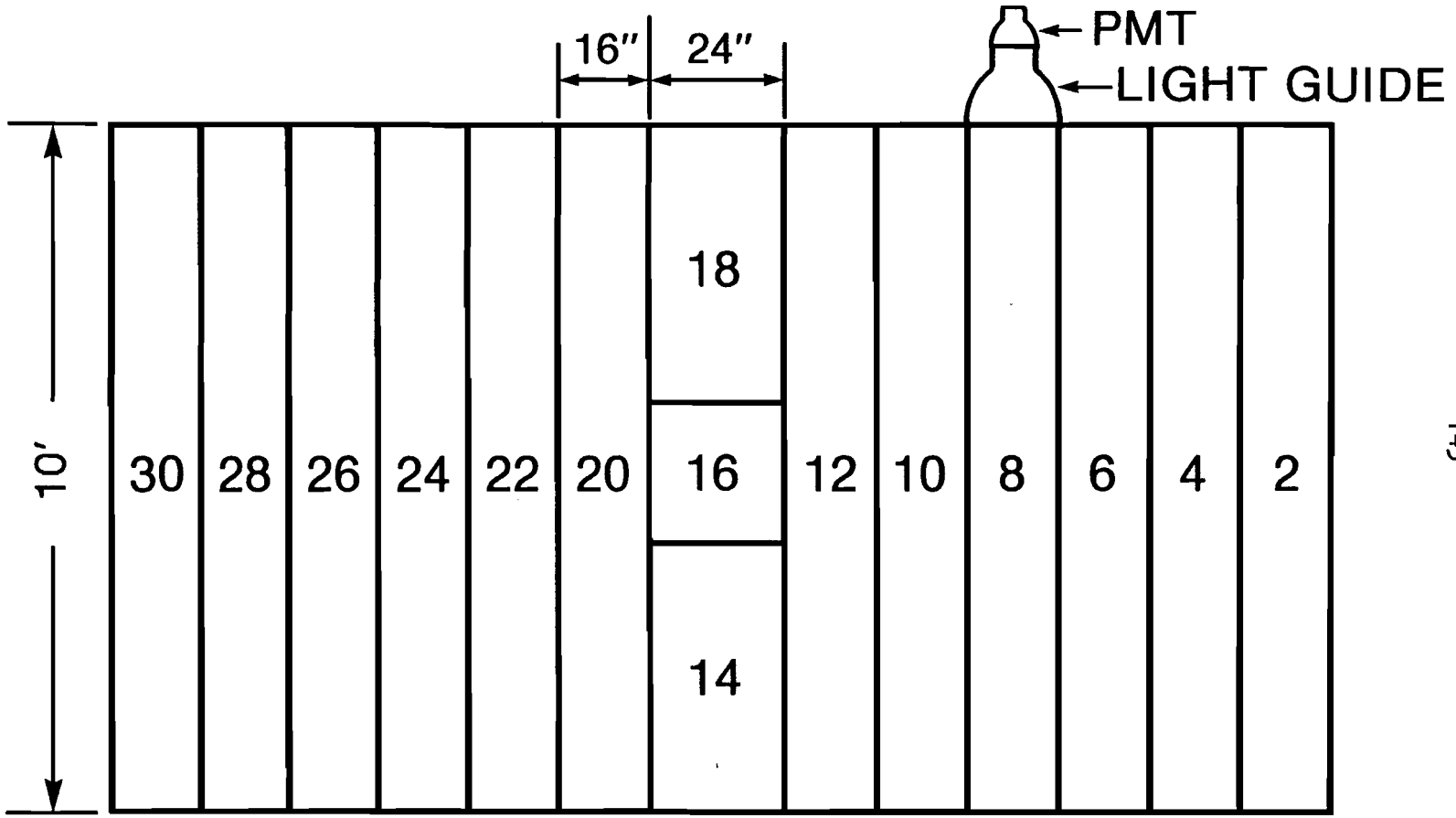

Figure 34

MUON WALL

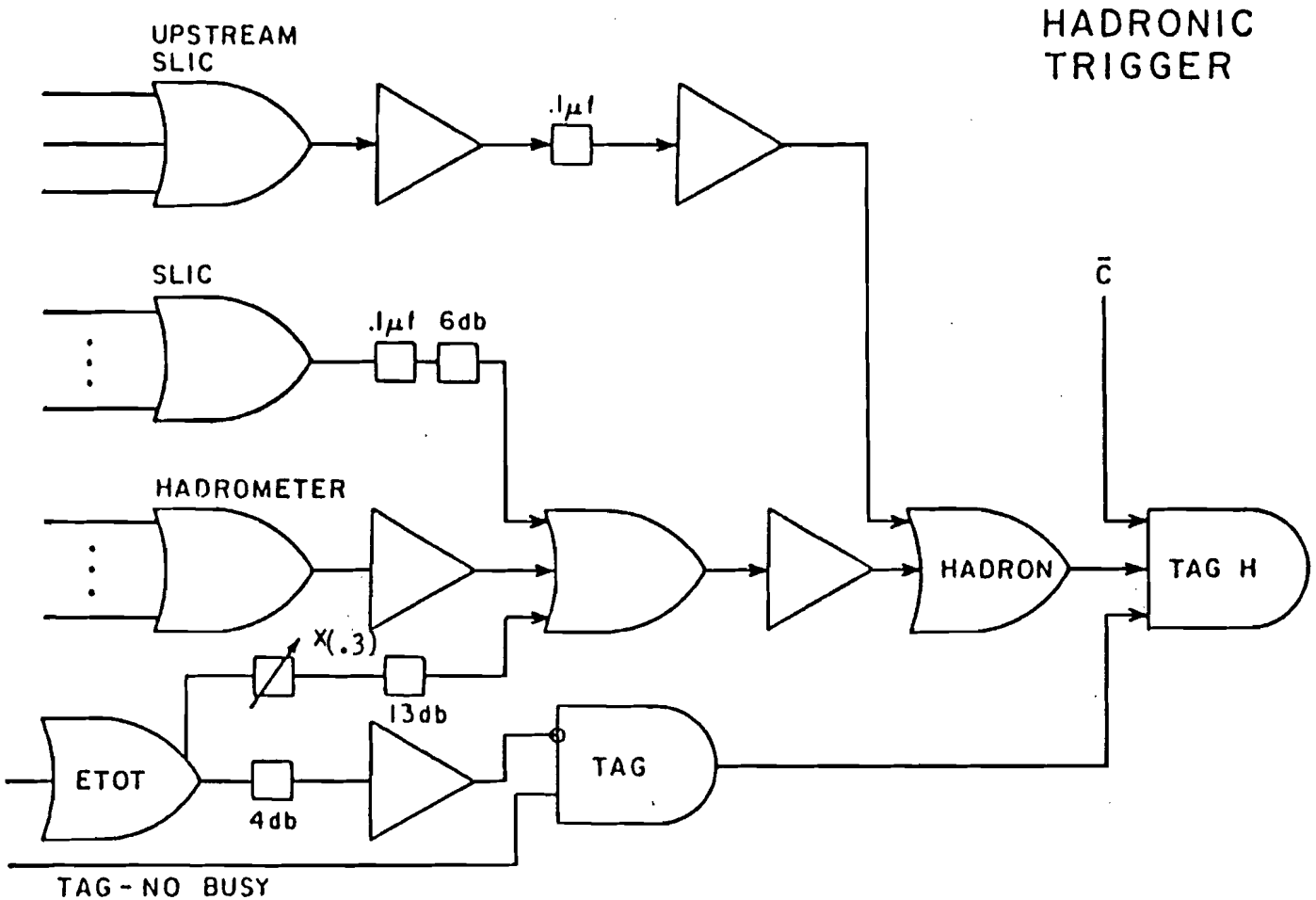
HADRONIC
TRIGGER
UPSTREAM
SLIC
.1μf
SLIC
.1μf
6db
HADROMETER
X(.3)
13db
ETOT
4db
TAG
TAG - NO BUSY
HADRON
C̄
TAG H

Figure 35

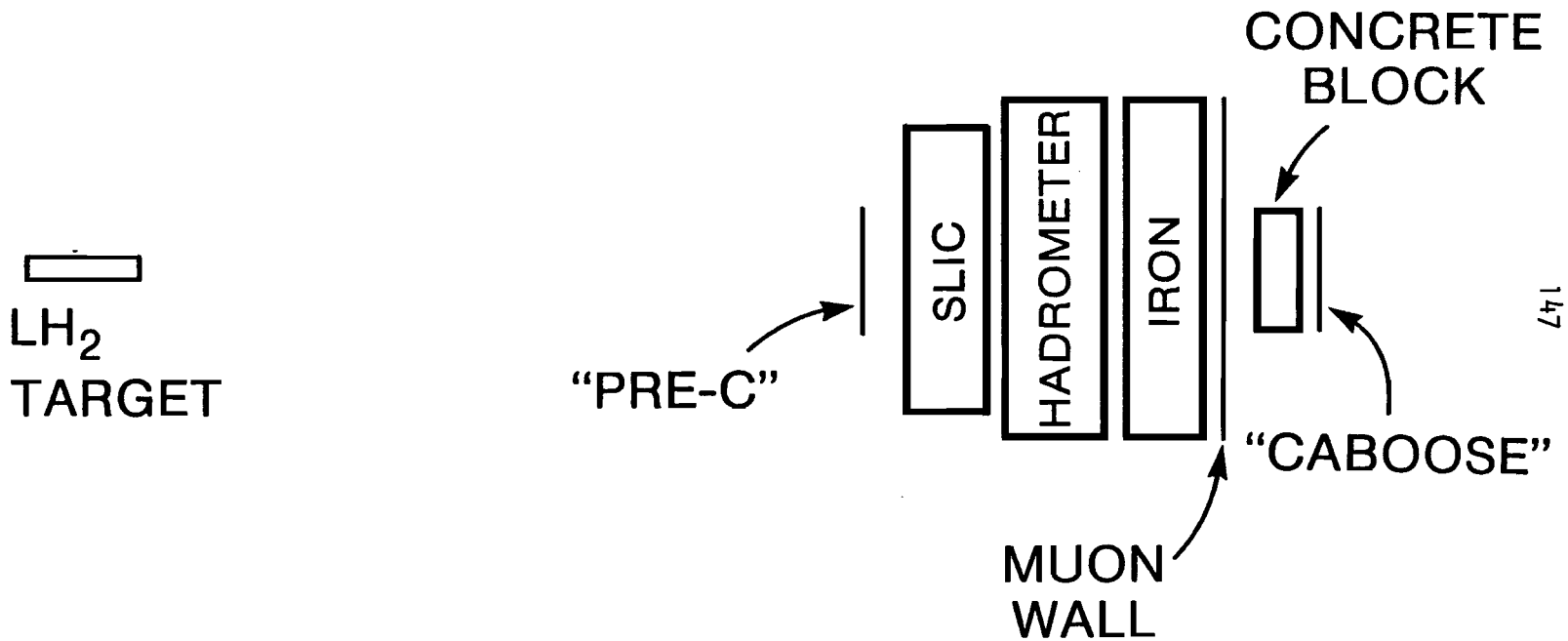

DIMUON TRIGGER COUNTER LAYOUT

Figure 36

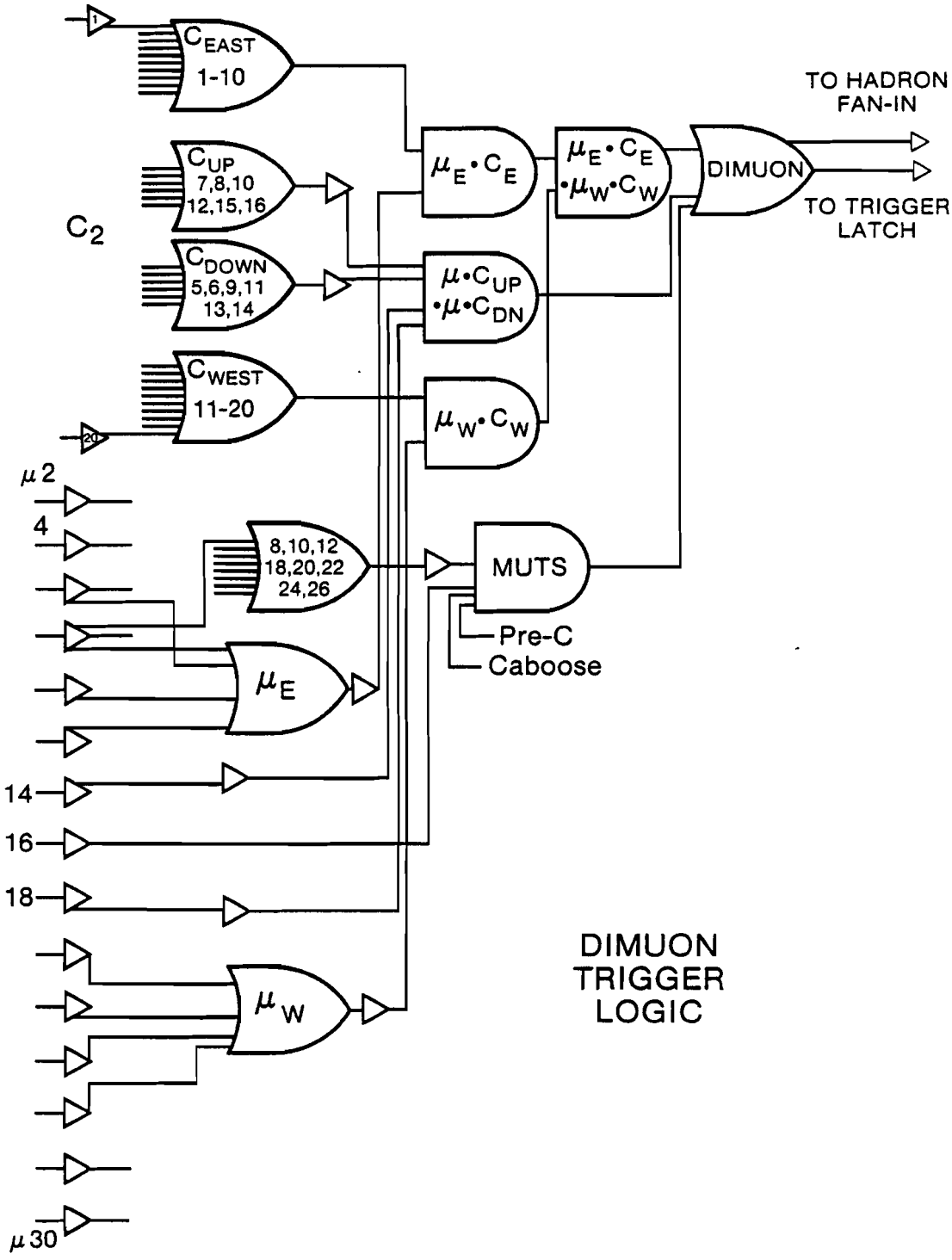
C EAST
1-10
C UP
7,8,10
12,15,16
C2
C DOWN
5,6,9,11
13,14
C WEST
11-20
μ2
4
14
16
18
μ30
8,10,12
18,20,22
24,26
μE
μW
μE • CE
μ • CUP
• μ • CDN
μW • CW
μE • CE
• μW • CW
DIMUON
MUTS
Pre-C
Caboose
TO HADRON
FAN-IN
TO TRIGGER
LATCH
DIMUON
TRIGGER
LOGIC

Figure 37

ON-LINE COMPUTER CONFIGURATION

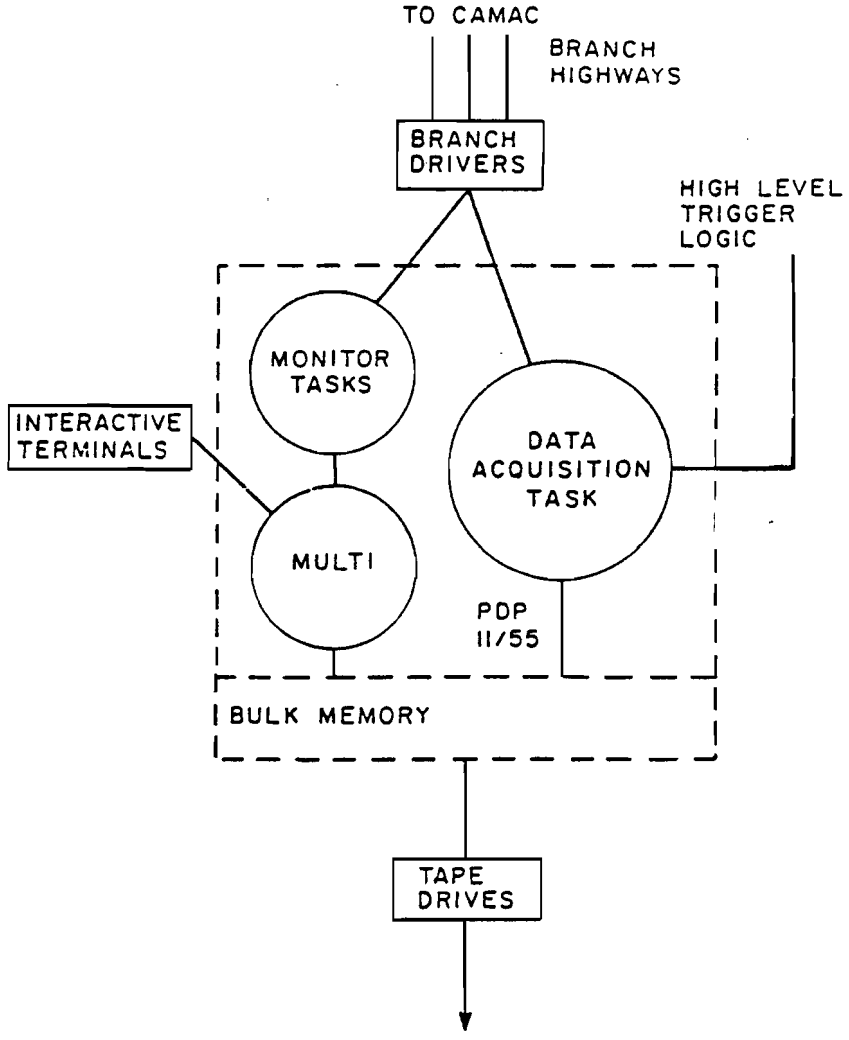

Figure 38

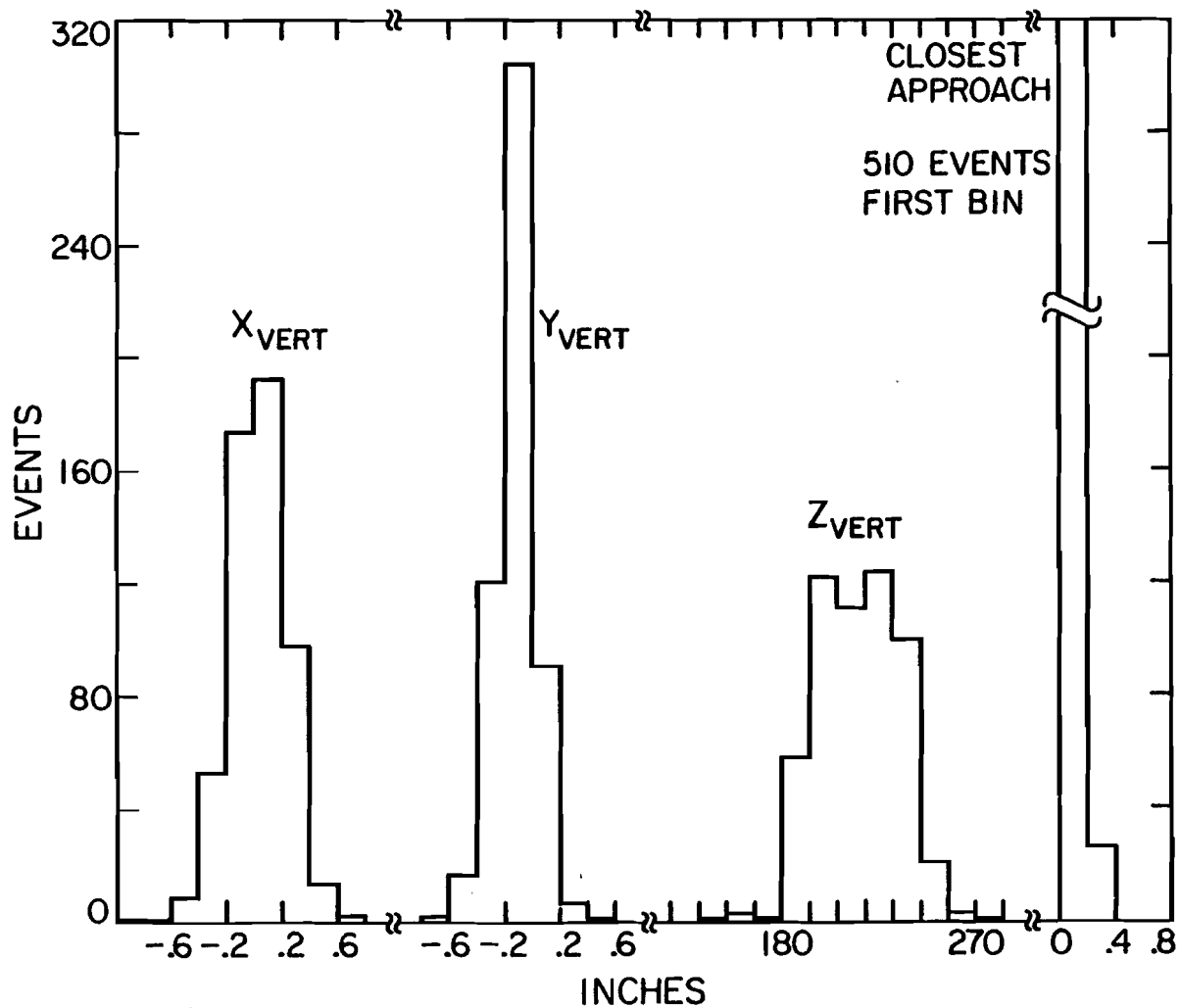
320
240
160
80
0
EVENTS
X_{VERT}
Y_{VERT}
Z_{VERT}
CLOSEST
APPROACH
510 EVENTS
FIRST BIN
-.6 -.2 .2 .6
-.6 -.2 .2 .6
180
270
0 .4 .8
INCHES

Figure 39

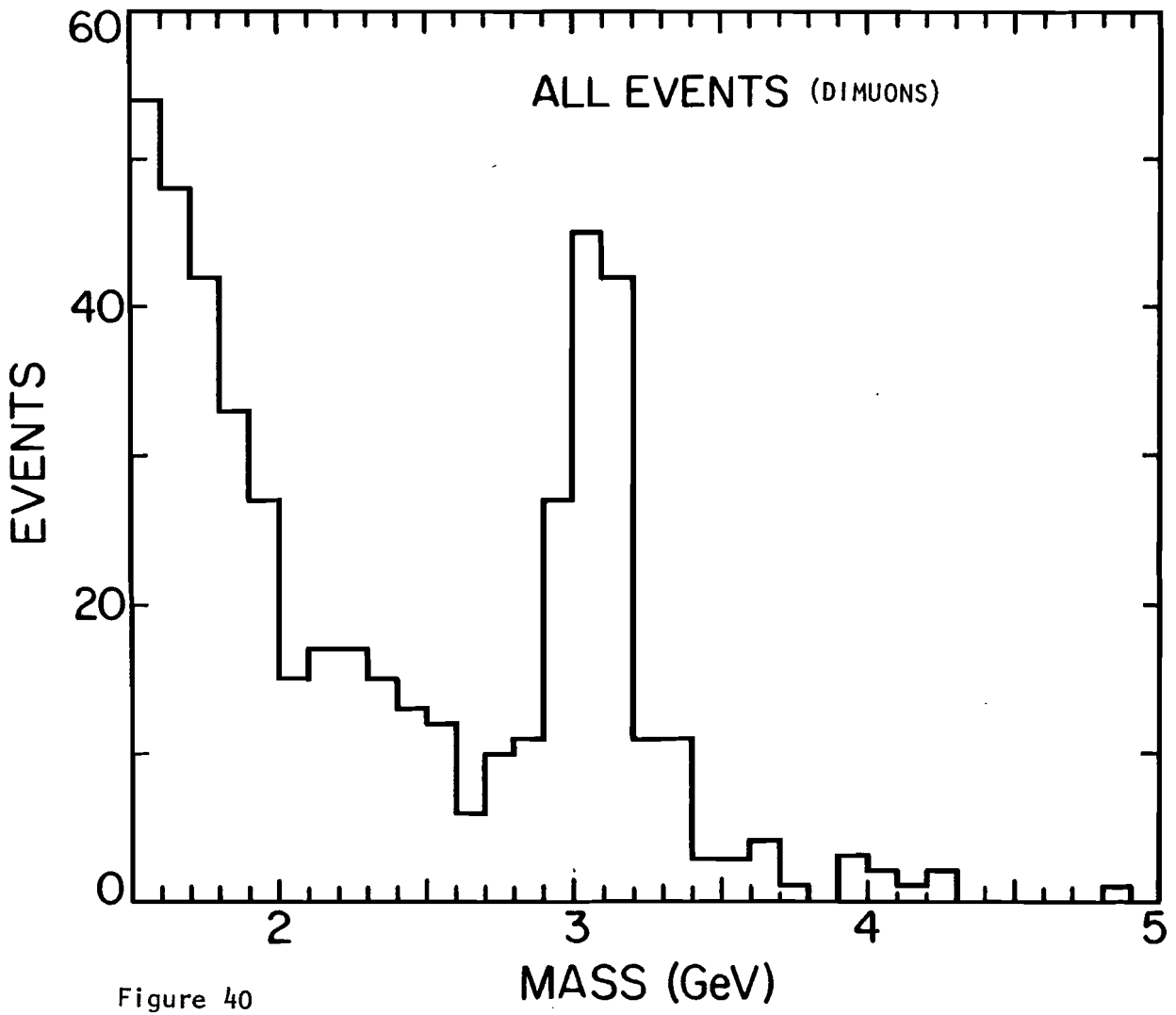

Figure 40

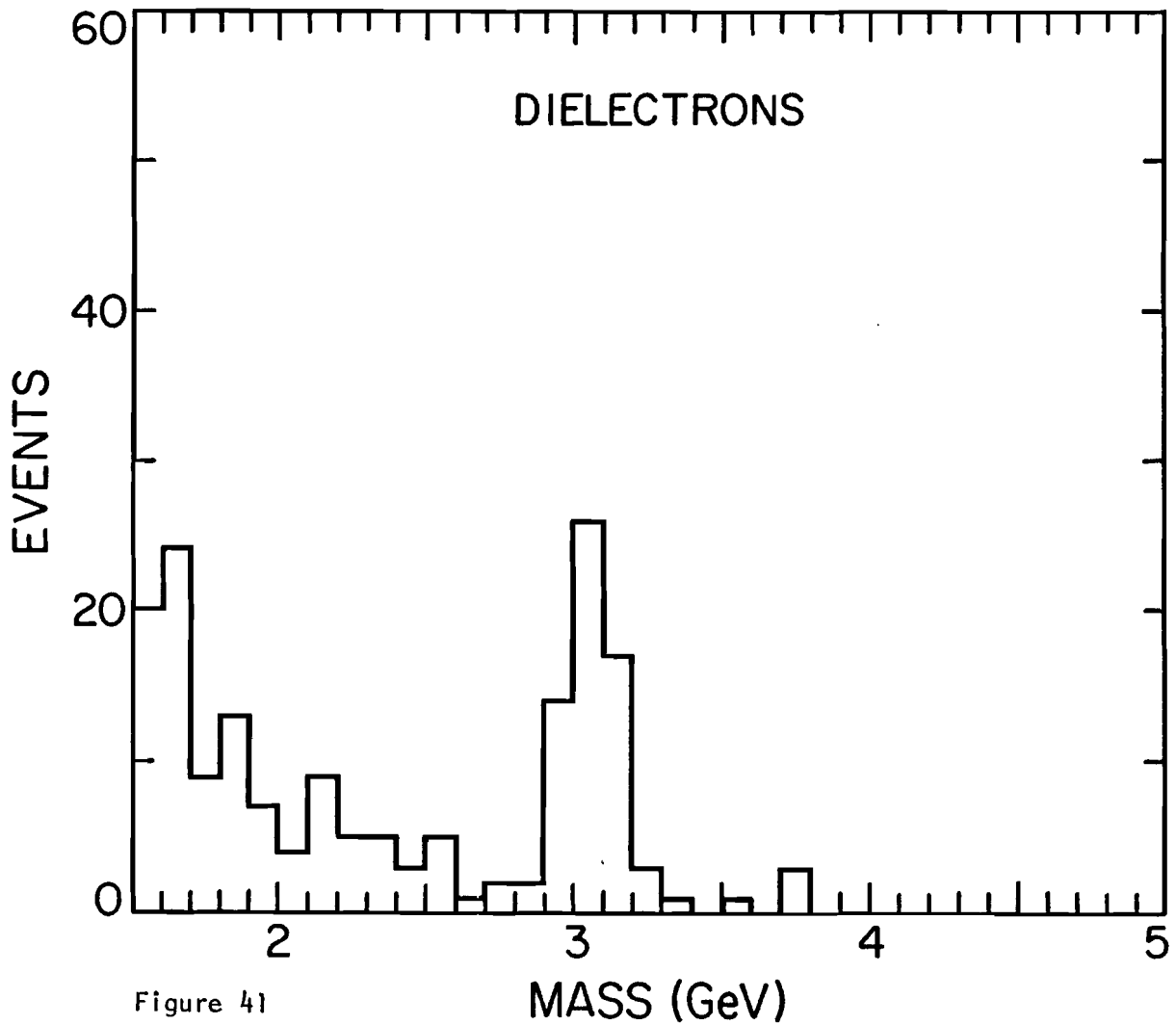

Figure 41

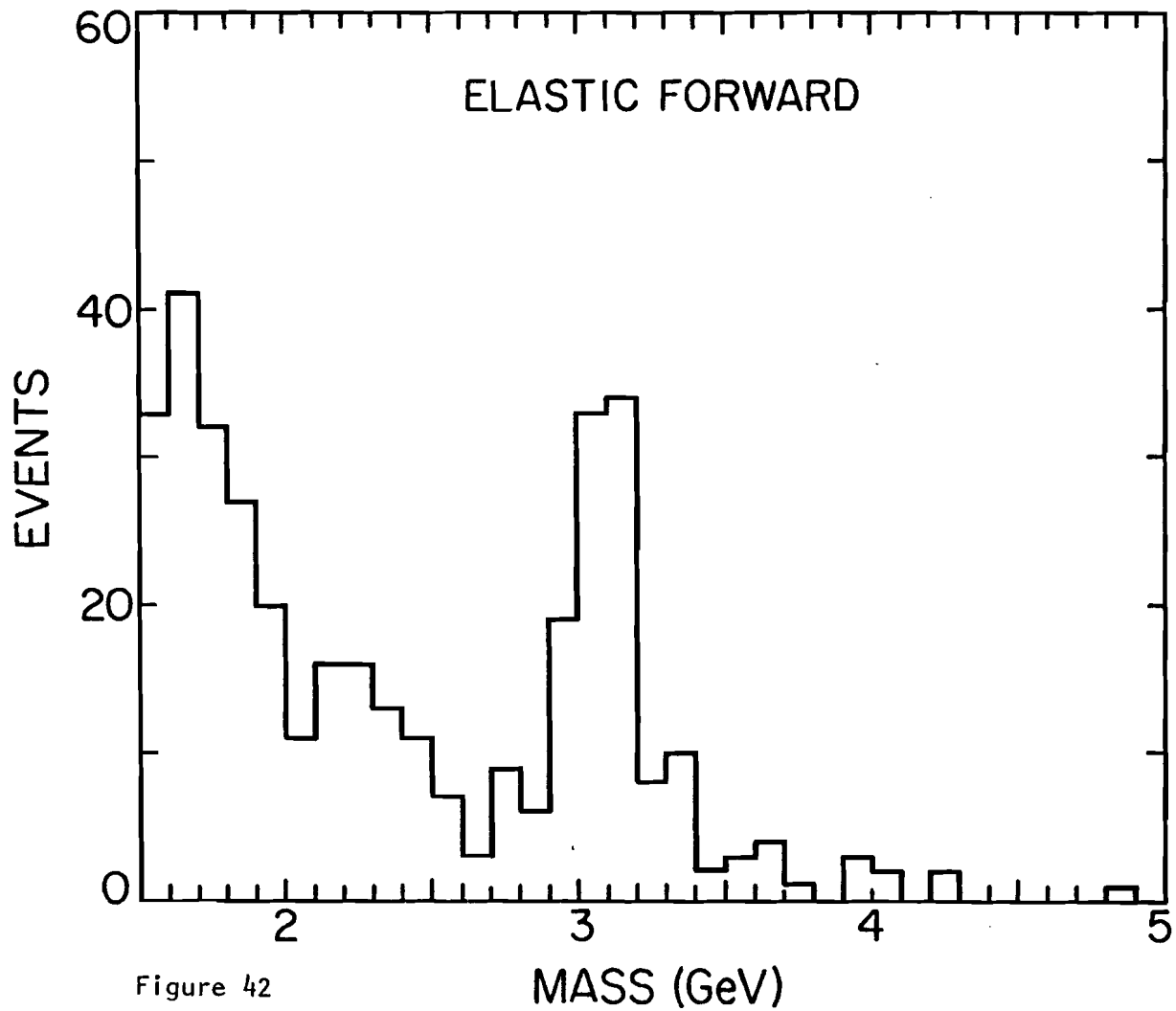

Figure 42

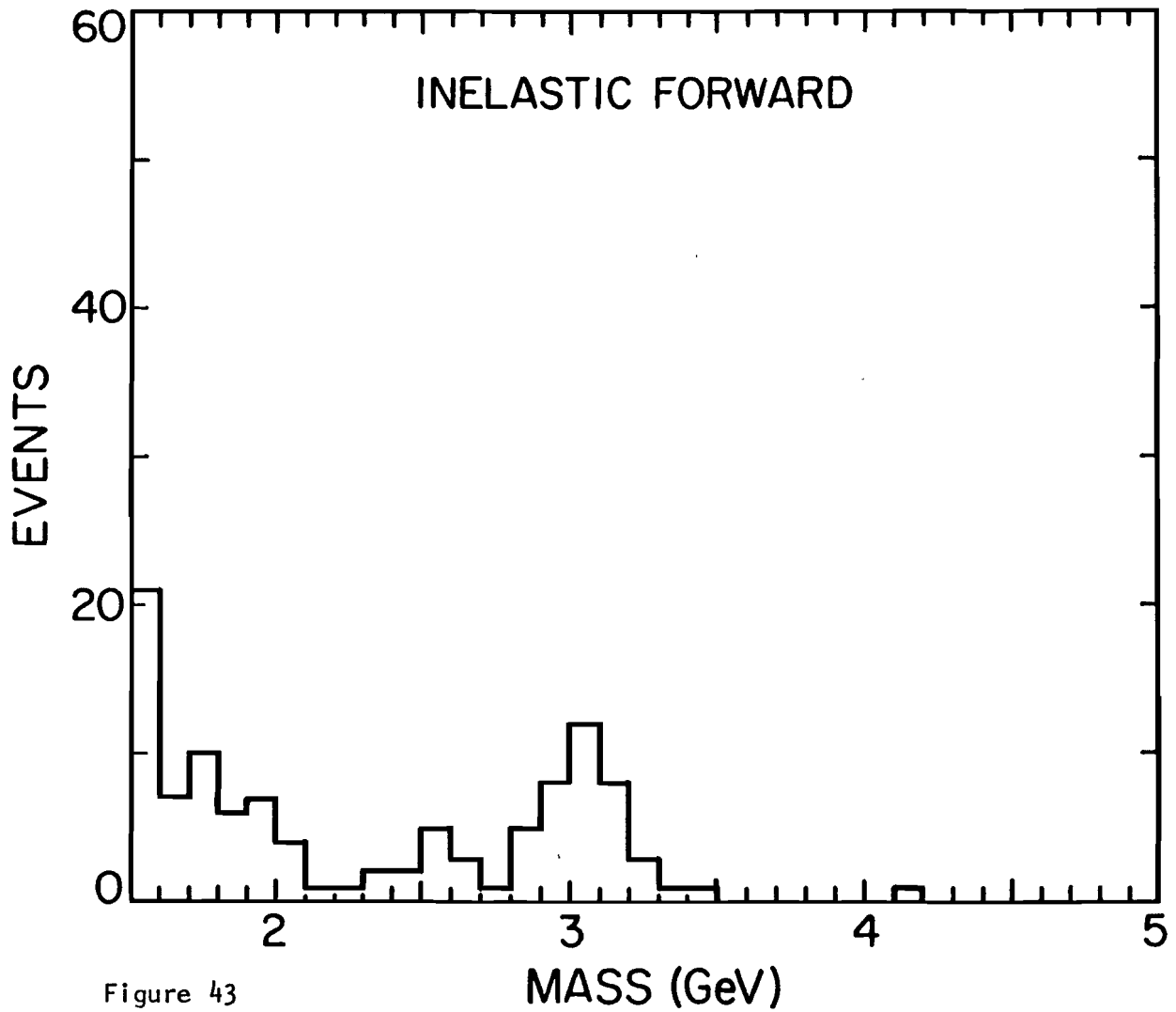

Figure 43

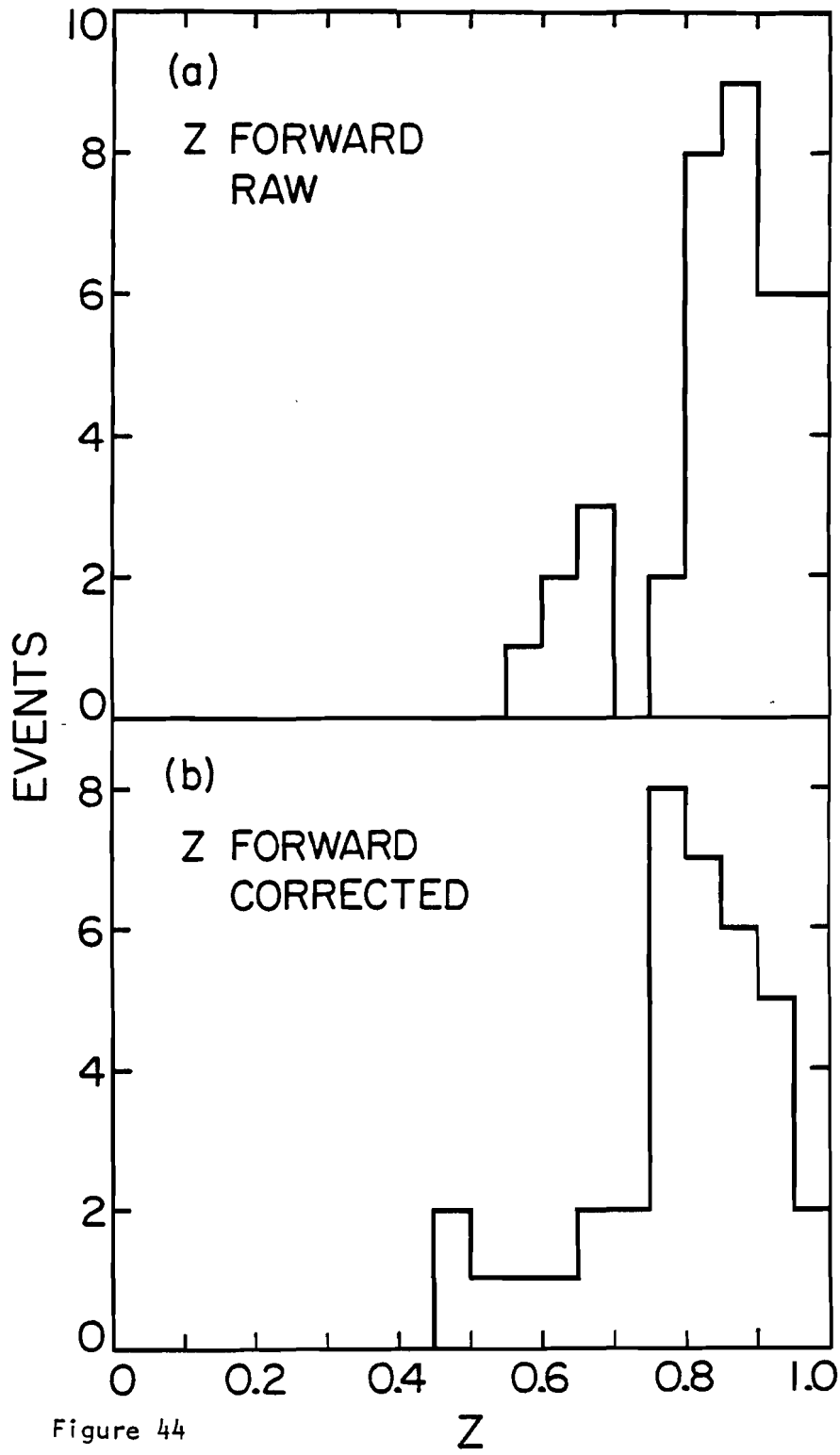
(a)
Z FORWARD
RAW
(b)
Z FORWARD
CORRECTED
EVENTS
Z
0
2
4
6
8
10
0.2
0.4
0.6
0.8
1.0

Figure 44

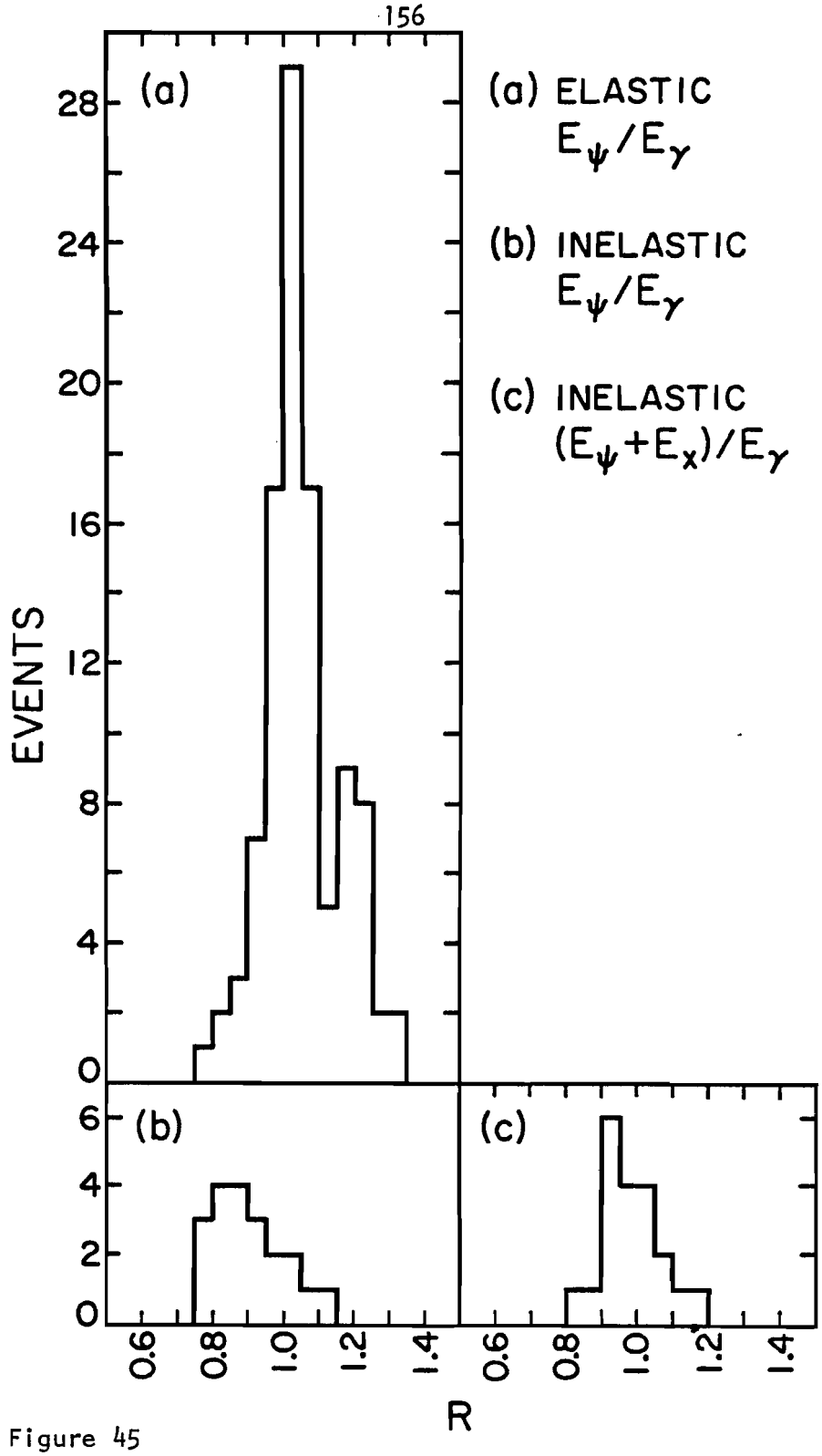
(a)
(b)
(c)
(a) ELASTIC
E_ψ/E_γ
(b) INELASTIC
E_ψ/E_γ
(c) INELASTIC
$(E_\psi+E_x)/E_\gamma$
EVENTS
R
0
4
8
12
16
20
24
28
2
6
0.6
0.8
1.0
1.2
1.4

Figure 45

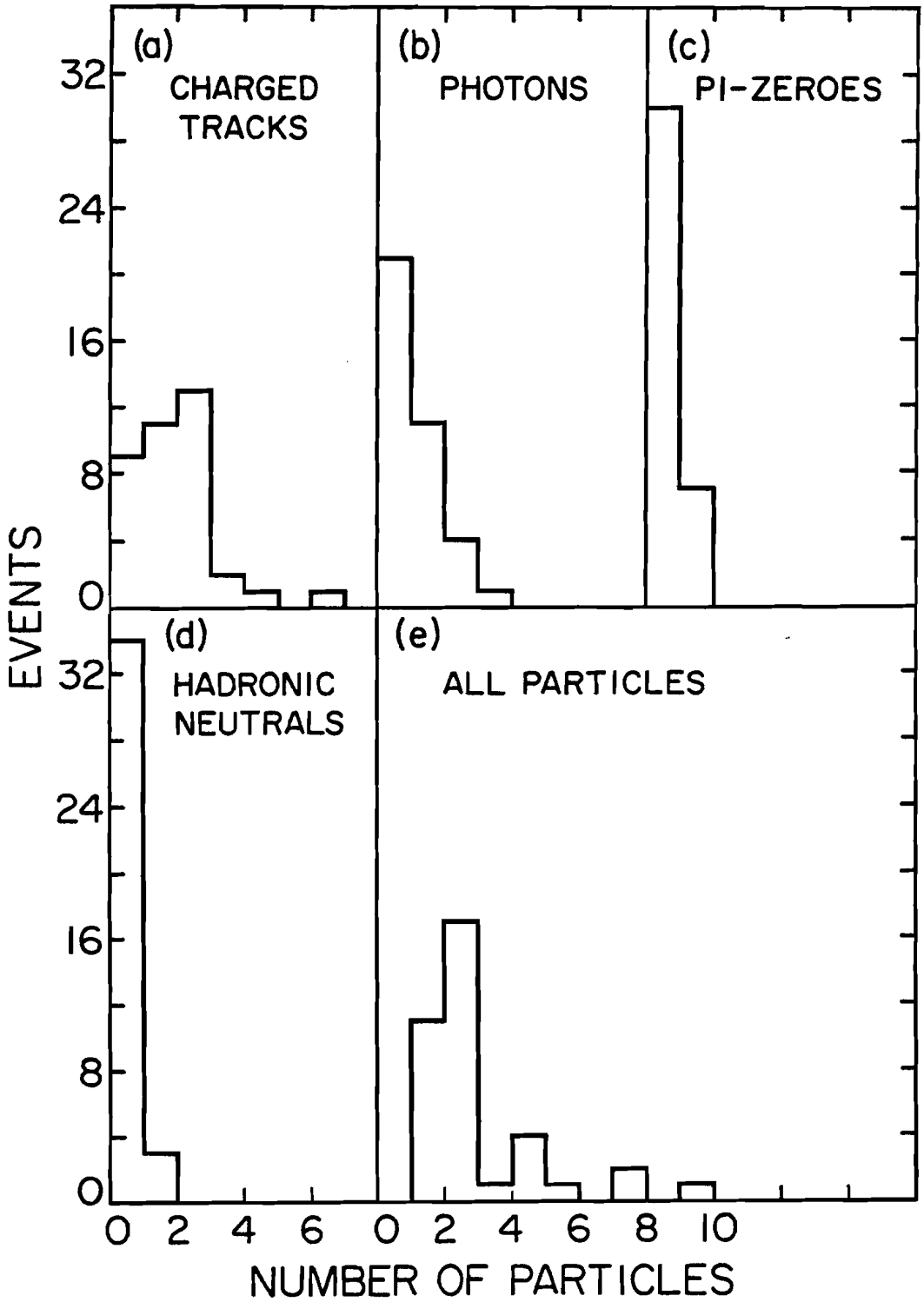
(a)
CHARGED
TRACKS
(b)
PHOTONS
(c)
PI-ZEROES
(d)
HADRONIC
NEUTRALS
(e)
ALL PARTICLES
EVENTS
0
8
16
24
32
0 2 4 6
0 2 4 6 8 10
NUMBER OF PARTICLES

Figure 46

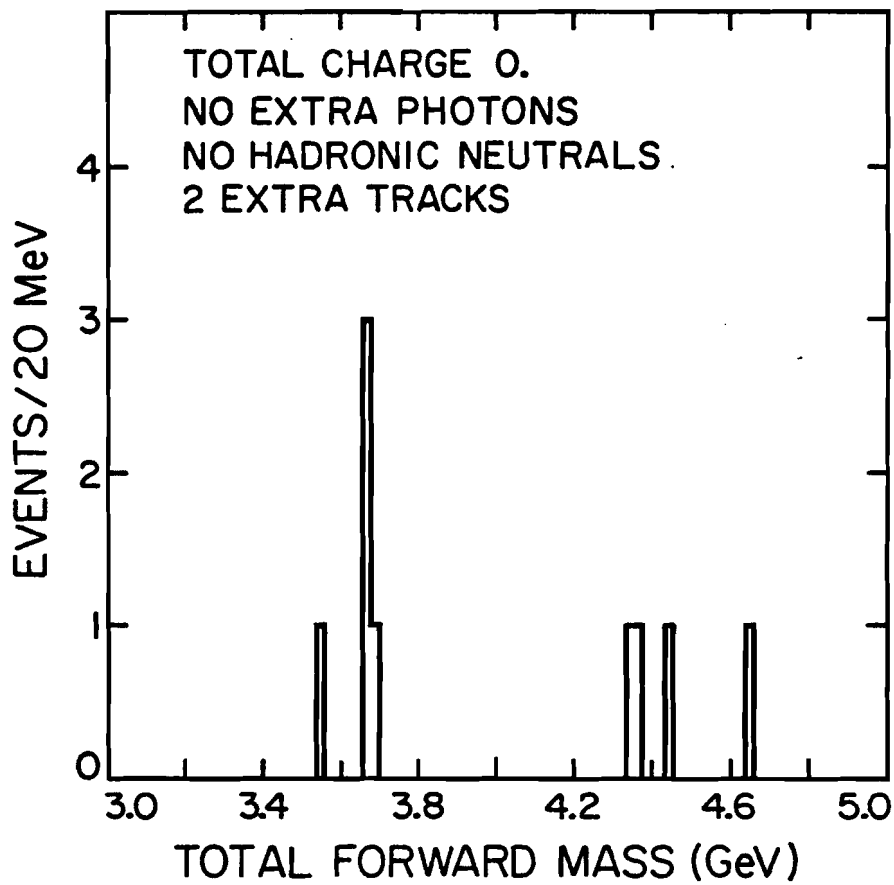
TOTAL CHARGE 0.
NO EXTRA PHOTONS
NO HADRONIC NEUTRALS
2 EXTRA TRACKS
EVENTS/20 MeV
0
1
2
3
4
3.0
3.4
3.8
4.2
4.6
5.0
TOTAL FORWARD MASS (GeV)

Figure 47

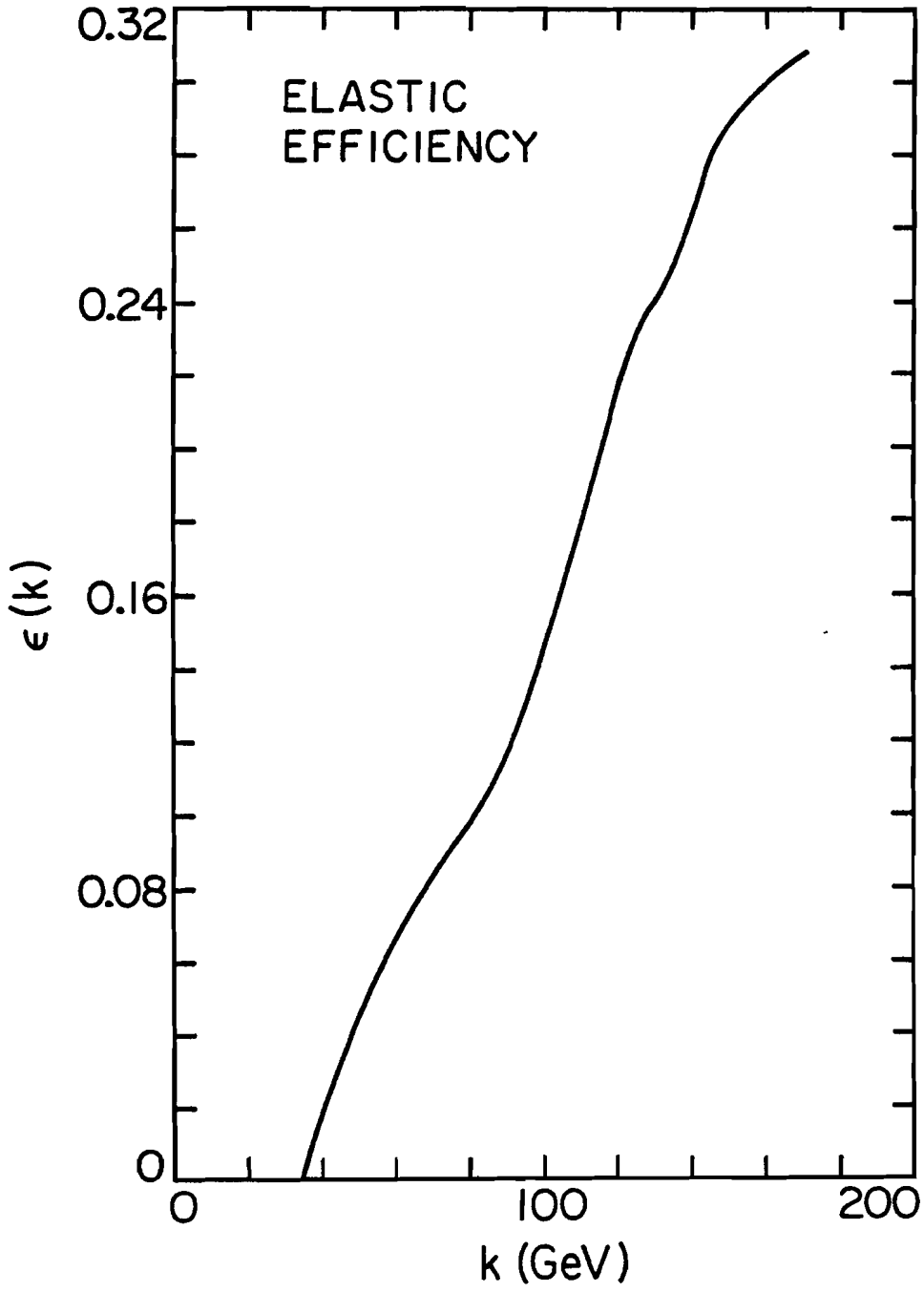

Figure 48

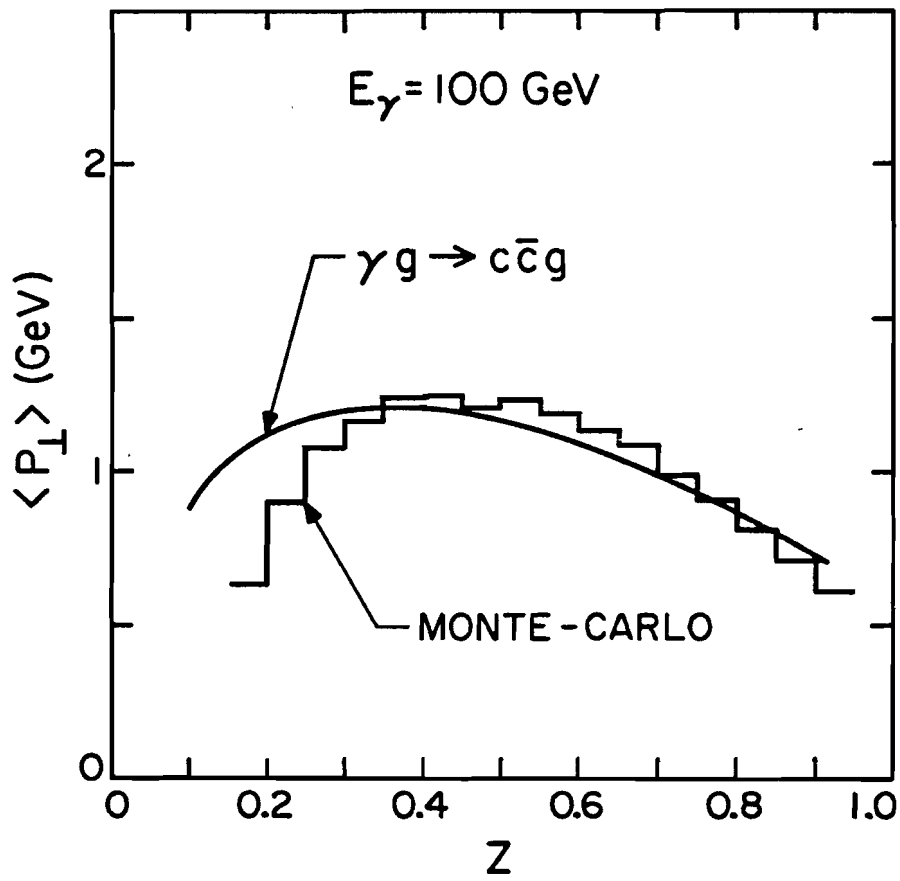
E_γ = 100 GeV
$\gamma g \rightarrow c\bar{c}g$
MONTE-CARLO
$\langle P_\perp \rangle$ (GeV)
Z
0
1
2
0
0.2
0.4
0.6
0.8
1.0

Figure 49

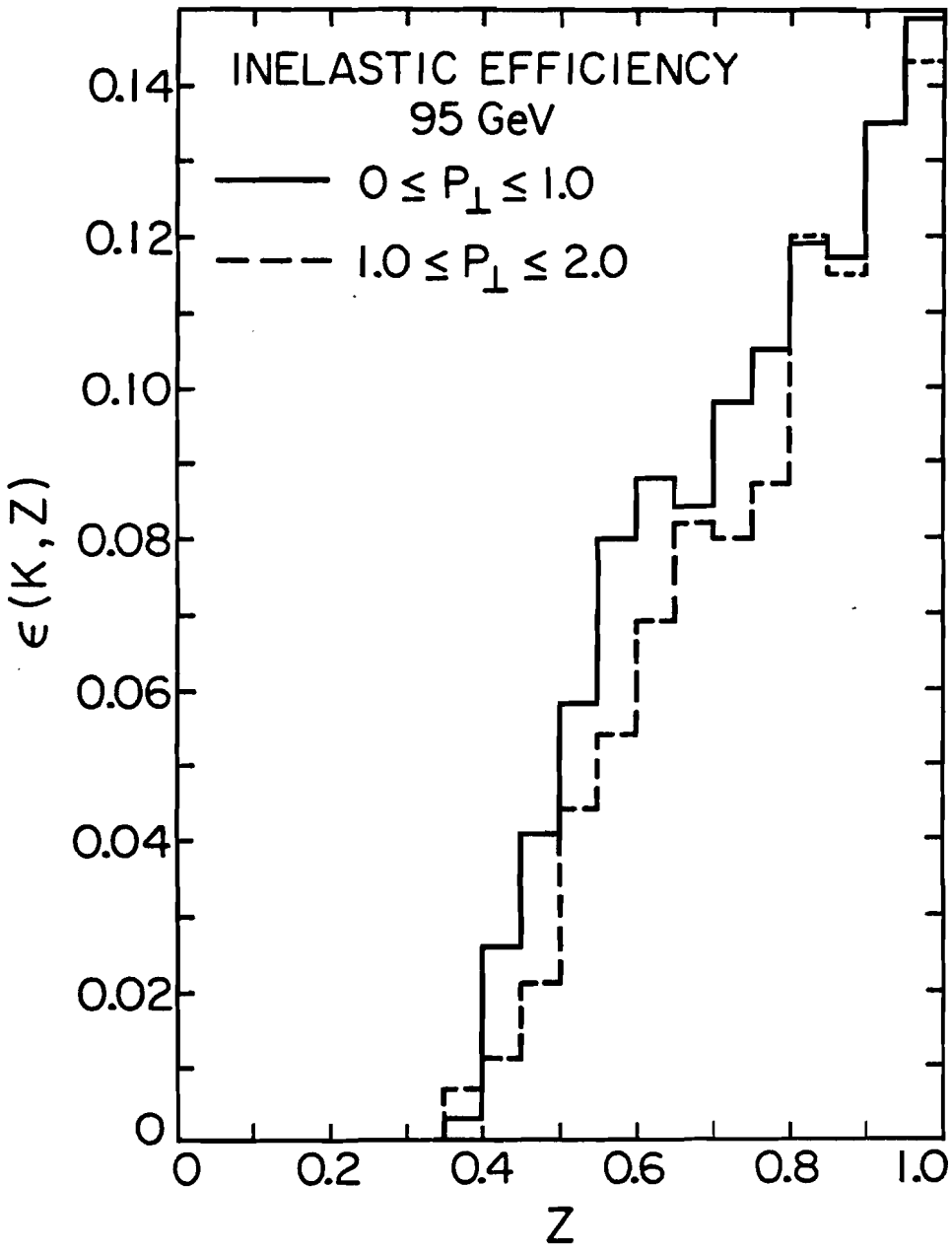
INELASTIC EFFICIENCY
95 GeV
0 ≤ P⊥ ≤ 1.0
1.0 ≤ P⊥ ≤ 2.0
ε(K, Z)
0.14
0.12
0.10
0.08
0.06
0.04
0.02
0
0
0.2
0.4
0.6
0.8
1.0
Z

Figure 50

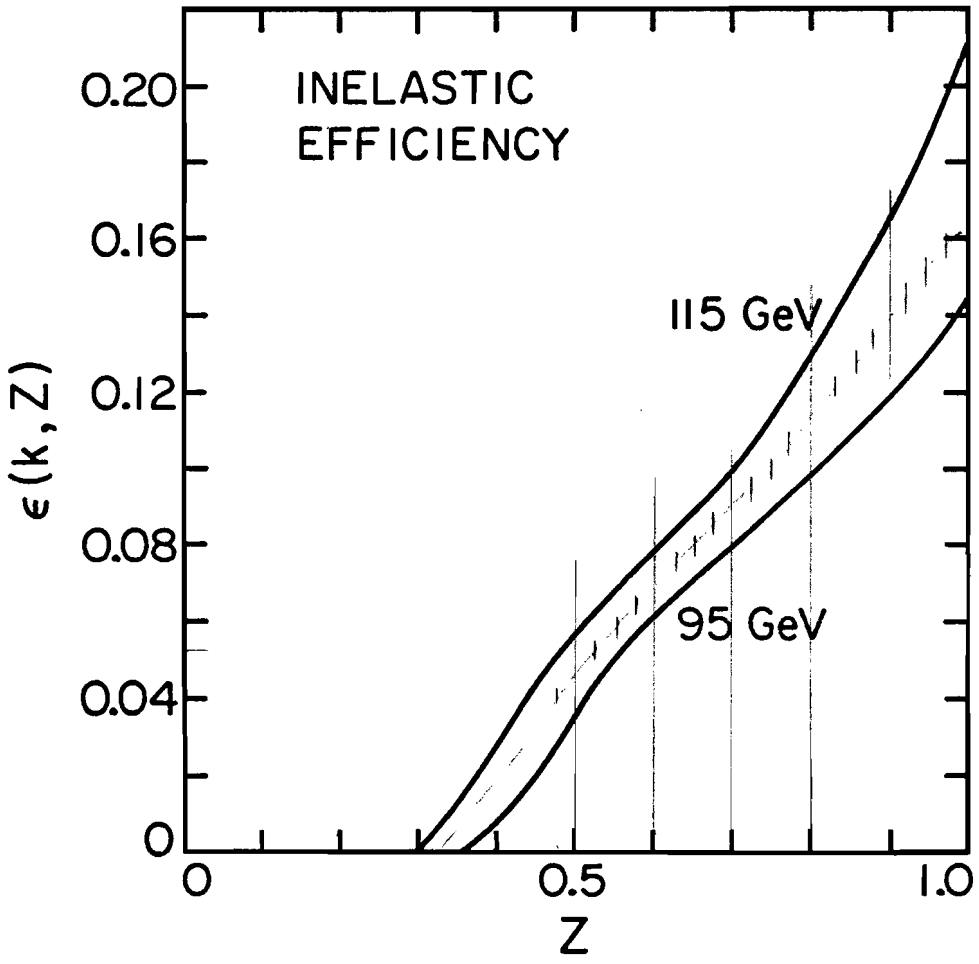
INELASTIC
EFFICIENCY
115 GeV
95 GeV
0.20
0.16
0.12
0.08
0.04
0
ε(k, Z)
0
0.5
1.0
Z

Figure 51

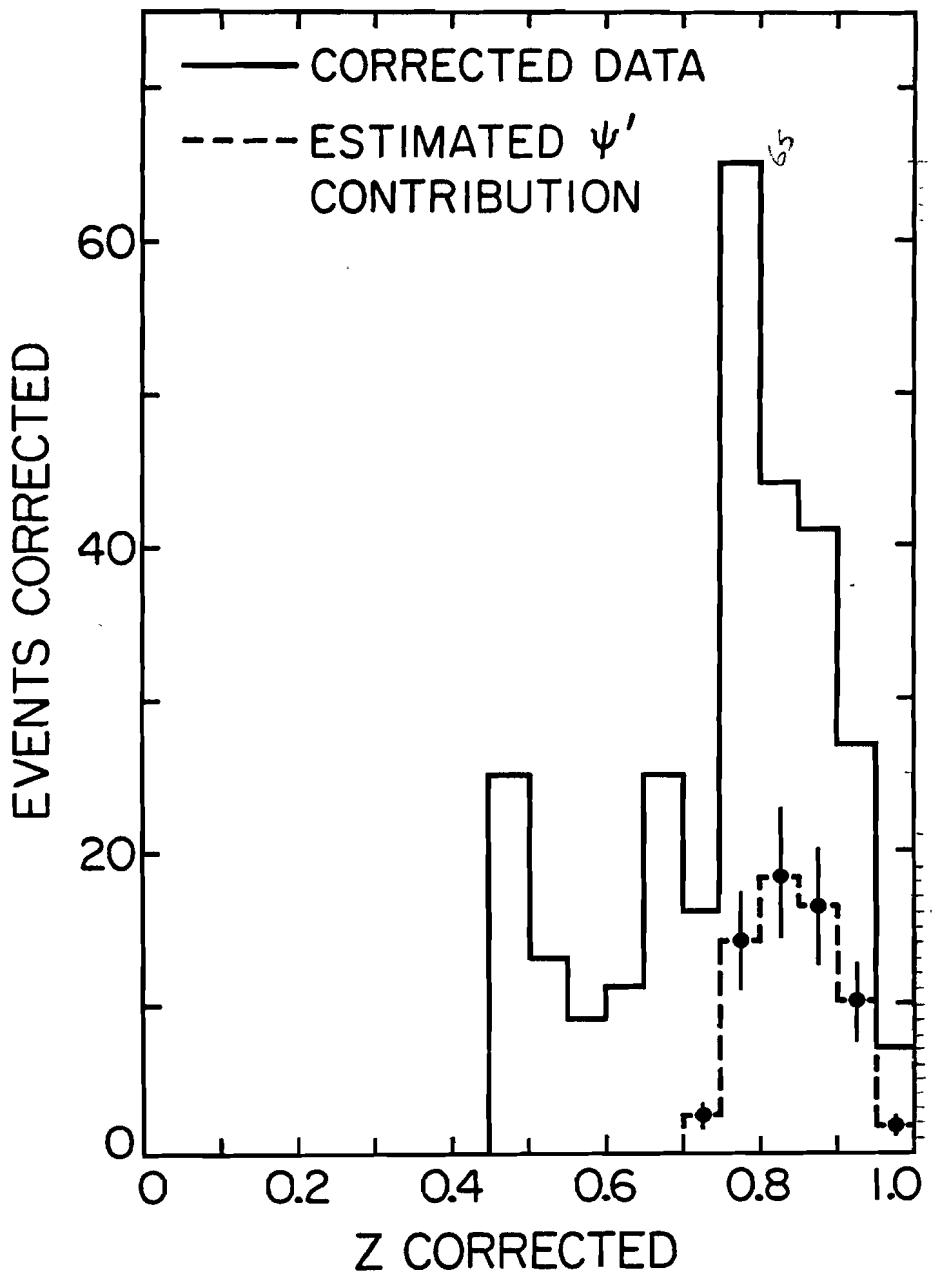
CORRECTED DATA
ESTIMATED ψ′
CONTRIBUTION
EVENTS CORRECTED
0
20
40
60
0
0.2
0.4
0.6
0.8
1.0
Z CORRECTED

Figure 52

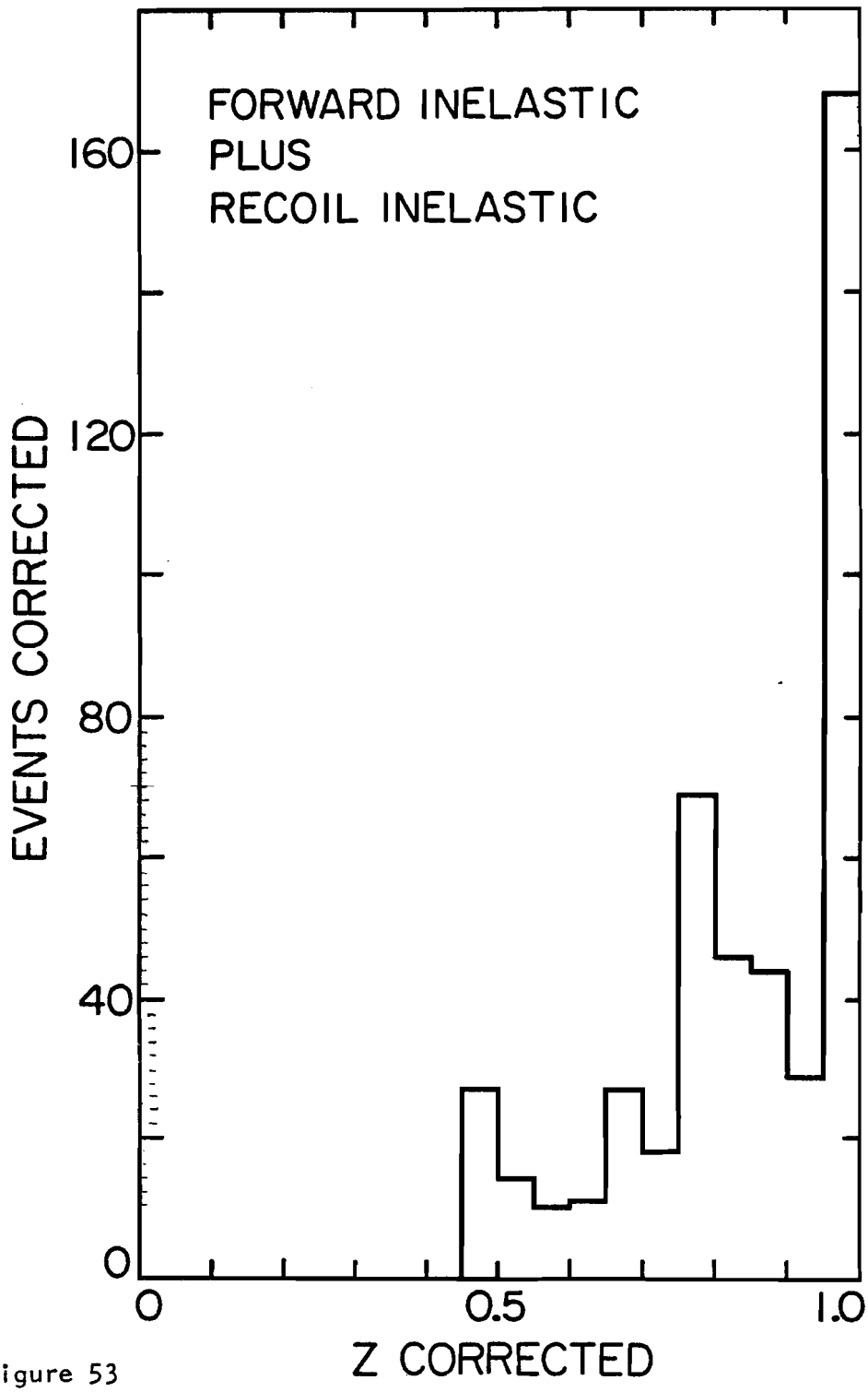
FORWARD INELASTIC
PLUS
RECOIL INELASTIC
EVENTS CORRECTED
160
120
80
40
0
0
0.5
1.0
Z CORRECTED

Figure 53

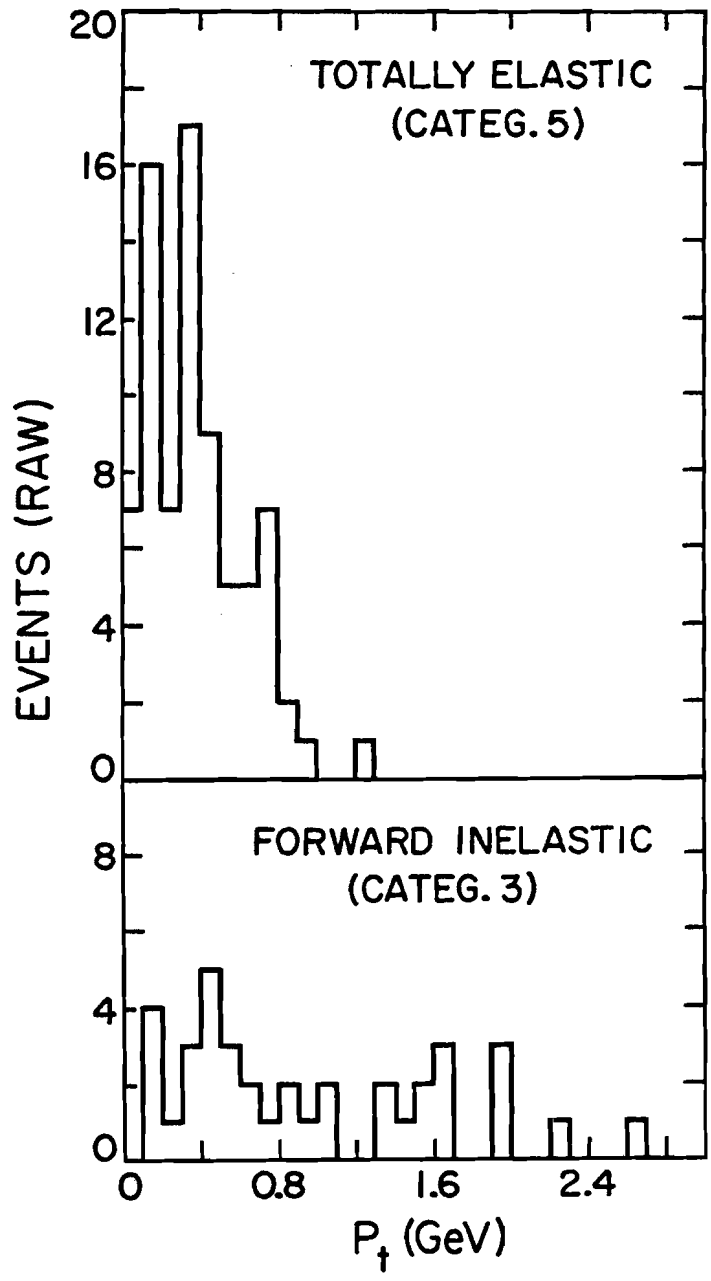
TOTALLY ELASTIC
(CATEG. 5)
FORWARD INELASTIC
(CATEG. 3)
EVENTS (RAW)
20
16
12
8
4
0
8
4
0
0
0.8
1.6
2.4
P_t (GeV)

Figure 54

APPENDIX B - TABLES

Table I

DRIFT CHAMBER RESOLUTIONS AND EFFICIENCIES

PLANE		RESOLUTION (microns)	EFFICIENCY %
D1A	U	380	92
	X	300	99
	V	425	98
	X'	340	99
D1B	U	360	96
	X	250	99
	V	380	96
	X'	230	99
D2A	U	310	98
	X	350	97
	V	300	96
D2B	U	310	99
	X	350	97
	V	290	99
D2C	U	320	99
	X	340	95
	V	310	97
D3A	U	300	99
	X	350	99
	V	310	99
D3B	U	280	99
	X	320	99
	V	270	99
D3C	U	290	99
	X	330	99
	V	290	99
D4A	U	350	99
	X	350	99
	V	350	99

Table II

CHARACTERISTICS OF THE CERENKOV COUNTERS

QUANTITY	C1	C2
GAS MIXTURE	100% N_2	80% He 20% N_2
LENGTH	3.7 meters	6.6 meters
INDEX OF REFRACTION	1.00027	1.00012
CERENKOV ANGLE	25 mrad	14 mrad
THRESHOLD FOR PIONS	6.0 GeV/c	9.1 GeV/c
THRESHOLD FOR KAONS	20 GeV/c	36 GeV/c
THESHOLD FOR PROTONS	38 GeV/c	69 GeV/c

Table III

CERENKOV COUNTERS CELL DIMENSIONS

CELL	C1(WIDTH,HEIGHT) inches	C2(WIDTH,HEIGHT) inches
1-1	4.0 , 8.0	10.0 , 18.0
1-2	8.0 , 8.0	20.0 , 18.0
1-3	38.0 , 8.0	65.0 , 18.0
1-4	12.0 , 16.0	30.0 , 32.0
1-5	38.0 , 16.0	65.0 , 32.0

CATEGORY	RAW EVENTS	BKGD. EVENTS	CORR. EVENTS
All	147 ± 12.1	23 ± 8	785 ± 92
Forward Elastic	110 ± 10.4	18 ± 7	526 ± 72
Forward Inelastic	37 ± 6.1	4 ± 2	269 ± 54
Forward Elastic Recoil Inelastic	33 ± 5.7	5 ± 2	161 ± 47
Forward Elastic Recoil Elastic	77 ± 8.8	13 ± 5	365 ± 72
Inelastic	70 ± 8.4	9 ± 4	429 ± 75
Inelastic $Z < .9$	30 ± 5.5	3 ± 2	240 ± 51

Table IV

CATEGORY	a) FRACTION	b) ψ'-SUBTRACTED FRACTION
All	1	1
Forward Elastic	.67 ± .08	.73 ± .09
Forward Inelastic	.34 ± .07	.28 ± .06
Forward Elastic Recoil Inelastic	.21 ± .06	.22 ± .06
Forward Elastic Recoil Elastic	.46 ± .08	.51 ± .09
Inelastic	.55 ± .09	.50 ± .08
Inelastic $Z < .9$	.31 ± .06	.26 ± .05

Table V

CATEGORY	a) CROSS SECTION(NB)	b) ψ'-SUBTRACTED CROSS SECTION(NB)
All	21.5 ± 2.4	19.6 ± 2.4
Forward Elastic	14.2 ± 1.9	14.2 ± 1.9
Forward Inelastic	7.3 ± 1.4	5.4 ± 1.5
Forward Elastic Recoil Inelastic	4.4 ± 1.1	4.4 ± 1.1
Forward Elastic Recoil Elastic	9.8 ± 1.8	9.8 ± 1.8
Inelastic	11.7 ± 2.0	9.8 ± 2.1
Inelastic $Z < .9$	6.6 ± 1.4	5.1 ± 1.4

Table VI

N.B.: There is an additional ~25% uncertainty in overall normalization of cross sections.

E516 Forward Elastic	BFP[17] Elastic	EMC[16] $Z \geq .95$	Wide Band[18] Forward Elastic
14.2 ± 1.9(±3.6) @ 103 GeV	20.7 ± 1.2(±4.1) @ 108 GeV	12.8 ± 2.0 @ 80 - 100 GeV 11.5 ± 2.0 @ 100 - 120 GeV	~21(±3) @ ~100 GeV

Table VII(a)
Elastic

E516 $Z < .9$	BFP $Z < .9$	EMC $Z < .95$	Wide Band
5.1 ± 1.4(±1.3) @ 103 GeV (ψ' subtracted)	16.8 ± 1.3(±2.7) @ 111 GeV	16.8 ± 2.9 @ 80 - 100 GeV	----
6.6 ± 1.4(±1.7) @ 103 GeV (ψ' not subtracted)		28.0 ± 4.0 @ 100 - 120 GeV	

Table VII(b)
Inelastic

E516 $\frac{\sigma_Z < .9}{\sigma_{FWD\ Elastic}}$	BFP $\frac{\sigma_Z < .9}{\sigma_{Elastic}}$	EMC $\frac{\sigma_Z < .95}{\sigma_Z \geq .95}$	Wide Band
.36 ± .07 @ 103 GeV ψ' subtracted	.81 ± .08 @ ~108 GeV	1.3 ± .3 @ 80 - 100 GeV	----
.46 ± .09 @ 103 GeV ψ' not subtracted		2.4 ± .5 @ 100 - 120 GeV	

Table VII(c)
Elastic/Inelastic

REFERENCES

1) See, for example, F. Gilman, Phys. Rep. 4C (1972) 95.

2) T. Appelquist, R. Barnett, K. Lane, Charm and Beyond, SLAC PUB-2100 (March 1978).

3) D. Duke and J. Owens, Phys. Lett. 96B (1980) 184.

4) J. Leveille and T. Weiler, Phys. Lett. 86B (1979) 377.

5) E. Berger and D. Jones, Phys. Rev. D23 (1981) 1521.

6) F. Halzen, Production of Heavy Quarks, Proceedings of the XXI International Conference on High Energy Physics, Paris, 1982, p. 381.

7) L. Jones and H. Wyld, Phys. Rev. D17 (1978) 2332.

8) J. Babcock, D. Sivers, S. Wolfram, Phys. Rev. D18 (1978) 162.

9) T. Weiler, Phys. Rev. Lett. 44 (1980) 304.

10) T. Tajima, T. Watanabe, Phys. Rev. D23 (1981) 1517.

11) J. Leveille, T. Weiler, Nuc. Phys. B147 (1979) 147.

12) H. Fritzsch, Phys. Lett. 67B (1977) 217.

13) H. Fritzsch, K. Streng, Phys. Lett. 72B (1978) 385.

14) R. Philips, Phenomenology of New Particle Production, Proceedings of the XX International Conference on High Energy Physics, Madison, Wisconsin, 1980, p. 1471.

15) M. Binkley et al., Phys. Rev. Lett. 50 (1983) 302.

16) J.J. Aubert et al., EMC, Nuc. Phys. B213 (1983) 1.

17) T. Markiewicz, Ph.D. thesis, U.C. Berkeley, 1981.

18) M. Binkley et al., Phys. Rev. Lett. 48 (1982) 73.

19) A. Clark et al., BFP, Phys. Rev. Lett. 43 (1979) 187.

20) J.J. Aubert et al., EMC, CERN EP/80-84, 1980.

21) M. Strovink, Review of Multimuon Production by Muons, Proceedings of the 1981 International Symposium on Lepton and Photon Interactions at High Energies, Bonn, W. Germany, p. 594.

22) B. Knapp et al., Phys. Rev. Lett. 34 (1975) 1040.

23) T. Nash et al., Phys. Rev. Lett. 36 (1976) 1233.

24) U. Camerini et al., Phys. Rev. Lett. 35 (1975) 483.

25) B. Gittleman et al., Phys. Rev. Lett. 35 (1975) 1616.

26) E. Barsotti et al., IEEE Trans. Nucl. Sci. NS-26 (1979) 686.

27) J. Martin et al., Use of the ECL-CAMAC Trigger Processor System for Recoil Missing Mass Triggers at the Tagged Photon Spectrometer at Fermilab, Proceedings of the Topical Conference on the Applications of Microprocessors to High-Energy Physics, CERN, 1981.

28) T. Nash, A Review of Programmable Systems Associated with Fermilab Experiments, ibid.

29) R. Mount, Multimuon Production in 280 GeV μ Iron Interactions, Proceedings of the XX International Conference on High Energy Physics, Madison, Wisconsin, 1980, p. 205.

30) This technique was suggested by Dr. T. Jensen, Univ. of Minnesota.

31) Many of the techniques used in construction of the splitters were suggested by C. Kerns, Fermilab.

32) Ferroxcube Corp., Elk Grove Village, Ill.

33) G. Hartner et al., A Recoil Proton Detector Using Cylindrical Proportional Chambers and Scintillation Counters, accepted for publication, Nucl. Inst. Meth., 1983.

34) Y. Tsai, Rev. Mod. Phys. 46 (1974) 815.

35) C. Kerns, Fermilab.

36) J. Kenney, Project Engineers, Arcadia, Calif.

37) V. Bharadwaj et al., Nucl. Inst. Meth. 155 (1978) 411.

38) V. Bharadwaj et al., A Large Area Liquid Scintillator Multiphoton Detector, University of California, Santa Barbara, High Energy Physics, unpublished.

39) J.J. Aubert et al., EMC, Phys. Lett. 123B (1983) 275.

40) Stanford: Physics Archaeology, CERN Courier 23 (1983) 90.

41) A. Duncan, Ph.D. thesis, Univ. of Colorado, 1982.

42) See also J. Appel et al., Tagged Photon Magnetic Spectrometer: Facility Design Report, Fermilab, 1977.

43) It has been pointed out by Baier and Ruckl, Bielefeld Report BI-TP81/30 (1980), that the Berger and Jones model depends strongly on the mass of the charmed quark. A mass of 1.2 GeV gives agreement with the EMC data (16).